A Feasibility Analysis of Space-Based Laser Ranging for Orbital Object Search and Acquisition

by

William Ediger

A thesis submitted to the
Faculty of Graduate and Postdoctoral Studies
of the University of Manitoba
in partial fulfilment of the requirements of the degree of

Master of Science
in
Mechanical Engineering

Department of Mechanical Engineering
University of Manitoba
Winnipeg

Abstract

A rapid growth of space-based platforms has increased the need for maintaining accurate position and velocity catalogs on spacecraft, debris, and naturally occurring objects, collectively referred to as resident space objects (RSOs). Space situational awareness (SSA) technologies are essential for identifying and tracking RSOs to protect current and future space assets. This thesis investigates the feasibility of using space-based laser rangefinding systems for RSO detection. A prototype built from commercial off-the-shelf components is evaluated through simulation, analysis, and experimental testing. This thesis also presents models comparing the trade-offs of key performance parameters for general space-based laser rangefinder systems and introduces a Bayesian search and acquisition algorithm. Results show that detecting uncooperative RSOs with a low-power rangefinder is limited by weak return signals. This study further demonstrated that combining laser rangefinders with optical cameras improves the reliability of obtaining RSO position estimates. Finally, the results emphasize the value of incorporating cooperative features on spacecraft, such as retroreflectors, to improve visibility and contribute to safer operations in near-Earth space.

Acknowledgements

Thank you to my advisor, Dr. Philip Ferguson, for your guidance, wisdom, and understanding through this journey. I appreciate the opportunity to gain invaluable experience through being a part of STARLab; not just in engineering, but in life as well. I would also like to thank my friends and colleagues at STARLab through the years; Andrew Bowman, Martin Tkach, Sajad Saraygordafshari, Mitesh Patel, Aref Asgari, Yujia Huang, Shakiba Ahmadi, Riley Sweeney, and Jaime Campos, just to name a few. Lastly, I would like to thank my parents, Michele and James, and my brother Calvin for their wisdom and support in my personal life.

Contents

List of Figures

List of Tables

Chapter 1

Introduction

This chapter details the motivation, objectives, and main contributions of my thesis. Finally, an outline for the rest of the remaining chapters is provided at the end.

1.1 Motivation

Space based systems have become critical infrastructure to society; communication, navigation, and environmental monitoring are all vital for modern industry and military operations. The disruption of such services would have a substantial negative impact on the world's largest economies [1]. Space-based infrastructure has become so critical that several state military branches have been formed with the protection of such assets a primary focus, such as the United States Space Force [2], the French Space Command [3], the Russian Space Forces, and China's People's Liberation Army Aerospace Force.

The greatest threat to near-Earth space infrastructure, other than a direct attack, is the environment. Near Earth orbits have become increasingly congested by resident space objects (RSOs). RSOs can be classified as natural objects such as meteoroids and asteroids, active spacecraft with orbital control systems, active spacecraft without orbital control systems, and inactive spacecraft such as spent rocket bodies, defunct satellites, or space debris. Orbits relatively close to Earth, known as low Earth orbit (LEO) have become the most congested in modern times [4]. In particular, a subset of LEO known as sun-synchronous orbits (SSOs) are favoured by spacecraft operators for maximizing solar power generation and minimizing solar fluctuations during remote sensing. Unfortunately, as a consequence of their popularity, SSOs are becoming rapidly congested [4]. Orbit congestion increases the risk of collisions between resident space objects (RSOs), which are disastrous both for the colliding RSOs and for surrounding spacecraft which may collide with the resulting debris field.

Historically most collision events have been intentional, resulting from tests of anti-satellite weapons capabilities, such as the destruction of Fengyun-1C in 2007 [5]. However, collisions between spacecraft have also resulted in significant amounts of debris, particularly the collision between Kosmos 2251 and Iridium 33 in 2009 [4].

The debris generated from collisions substantially increases the amount of RSOs, increasing the risk of future unintended collisions. This positive feedback loop is a key concern for spacecraft operators trying to manage mission risk. A scenario in which regions of near Earth space become so congested that they are completely inhospitable to all spacecraft for decades or even centuries is known as Kessler syndrome [6]. Kessler syndrome represents the worst case of an exponential increase in uncontrollable RSOs [6].

Mitigating RSO collision risk is central to preventing the proliferation of space debris. Passive methods of mitigation include improving spacecraft structure construction to limit the impact of debris generated in the event of a collision [7]. Active mitigation efforts focus on reducing the probability of collisions occurring in the first place by implementing spacecraft maneuvers with controllable RSOs to avoid collisions or by implementing systems to actively remove defunct RSOs from the environment. For instance, the Federal Communications Commission has implemented a five year de-orbit requirement for spacecraft after the end of their life-time [8]. Likewise, the United Nations provides guidelines for the prevention of space debris, notably suggesting a de-orbit timeline of no more than 25 years and suggesting spacecraft implement components to enhance track-ability [9]. Active mitigation methods require detailed information about the locations and trajectories of RSOs to accurately plan maneuvers on active RSOs to avoid collisions. The ability to track, catalog and predict the movement of RSOs is referred to as space situational awareness (SSA). The majority of SSA infrastructure is ground-based, combining measurements from a network of radar [10], laser [11], and optical [12] arrays with statistical dynamic predictions. The most well known of such networks is the United States Space Surveillance Network (SSN) [13]. Canada is also a leader in this area with the NEOSSat [14] and Sapphire [15] spacecraft launched in 2013 to image and track RSOs from space. Further, Defence Reserach and Development Canada, in collaboration with the United Kingdom's Defence Science and Technology Laboratory (DSTL), Magellan Aerospace, and the University of Manitoba have announced in 2024 the Redwing and Little Innovator in Space Situational Awareness (LISSA) mission [16].

The culmination of ground-based observer measurements results in two-line element sets (TLEs) which provide time-stamped information on an RSOs position and velocity in a compact, industry-standard format. Dynamic models such as SGP4 [17] are used to propagate TLEs through time to predict future positions of RSOs. Although orbital dynamics are relatively well defined, TLEs require consistent updating due to model inaccuracies caused by atmospheric drag, magnetic field shifts, and gravitational effects [17], [18]. Current errors in TLE propagation have been sufficient to mischaracterize the risk of collisions, such was the case with the collision of Kosmos 2251 and Iridium 33 where a predicted near miss was, in reality, a catastrophic collision [19]. Implementing novel technologies that improve the accuracy and update frequency of TLEs is one way to lower the likelihood of RSO collisions occurring.

The focus of this thesis is on establishing the feasibility of space-based laser ranging systems to enhance SSA capabilities and improve the accuracy of TLEs. This thesis expands upon previous work I completed, exploring the capability of a combined laser rangefinder and cueing camera system for RSO tracking. A portion of this previous work was conducted as part of the Special Processes and Advanced Computing Environment for Debris Unambiguity, Surveying, and Tracking (SPACEDUST) initiative and was presented at the Advanced Maui Optical and Space Surveillance Technologies Conference (AMOSTech) [20]. SPACEDUST was an initiative exploring novel space debris detection technologies funded by the Department of National Defence (DND) of Canada in partnership with Magellan Aerospace Winnipeg, who subcontracted projects to various academic and industry partners [21]. This thesis also expands upon a search algorithm and simulation work presented at the American Institute of Aeronautics and Astronautics (AIAA) Science and Technology (SciTech) Forum and Exposition [22]. Finally, this thesis uses a geometric model I derived to study the occlusion effect of a small mirror on the ranging performance of a laser rangefinder, presented at the Institute of Electrical and Electronics Engineers (IEEE) Sensors conference [23].

1.2 Problem Statement

Ground-based laser systems are capable of ranging LEO RSOs smaller than 10 cm [24], though the specific target size, surface quality, and quality of measurement are unclear. In general, it is documented that space debris smaller than 10 cm remains a significant challenge to track by means of radar, optical, and laser ranging [25]. These ground-based laser ranging systems can range uncooperative targets at distances up to 3000 km and retroreflective targets up to 36,000 km [26]. However, ground-based laser systems are generally limited to night-time operations and favourable weather due to requiring high contrast against the sky for RSO visibility [26]. Further, relativistic effects due to the relative speeds between observer and target, such as velocity aberration [27], and the attenuation effects of atmosphere must be taken into account for ground-based laser systems [28]. If a target is not regularly measured, these limitations can lead to tracking inaccuracies due to orbit perturbation uncertainties accumulating over time.

As discussed briefly in my previous work [22], space-based laser ranging systems have the potential to alleviate some of the drawbacks of their ground-based counterparts. The mobile nature of space-based platforms allow for a greater amount of viewable space over a period compared to a ground-based observer. Operations are simplified by considering atmospheric effects on measurements as negligible. Velocity aberration may be negligible or equally significant for space-based laser ranging dependent on the relative orbital geometries of observer and target. Less powerful lasers may be implemented on observers to range the relatively short distances from targets compared to the longer ranges required of a ground-based observer.

One of the key challenges with space-based laser ranging is the high angular speeds required to track RSOs at close range. As discussed in chapter 6, these relative angular speeds can exceed 580 deg/s for orbital distances between a LEO target and LEO observer of 1 km, decreasing to 45 deg/s for a nominal orbital distance of 20 km. Fast-steering mirrors capable of achieving these elevated angular tracking rates impact overall range performance negatively and significantly, detailed in chapter 6. Finally, small tracking windows are likely to limit target acquisition capability compared to ground-based laser ranging systems. These challenges bring in to question the feasibility of using space-based laser ranging systems to detect RSOs, particularly uncooperative RSOs such as space debris. This thesis addresses this question of feasibility through analysis, simulation, and experimentation to determine limits in ranging and target acquisition using real commercial hardware. Discussion of the broader implications of this work are provided, as well as recommendations for future work in the field and suggestions for technology improvements that may improve system feasibility.

1.3 Objectives

The purpose of my research was to investigate the feasibility and operation of steerable single point laser rangefinder systems for space situational awareness applications, with a particular interest in predictive scanning patterns. Therefore my research hypotheses were as follows:

1. A steerable single-point laser rangefinder system consisting of a laser range finder and high-accuracy steerable mirror can acquire and range targets with relative angular rates similar to those observed in low Earth orbit (LEO) conjunction events at distances exceeding 1 km. Target acquisition can be achieved by using predictive dynamics to optimize a search pattern within a dynamic uncertainty region.

2. Incorporating a target-detecting optical camera to provide pointing cues will improve system mean acquisition time and target acquisition performance by providing

higher quality uncertainty estimates compared to solely relying on target two-line element propagation.

1.3.1 Scope and Limitations

This thesis focuses on evaluating the feasibility of a single-point laser rangefinder system for SSA applications. Specifically, the work in this thesis encompasses simulation, analysis, and hardware testing:

1. Development of target acquisition algorithms for a steerable single-point laser rangefinder system, both with and without an optical cueing camera. Simulations generate and test dynamic search patterns for given uncertainty regions based on prior knowledge, namely two-line element propagation error and optical cueing camera error. These simulations are used to assess the performance of such search patterns during hypothetical LEO conjunction events.

2. Analysis evaluating key requirements trade-offs and modeling the effect of a small mirror on the ranging performance of a commercial laser rangefinder in a RSO ranging scenario.

3. Hardware experimental testing using a prototype consisting of a steerable mirror and laser rangefinder to evaluate system performance. Tests include static range performance measurements and dynamic target acquisition performance.

This research is limited to steerable single-point laser rangefinder systems and does not explore arrayed systems. Hardware tests are constrained to off-the-shelf components and their capabilities, such as mirror size, steering speed, and camera resolution. Important environmental factors for actual spacecraft hardware implementation, including radiation tolerance and thermal cycling, are not addressed. These limitations should be considered when evaluating the results of this work for operational SSA scenarios.

1.4 Main Contributions

This research advances the understanding and application of steerable single-point laser rangefinder systems for SSA through the following contributions:

1. Design, assembly, calibration, and experimental testing of a steerable laser rangefinder testbed prototype.
2. Development of an algorithm that generates dynamic search patterns using orbital dynamics, negative sensor information, and Bayesian inference.
3. Simulations to establish the feasibility of steerable single-point laser rangefinder systems consisting of a steerable mirror and laser rangefinder in conditions approximating LEO conjunction event dynamics.
4. Assessment through simulation of the improved responsiveness and target acquisition ability of steerable single-point laser rangefinder systems by integrating an optical camera for cueing information compared to relying solely on two-line element propagation.
5. Key performance parameter trade-off analysis and mathematical models with respect to competing metrics, particularly target acquisition and detectable system range.
6. Theoretical analysis of range limitations for varying targets using a steerable single-point laser rangefinder system based on commercial off-the-shelf components.
7. Hardware testing of a prototype steerable single-point laser rangefinder system, including range testing and target acquisition, to evaluate the feasibility of such systems and to validate simulation methodology.

Further applications of this research include fields implementing aim and measure operations of objects with relative motion; of note are military targeting systems, drone payload delivery, laser communications, and of course, satellite space situational awareness technologies. The methods used to determine a scanning pattern may be translated to other devices such as aiming operations for targets with defined trajectories with associated position and velocity uncertainties.

1.5 Thesis Overview

In this section, I outline the remaining content of this thesis. Chapter 2 reviews relevant literature on steerable single-point laser rangefinder systems for ranging and target acquisition for SSA operations and puts my hypotheses and contributions into context of the broader literature. The literature review provides an overview of laser ranging technologies, their existing applications in SSA, and associated challenges. Additionally, the literature review discusses optical cueing cameras for RSO target detection, tracking, and integration of cameras into a laser steering system.

Chapter 3 presents the development of a Bayesian search pattern generation algorithm that was used for target acquisition simulations. This chapter provides an overview of orbital mechanics, two-line element sets, relevant reference frames, and the orbital cases that were considered in simulations. The Bayesian search pattern algorithm is presented alongside relevant background, in particular the definition and use of a particle filter.

Chapter 4 outlines the simulation methodology used in this thesis. The relevant inputs and background for a camera-less target search and acquisition simulations are presented. Then how bins are determined for use with the Bayesian search algorithm that was presented in chapter 3. Finally, the relevant inputs and background for camera-cued target search and acquisition simulations is presented.

Chapter 5 presents the development, design, operation, and testing methodology for the steerable laser testbed prototype. The development of a general keystone error correction formula for laser beam steering is detailed. The testing methodology for prototype search and acquisition experiments is given. However, the testing methodology for the prototype ranging performance experiment is instead provided in Chapter 6.

Chapter 6 presents important trade-offs between key performance parameters and how different hardware specifications effect these performance parameters. In particular, these performance parameters are the ranging capability, scanning rate, and measurement accuracy. The ranging capability is modeled in depth, accounting for target size, target reflectivity, and mirror occlusion effects. The prototype ranging performance test methodology is presented, followed by the results of this test, which were used to validate a geometric mirror occlusion model. This geometric mirror occlusion model was then used to estimate the overall ranging capability of the prototype for various target sizes and types.

Chapter 7 presents the remaining results and discussion. Simulation and experimental results were compared to evaluate the acquisition performance of a Bayesian search relative to an Archimedes spiral when searching for a stationary target. For both stationary and moving targets, simulation and experimental results were compared using statistical hypothesis testing to assess consistency between predicted and observed acquisition performance. This consistency provided validation of the simulation model. Simulation results were used to evaluate the performance of the Bayesian search in acquiring and tracking targets in LEO conjunction events. The performance of the system with and without simulated optical camera cues is compared to assess differences in acquisition performance.

Chapter 8 summarizes the thesis by briefly reiterating the primary research objectives, contributions, and key findings.

Chapter 2

Literature Review

This chapter outlines the current state of laser ranging systems with respect to space-based systems and target tracking. It also discusses prior work on beam steering mechanisms, search and acquisition methods, tracking methods, calibration techniques, and achievable system range.

2.1 Ground and Space-Based Laser Sensing

Laser ranging of space objects by ground-based observers has been ongoing since 1964 with the successful ranging of Beacon Explorer-B [28]. Since then, high accuracy laser ranging of cooperative satellites equipped with retroreflector arrays has been used to measure Earth dynamics [29]. Notably, passive retroreflective satellites such as LAGEOS, LARES, Etalon, Starlette, and Stella [29] serve solely as targets for ground-based laser systems. The International Laser Ranging Service (ILRS) was formed due to the increased collaboration between international geodesy researchers using laser ranging [29]. In recent years the ILRS has expanded operations for some stations on their network to track non-cooperative space debris [29]. These tracking operations use search and acquisition techniques based on two-line element knowledge [30] and optical camera cueing [31].

Light Detection and Ranging (LiDAR) has been used for space-based missions measuring terrestrial weather and atmosphere, producing higher levels of detail compared to radar [32]. In their review on the history of space-based LiDAR systems, Fouladinejad et al. identify seven missions that incorporate LiDAR [32]:

- Infrared laser payloads: ICESat, ICESat-2, ACE, CALIPSO, CATS-ISS.
- Ultraviolet laser payloads: ADM-Aeolus, and EarthCARE.

These missions highlight the efficacy of infrared LiDAR on space-based platforms to accurately measure targets at high ranges. As these missions maintain a near static pointing direction and maintain view of a large target (Earth), their beam-steering capabilities do not adequately address the challenges present with tracking high-speed, relatively small RSOs.

Space-based laser systems are not limited to remote sensing missions; they are also used for optical communications links, with potential high data rates on the order of 100 Gb/s [33]. However, the narrow beam of optical communications systems necessitates fine pointing and stable control; beams are so narrow ($\approx \mu$rad divergence) that velocity aberration due to the finite speed of light must be accounted for [33], [34]. Optical satellite links establish communications between spacecraft by performing a cooperative beaconing search and acquisition procedure, ideally with a wide beamwidth laser [33], [35]. Once a link is established, the narrow communications beam will begin sending information over a high data rate connection [35]. For the purposes of my work, targets will not be actively cooperative in the manner that a beaconing receiver spacecraft is. As such, the operations of optical communications satellites provides a general basis for initial search methods, but the control used for acquisition will not be applicable to a non-cooperative target.

Finally, a few satellite laser applications can not be categorized as either direct remote sensing or optical communications. The Gravity Recover and Climate Experiment Follow On (GRACE-FO) mission consists of a pair of satellites that measure inter-satellite distances using laser interferometer, precisely mapping the Earth's gravity field [36]. The Polish ImAging SaTellites (PIAST) is a planned project incorporating three satellites capable of tracking each other for the purposes of formation flying and operational coordination by using a laser ranging payload and corner cube retroreflectors [37]. Like the aforementioned inter-satellite optical links, these missions feature constellations of satellites, typically in a leader and follower configuration. By necessity, such constellations mean that prior knowledge of satellite positions relative to one another is well known, simplifying acquisition activities compared to a general target. There is a clear gap for applying laser ranging systems to a general target with poor a priori knowledge of position and high relative velocity relative to an observer.

2.2 Beam Steering Mechanisms

A comprehensive survey on beam steering mechanisms, referred to as acquisition, tracking, and pointing (ATP) mechanisms, was produced by Kaymak et al. [38]. This survey had a focus on ATP mechanisms for communications purposes in particular but provides a general qualitative overview of the strengths and weaknesses of different mechanisms. Kaymak et al. [38] identified four distinct categories of ATP mechanisms applicable to satellite-based systems along with their benefits and drawbacks. The summary presented in Table 1 is adapted from Kaymak et al. [38].

Table 1. Summary of relevant ATP mechanisms, adapted from Kaymak et al [38]

Mechanism	**Resolution (rad)**	**Field of Regard (FOR)**	**Steer Speed**
Gimbal	$\approx 10^{-6}$	Wide	Slow
Mirror	$< 10^{-6}$	Narrow*	Fast
Gimbal-Mirror Hybrid	$< 10^{-6}$	Wide	Fast
Adaptive Optics	$\approx 10^{-9}$	Narrow	Fast

*Note: Kaymak et al. and Milaševičius & Mačiulis identify voice-coil actuated mirrors as an exception due to their wide FOR [38], [39].

Mechanical wear is a serious problem for space-based systems over the course of a mission. As such, systems relying on mechanical methods resulting in component friction and fatigue are undesirable. Of the above ATP mechanisms, gimbal-based systems result in fatigue and wear over time, whereas electromagnetically actuated mirror and adaptive optics systems mitigate wear. For the purpose of tracking RSOs moving at high relative speeds, a fast steering, wide FOR system is required. Of the systems outlined in Table

1, only voice-coil actuated mirror systems meet these requirements.

Fast steering mirrors are typically very small to minimize weight, allowing for faster steering and responsiveness. Ideally, a mirror used to steer a laser rangefinder should be large enough to cover both the emitter and receiver. A mirror that does not cover both decreases the signal-to-noise ratio, lowering the achievable range of a rangefinder, noted by Zuo & He [40]. To address this issue Zuo & He detail a design for a large, low-cost flexible printed circuit board mirror that can cover both the emitter and receiver of a laser rangefinder, however this mirror is steerable in only one axis [40]. Zuo & He's LiDAR is only proven for a distance of 50 m, a wide FOR of 60 degrees, and a resolution of 0.2 degrees [40]. Although the measured achievable range for Zuo & He's LiDAR is based on a limited testing environment, the achievable mirror resolution is not appropriate for precise, long-range space-to-space RSO detection operations.

Beam steering mirrors have been implemented in previous satellite missions. The primary instrument for ICESAT-2, the Advanced Topographic Laser Altimeter System (ATLAS), uses an active steering mirror to maintain alignment between transmit and receive beams [41]. However, despite this capability, ATLAS has a limited FoR of only 5 mrad [42]. Laser communication terminals also incorporate steering mirrors for search and acquisition, but their FoR remains limited, on the order of 1° [39], [43], [44]. These beam steering systems are designed for maintaining a narrow, focused beams rather than wide range of motion steering. There is a clear gap in the implementation of wide FoR beam steering mechanisms in space-based applications. My work addresses this gap by exploring the feasibility of a wide FoR beam steering mirror for laser ranging applications.

2.3 Search, Acquisition and Tracking

Optical communications systems provide a good basis for exploring acquisition techniques. Chapter 4 of "Free Space Optical Communications" by Kaushal et al. discusses acquisition, tracking, and pointing in depth for optical communication links [35]. In particular, Section 4.1.2 discusses four scanning techniques: continuous spiral scan, step spiral scan, segmented scan, and raster scan; noting that a spiral scan is the most efficient of these options [35]. These scanning techniques are used in the context of an actively cooperative target that is also implementing its own search for the transmitting spacecraft, effectively acting as a relay for the transmitting spacecraft's signal. These scanning patterns are ideally performed with a wide beam to reduce the amount of overall scanning, therefore resulting in faster acquisition. Laser ranging of a general target requires a round trip of a signal compared to the relay of an optical communications acquisition strategy. This round trip significantly reduces the return signal strength, further compounded if a wide divergence beam is used. Kaushal et al. note the key trade-off when designing a search and acquisition system; improvements in acquisition time cause reductions in received beam power due to wider divergence and vice versa [35]. Kaushal et al. finally identify the key parameters describing the acquisition process for a free space optical communications system: acquisition time, uncertainty area, scanning technique, and acquisition approach [35]. The evaluation of acquisition time (and acquisition probability) described by Kaushal et al. does not account for the effect of velocity uncertainty. My research accounts for velocity uncertainty by integrating a dynamic model of an orbiting spacecraft into a particle filter [45] to generate search patterns. This approach also allows for Bayesian probability updating, enabling search patterns to incorporate information from null laser ranging measurements.

Relative motion between spacecraft is an important aspect in search and acquisition planning; it informs both uncertainty area and scanning technique, and less directly acquisition time. Nayak et al. evaluate the relative motion for two space-craft in a chaser-leader configuration by analyzing the Clohessy-Wiltshire equations, casting the relative motion of the leader spacecraft in the reference frame of the chaser [46]. The purpose of this study by Nayak et al. is for precise pointing planning of a laser system to achieve accurate shape detection and edge reconstruction of a target [46]. Although my work deals with general configurations of spacecraft using numerical methods rather than a direct analysis of the Clohessy-Wiltshire equations, the reference frames presented by Nayak et al., such as the radial-transverse-normal (RSW) frame [46], are a useful basis for understanding operations. This work by Nayak et al. further demonstrates a focus on chaser-leader satellite configurations for laser system applications in literature. I address this gap in literature by simulating the trajectories of two spacecraft for several different dual orbit configurations to assess the needs and efficacy of laser ranging systems for targets with much stricter tracking requirements with restrictive tracking windows.

Once a target is acquired, the process of continually tracking becomes the primary task. The Kalman filter [47] is well established and has been widely used in navigation and tracking applications in the aerospace industry [48], [49], [50]. Gokhan & Murat demonstrated through simulation that a Kalman filter is suitable for maintaining a link between two cooperative mobile optical communication terminals [49]. This scenario of maintaining alignment between two moving targets with a narrow optical beam presents similar challenges to those faced in tracking RSOs from a space-based platform. Gokhan & Murat note that in the case of long range satellite optical communications links, the extended Kalman filter could be employed to handle the non-linearities present in orbiting spacecraft dynamics [49]. Given the extensive use of Kalman filters in tracking, there is strong justification for investigating their application in tracking a resident space object with a space-based laser ranging platform. I propose using an extended Kalman filter for continuous tracking of an acquired target after successful search and acquisition. However, this tracking aspect was left out of scope for this thesis.

2.4 Achievable Ranges for Laser Rangefinders

Several authors have performed analysis of the radar equation applied to laser rangefinders to establish theoretical ranging capability of laser systems [37], [51], [52], [53]. Zhang et al. [51] conducted an analysis establishing a maximum detection range model for a 1064 nm short-wave infrared laser ranging system intended to range space debris. Zhang et al. used the radar equation to account for atmospheric attenuation and sky background radiance effects [51]. Blanchet et al. evaluate the feasibility of a ground based laser ranging system for detecting space debris by using the radar equation to establish the capability of laser systems for detecting targets of various sizes [52]. Blanchet cites the modified radar equation presented by Degnan [54]. Driedger et al. [53] derived a simplified form of the radar equation, neglecting negligible atmospheric effects, to establish the theoretical maximum detection range of a space based optical communications laser. Wojtanowski et al. [37] evaluated the performance of a space-based laser rangefinder for the Polish ImAging SaTellites (PIAST) mission accounting for the effects of corner cube retro-reflectors on beam return. Wojtanowski et al. [37], Forrester & Hulme [55], and Degnan [56] account for diffraction caused by corner cuber retro-reflectors by analyzing the irradiance of the far field diffraction pattern (FFDP). Experimental measurement of the effect that angle of incidence has on the FFDP were performed by Wojtanowski et al. [37] and provide a robust treatment of corner cube retro-reflector irradiance. These works demonstrate the broad acceptance of the radar equation as effective analysis in the performance of a laser rangefinding system in the space situational awareness community.

Zhang et al. [51] and Blanchet et al. [52] evaluated returns for a ground-based system targeting a diffuse reflecting object; focusing on atmospheric effects, target surface, and target size properties. Whereas Driedger et al. [53] applies the radar equation to a space-based system, ignoring atmospheric effects. My research has a focus on both diffuse targets and retro-reflective targets, as such the work of Wojtanowski et al. [37] is directly relevant. However, these prior works do not account for the effect that a small beam steering mirror has on return signal strength. Because my work focuses on a space-based system using the beam-steering method of a small fast steering mirror, I also account for the effect of mirror angle and mirror size in my analysis.

Chapter 3

Bayesian Search Pattern Algorithm

Portions of this chapter have been adapted and reproduced with permission (Appendix B) from:
[22] W. M. Ediger and P. A. Ferguson, “Feasibility of space-based laser ranging for resident space object detection,” in *AIAA SCITECH 2025 Forum*. DOI: `10.2514/6.2025-1163`. eprint: `https://arc.aiaa.org/doi/pdf/10.2514/6.2025-1163`. [Online]. Available: `https://arc.aiaa.org/doi/abs/10.2514/6.2025-1163`

In this chapter, I describe the search algorithm used for Resident Space Object (RSO) search and acquisition that is explored in this thesis. First I give an introduction to stochastic processes and the filtering problem. I provide a brief description of how a particle filter can be used to incorporate Bayesian inference. I then describe the algorithm used for incorporating the absence of measurements into a particle filter for efficient search and acquisition activities.

3.1 Orbital Mechanics and Reference Frames

This section describes the basics of orbital elements and mechanics, two-line element sets, and relevant coordinate frames for space-based laser ranging activities. The discussion on orbital mechanics is based on Spacecraft Dynamics and Control by de Ruiter [18]. Here I outline the key orbital elements and dynamics used to define an orbit.

3.1.1 Orbital Mechanics

A satellite's orbit about Earth may be described by six constants, or orbital elements, the Keplerian orbital elements for orbits around Earth are as follows:

1. **Semi-major axis (a):** The semi-major axis is half the length of the orbit's major axis.

   $$a = \frac{r_a + r_p}{2} \tag{3.1}$$

   where r_a is the orbit apogee (furthest point of orbit to Earth) and r_p is the orbit perigee (closest point of orbit to Earth).

2. **Eccentricity (e):** Eccentricity describes how circular an orbit is.

   $$e = \frac{r_a - r_p}{r_a + r_p} \tag{3.2}$$

   When $e = 0$ the orbit forms a circle and $0 < e < 1$ describes an ellipse, values of $e \geq 1$ describe escape trajectories and are not relevant to this thesis.

3. **Inclination (i):** Inclination is the angle between the orbital plane and the equatorial plane of Earth.

4. **Right ascension of the ascending node (Ω):** The angle from the vernal equinox to the ascending node of the orbit, measured along the equator of Earth.

5. **Argument of perigee (ω):** The angle between the ascending node and the point of perigee.

6. **True anomaly (θ):** The angle between the ascending node and the position of the satellite in its orbit at a given time.

In simple terms, the first five of these elements describe an ellipse in three-dimensional space, with Earth at one of its foci. This ellipse traces the orbital path of an orbiting body. The sixth term, the true anomaly, defines a point on this ellipse where the body is located. A diagram of the orbit elements is presented in Figure 3.1.

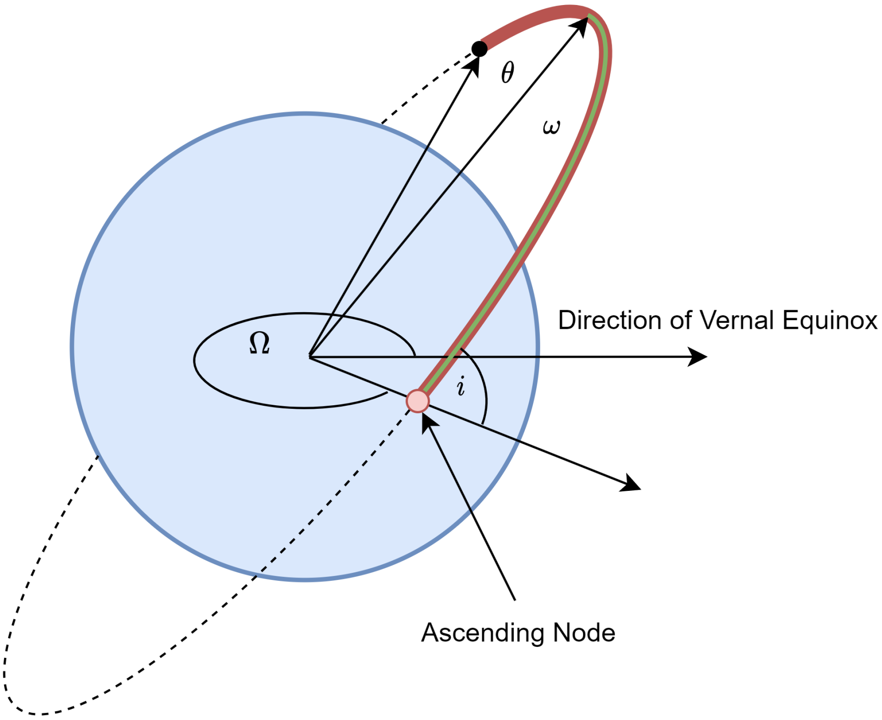

Figure 3.1. Illustration of Keplerian orbital elements

These six orbital elements can be used to calculate the position, $\vec{r}$ and velocity, $\dot{\mathbf{r}}$ of an orbiting body at a given instant. The dynamics of a body of relatively small mass orbiting Earth can be modeled by Newton's law of universal gravitation in Equation 3.3.

$$\ddot{\vec{r}} = -\frac{\mu}{|\vec{r}|^3}\vec{r} \tag{3.3}$$

where μ is the standard gravitational parameter of Earth and $\mathbf{r}$ is the location of the orbiting body with respect to the center of Earth. The above model is complicated by the presence of real, unpredictable perturbing forces. Theses perturbations include gravitational field variation, atmospheric drag, solar pressure, intentional thruster firings, and magnetic field forces. We can adjust the above equation by introducing a mass normalized perturbing force $\vec{f}$ to model these effects.

$$\ddot{\vec{r}} = -\frac{\mu}{|\vec{r}|^3}\vec{r} + \vec{f} \tag{3.4}$$

3.1.2 Two-Line Element Sets

Two Line Element Sets (TLEs) are formatted data sets that contain Resident Space Object (RSO) orbital element information. TLEs are based on RSO observations from space observation networks such as the International Laser Ranging Service (ILRS). Propagating TLEs, such as through the Simplified General Perturbation 4 (SGP4) model, is used to predict RSO trajectories and determine potential collision scenarios. The North American Aerospace Defense Command (NORAD) TLE format is defined by the line and column of a value and are detailed in Table 2 [57].

Table 2. TLE format [57]

Line 1	
Column	Description
01	Line Number
03-07	Satellite Number
08	Classification (U = Unclassified)
10-11	International Designator (Last two digits of launch year)
12-14	International Designator (Launch number of the year)
15-17	International Designator (Piece of the launch)
19-20	Epoch Year (Last two digits of year)
21-32	Epoch (Day of the year and fractional portion of the day)
34-43	First Time Derivative of the Mean Motion
45-52	Second Time Derivative of the Mean Motion (decimal point assumed)
54-61	BSTAR drag term (decimal point assumed)
63	Ephermeris type
65-68	Element number
69	Checksum (Modulo 10)
Line 2	
Column	Description
01	Line Number
03-07	Satellite Number
09-16	Inclination [Degrees]
18-25	Right Ascension of the Ascending Node [Degrees]
27-33	Eccentricity (Leading decimal point assumed)
35-42	Argument of Perigee [Degrees]
44-51	Mean Anomaly [Degrees]
53-63	Mean Motion [Revs per day]
64-68	Revolution number at epoch [Revs]
69	Checksum (Modulo 10)

3.1.3 Cowell's Method

Cowell's method [18] can be used to propagate an orbit with perturbations, with the caveat that a relatively small time-step must be used for accurate solutions.

$$\dot{\vec{r}} = \vec{v} \tag{3.5}$$

$$\dot{\vec{v}} = -\frac{\mu\vec{r}}{|\vec{r}|^3} + \vec{f} \tag{3.6}$$

where $\vec{v}$ is the velocity of the orbiting body. The above equations can be numerically integrated to achieve an orbital solution given an initial position and velocity. This technique is prone to accumulating integration inaccuracies over long time horizons, but is sufficient for short simulations with relatively small time steps.

3.1.4 Relevant Reference Frames

The Earth Centered Inertial (ECI) coordinate frame is used as the fixed, inertial coordinate frame for all my calculations. The ECI frame is defined by the fixed direction of vernal equinox, the axis of rotation of Earth, and the unit vector defined by the cross product of these two axes. The ECI frame is illustrated in Figure 3.2.

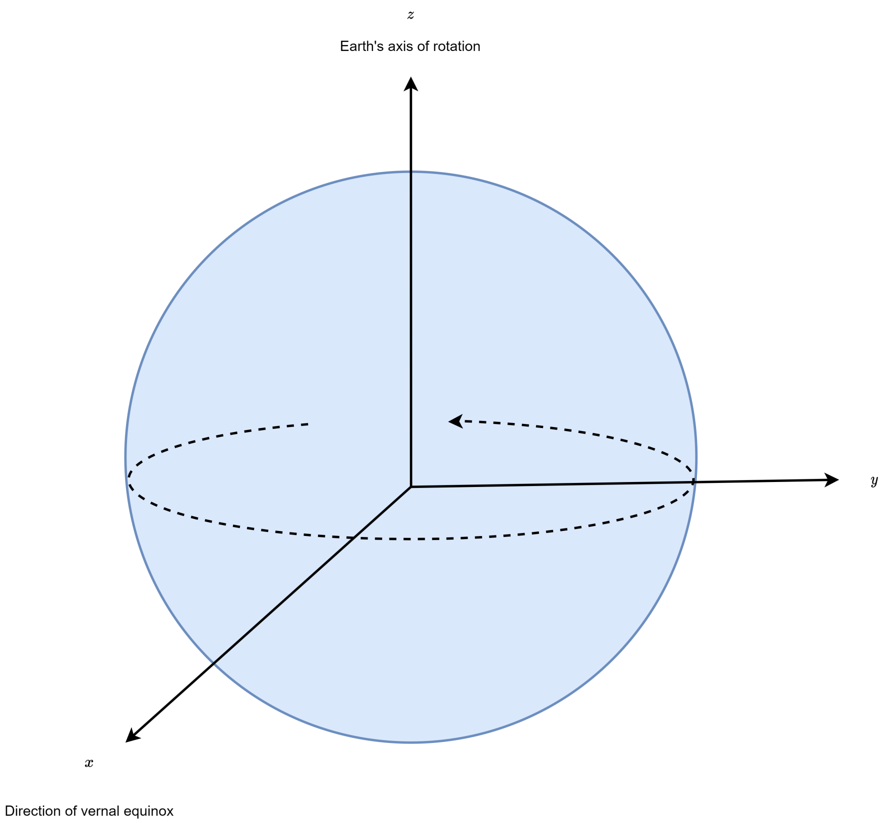

Figure 3.2. Earth centered inertial coordinate frame

Hill's coordinate frame is defined by the local satellite position and trajectory. The frame is defined by the radial direction measured from the center of Earth to the satellite, the along-track direction pointing in the direction of satellite motion, and the cross-track direction perpendicular to the orbital plane defined by the cross product of the first two unit vectors. Hill's frame is illustrated in Figure 3.3.

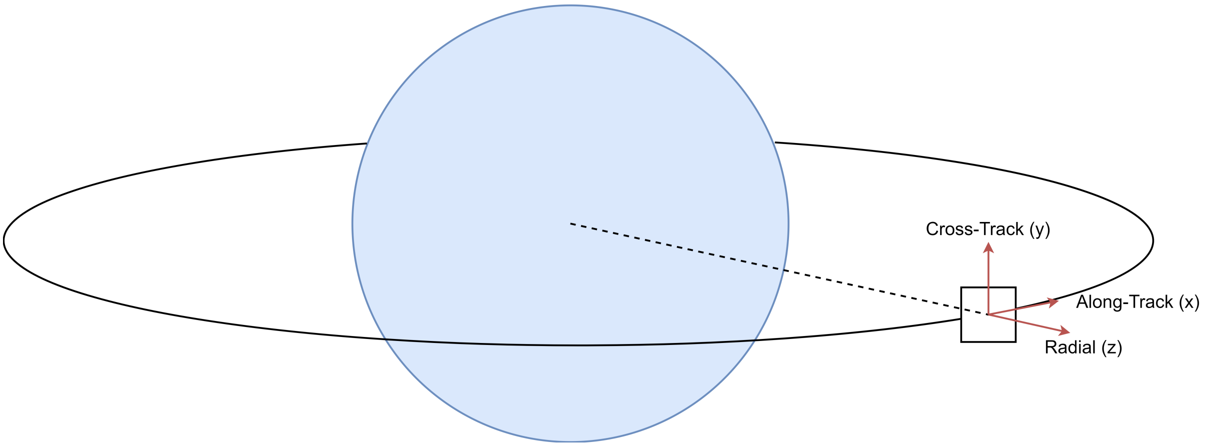

Figure 3.3. Hill's reference frame

Finally, I define the beam pointing direction of the beam steering system using a spherical coordinate system, centring the point of reflection between the laser and mirror at the observing spacecraft centroid, as illustrated in Figure 3.4. I assume the default pointing direction for the laser, z, is when the mirror is given no steering direction and is always aligned with the Hill frame radial direction. I also assume that the x axis for the laser system is always aligned with the satellite along-track direction of the Hill Frame. Then the y axis in Figure 3.4 must be aligned with the Hill frame cross-track direction. Therefore the angle between the Hill frame radial direction and the pointing angle defines the elevation angle, θ. The angle between the Hill frame along-track direction and the pointing vector projection on to the Hill frame along-track/cross-track plane defines the azimuth angle, ϕ.

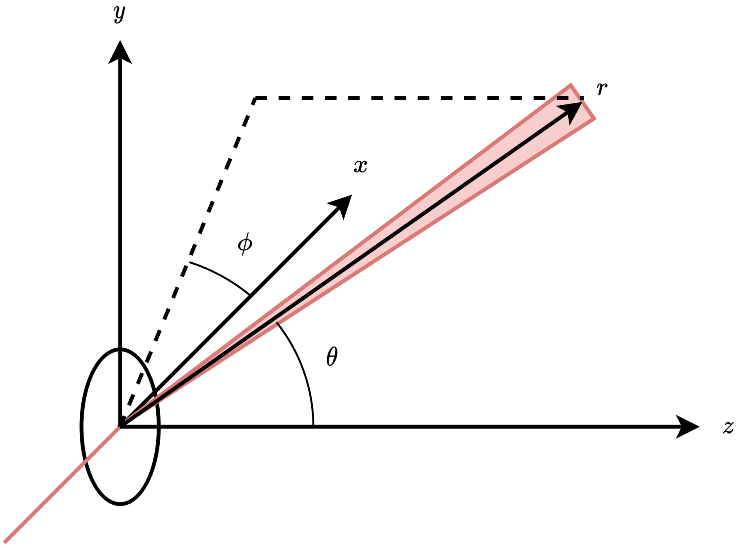

Figure 3.4. Beam steering system coordinate system, the ellipse represents the steerable mirror, vector r being the beam steering direction, defining the ray along which a conical beam exists. Axis z remains aligned with the Hill frame radial direction. θ and ϕ define elevation and azimuth angles respectively.

For clarity moving forward through this thesis I will define the following related, but distinct concepts here:

- **Beam Width:** As the light emitted from a laser travels along a ray, the energy naturally diverges from the beam centre. I refer to the width of the area illuminated by the beam at a given distance as the beam width.

- **Field of Regard (FOR):** FOR defines the boundary by which a sensing system can steer and measure within. Just because a system has a given FOR, does not mean it senses the entire FOR at the same time.

- **Field of View (FOV):** FOV defines the region that a camera can view at one given time, this is different from FOR. The entire FOV can be sensed at the same time, unlike a FOR.

The decision to adopt a spherical coordinate frame simplifies some conditional logic. The Field of Regard (FOR) defines the bounds of beam steering directions the system can take. I defined the system FOR using the specs for an Optotune MR-15-30 steerable mirror, resulting in a cone with half angle 50°. I made this choice to align these simulations with the capabilities of the prototype defined in chapter 6. In the spherical coordinate system this means that a target is within the FOR if:

$$\theta \leq 50^\circ \tag{3.7}$$

By defining the laser beam as a cone with half-angle equaling laser beam divergence half-angle α, projected from the origin of the laser system along a direction $\hat{v}$, we see that a target at position $\vec{a}$ from the satellite is within the beam if:

$$\hat{a} \cdot \hat{v} \geq \cos \alpha \tag{3.8}$$

Therefore, I define a target being acquired as any time the angle between the steered laser beam and target is less than the laser beam divergence half-angle, as illustrated in Figure 3.5.

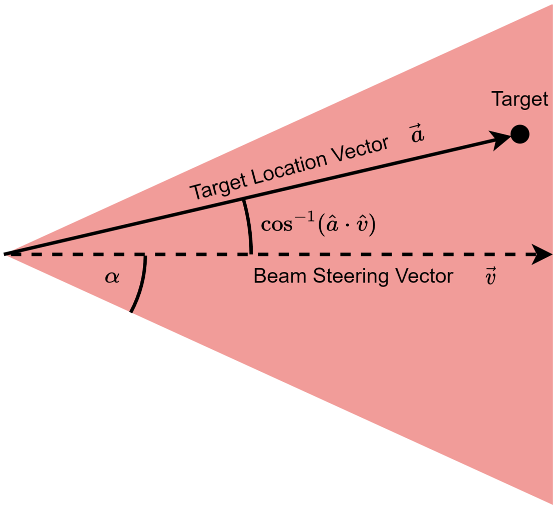

Figure 3.5. Successful target acquisition, defined by the angle between steering direction, $\vec{v}$ and target direction, $\vec{a}$ being smaller than beam half divergence α.

3.1.5 Considered Observer and Target Orbital Cases

For my research, I explored three observer orbit cases; an along-track observer in the same direction as the target (parallel), an along-track observer in the opposite direction of the target (opposite), and a cross-track observation of the target (perpendicular). This geometry is illustrated in Fig. 3.6. The observer orbiting in the opposite direction to the target presents the most challenging of scenarios as this configuration has the shortest observation window due to the high relative velocity between target and observer. I chose the Canadian satellite RADARSAT Constellation Mission-2 (RCM-2) with an initial altitude of 597 km [58] as my representative LEO target. I'll note that RCM-2 does not include retro-reflectors, but represents a well known RSO in the heavily congested sun-synchronous orbital belt of LEO. I assumed a circular orbit for the observer at altitudes of 577 km and 547 km, providing a nominal radial distance between observer and target orbits of 20 km and 50 km respectively.

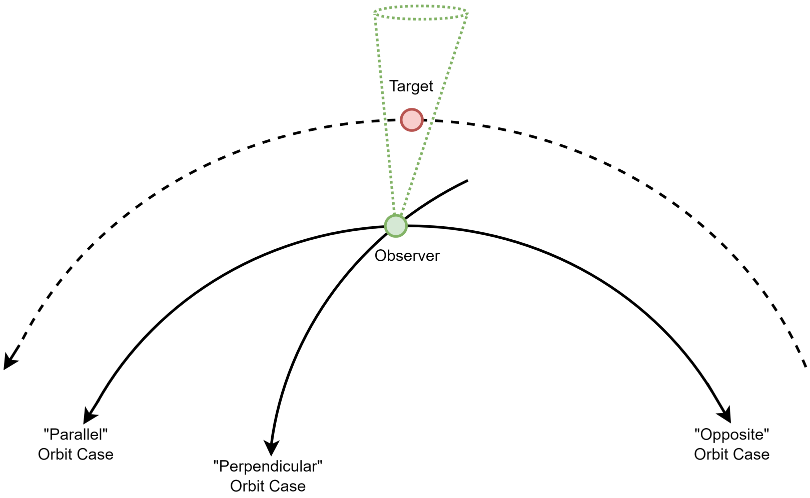

Figure 3.6. Illustration of observer orbit cases

3.2 Search and Acquisition Algorithm

In this section, I discuss relevant background to understand search, acquisition, and tracking operations. First I give an introduction to stochastic processes and the filtering problem. I then describe how to incorporate an missed measurements into a filter used for search and acquisition activities. Finally I describe the particle filter that can be used to incorporate Bayesian inference.

3.2.1 Stochastic Processes and the Filtering Problem

Classical control theory focuses on deterministic systems, being both predictable and repeatable. That is, given a certain input they always produce the same output. In contrast, stochastic processes incorporate elements of randomness, either through noise in the input or variability in the system dynamics. Due to the random nature of these processes, results must be described probabilistically. Stochastic processes are therefore described by the set of all possible values that a process can take given input and process variance. The challenge of determining the state of a system given a stochastic process is described as the filtering problem.

3.2.2 Bayesian Inference

Bayesian inference considers the likelihood that a hypothesis is true based on observed evidence. In this framework, statistical parameters such as mean and standard deviation are considered uncertain and probabilistic. In contrast, classic statistical methods consider parameters to be fixed and non-probabilistic; the mean and standard deviation of a population are fixed and not probabilistic, for instance. Bayesian inference considers two states, a priori refers to your initial knowledge of a parameter and may be described by a distribution, and post priori, which refers to your updated knowledge after making an observation. The relationship between these two states is understood by Bayes' Theorem (equation 3.9).

$$P(A|B) = \frac{P(B|A)P(A)}{P(B)} \tag{3.9}$$

where $P(A|B)$ is the probability of event A given that event B has occurred.

Target acquisition is particularly challenging when target position uncertainty is relatively large compared to beam width. One can think of this problem like trying to find a small moving object in a wide open field while only able to look through a straw. Combined with limited observation windows, leveraging all available information is crucial to achieve an observation of a target. Popular filters used for tracking applications, such as Kalman filters, require target measurements to update predictions. Unfortunately, by definition all measurements prior to acquisition will miss the target, yielding no direct information on its location. However, a lack of measurement still provides useful information about where a target is not. Bayesian updating may incorporate this type of information, referred to as negative information, to update a prior known probability distribution [59], [60]. Negative information has been used to improve performance in both tracking [59] and localization [60] applications. Beams are of finite size for a laser ranging system, therefore dividing the search space into discrete bins that are the size of these beams is appropriate. Each bin then has an associated probability, the likelihood that the target lies within a given bin. Equation 3.10 describes the Bayesian probability update for bin A, given a lack of measurement in bin B. Where $P(A)$ denotes the probability that the target lies within bin A, and $P(\bar{B})$ denotes the probability that the target does not lie within bin B.

$$P(A|\bar{B}) = \frac{P(\bar{B}|A)P(A)}{P(\bar{B})} \tag{3.10}$$

The above equation is of particular use if knowledge of the target's size is significant compared to the beam width of the emitted beam, as the probability of the target lying within bins adjacent to a searched bin also decreases, due to the possibility of a target spanning across multiple bins. However, this effect becomes very small for cases where a beam is several times wider than the target size, in which case Equation 3.10 simplifies to Equation 3.11. The beam width of our system increases by 0.8 m for every 1 km of range, and so for any significant ranging operation the beam width will be meaningfully larger than targets under 1 m in size.

$$P(A|\bar{B}) = \frac{P(A)}{1 - P(B)} \tag{3.11}$$

In this thesis I did not perform my analyses with the possibility of false negatives, that is, a measurement being returned null despite the laser striking the target. To account for the possibility of false negatives the Bayesian update equation must include the probability of a measurement being returned when measuring bin B, which I will call $P(C)$. Conversely, $P(\bar{C})$ is the probability that a measurement is null when measuring bin B. A false negative for a measurement of bin B is then $P(\bar{C}|B)$. Therefore, the update to a general bin A given a null measurement in bin B is $P(A|\bar{C})$. The Bayesian update equation for each bin could then described by Equation 3.12.

$$P(A|\bar{C}) = \frac{P(\bar{C}|A)P(A)}{P(\bar{C})} \tag{3.12}$$

$$P(A|\bar{C}) = \frac{P(\bar{C}|A)P(A)}{P(\bar{C}|B)P(B) + P(\bar{C}|\bar{B})P(\bar{B})} \tag{3.13}$$

Finally, I'll note the above equation can also account for the possibility of false positives through $P(\bar{C}|\bar{B})$. However, for all generated search patterns explored in this thesis I assumed a false negative was not possible, and so used Equation 3.11.

3.2.3 The Particle Filter

Particle filters are a robust state estimation method capable of accounting for non-Gaussian distributions, non-linear dynamics, and Bayesian updating [45]. Particle filters have precedent in aerospace applications, being employed in drone collision avoidance [61] and RSO debris tracking [62]. Whereas popular filtering methods, such as Extended Kalman Filters (EKFs), rely on linearizing dynamics and covariance propagation, leading to accumulated errors in non-linear, non-Gaussian systems, particle filters directly propagate individual states, allowing their use in highly non-linear applications. A key down-side to the immense flexibility of a particle filter is the requirements of adequate sampling and high computational effort.

The initiation of a particle filter can be simply explained as taking n representative samples from the initial state distribution. These particles are then each individually propagated given a certain dynamic model. This update is then followed by a measurement update step, either through a direct measurement or null measurement, isolating or deleting particles respectively. Finally we end with an updated distribution that numerically reflects the underlying distribution.

3.3 Particle Filter for Search Pattern Generation

To generate search patterns I begin by establishing a particle filter. Each particle contains seven elements; three position elements, three velocity elements, and one probability weight element. The probability associated with each particle is uniformly distributed. The first six elements are generated by randomly sampling values from two multivariate Gaussian distributions, one for position, and another for velocity. Details on the TLE derived statistical parameters used for these distributions can be found in section 4.3.2. These particles are explicitly independent of the bins; the bins simply divide the search space into discrete regions, each representing a possible beam location from the laser system. Note that target velocity uncertainty is important to model as variation in particle velocities cause particles to drift in to previously searched regions, requiring backtracking by the system.

The generated search pattern is a series of selected bins, defining a time-series of pointing angles for which the laser beam should be steered. This search pattern was generated by first identifying the bin most likely to contain the target, then by assuming the target does not exist within that bin and moving to the next most likely bin in the following time step. The probability distribution of the target location is updated using Bayes theorem, and the observer state and all target particles are propagated individually using Cowell's method, assuming negligible perturbation forces ($\vec{f} = 0$). This process is then repeated for subsequent time steps. Deleting particles in a bin updates the overall target probability distribution by redistributing probabilities when a target is not found within said bin. The underlying assumption for search pattern generation is that the target is never found, such that particles are continually deleted until all particles are removed or all particles have drifted outside the system FOV. The particles and observer are propagated via Cowell's method [18] using fixed step Euler integration, as given in Equations 3.14-3.16. Although Euler's method is known for accumulating numerical errors faster than higher-order integrators, all simulations presented in this thesis have short time spans (typically far less than 100 seconds) with small fixed time steps of 0.05 seconds, mitigating error accumulation.

$$\vec{a}_n = -\frac{\mu \vec{r}}{|\vec{r}|^3} \tag{3.14}$$

$$\vec{v}_{n+1} = \vec{v}_n + \vec{a}_n \Delta t \tag{3.15}$$

$$\vec{r}_{n+1} = \vec{r}_n + \vec{v}_n \Delta t + \frac{1}{2}\vec{a}_n \Delta t^2 \tag{3.16}$$

Maximum likelihood bin locations are saved to use as the system search pattern. This technique has the potential to be adapted for multiple sensors across multiple spacecraft, or to generate patterns when multiple targets are expected within a FOR, although such analysis is out of the scope of this work. An illustration of the search pattern generation algorithm is given in Figure 3.7.

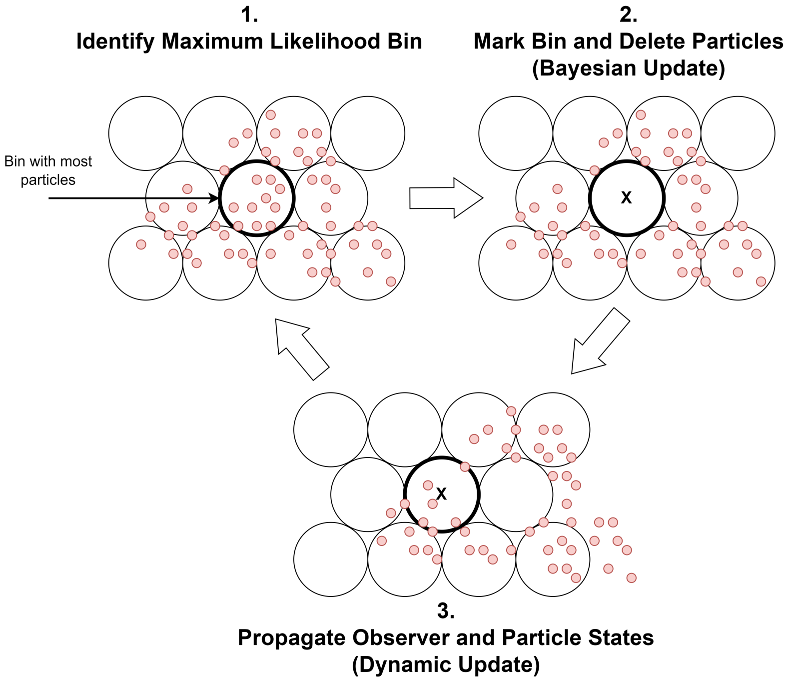

Figure 3.7. Illustration of search pattern generation algorithm, large circles represent individual bins, small red circles represent individual particles.

Chapter 4

Simulation Methodology

> Portions of this chapter have been adapted and reproduced with permission (Appendix B) from:
> [22] W. M. Ediger and P. A. Ferguson, “Feasibility of space-based laser ranging for resident space object detection,” in *AIAA SCITECH 2025 Forum.* DOI: `10.2514/6.2025-1163`. eprint: `https://arc.aiaa.org/doi/pdf/10.2514/6.2025-1163`. [Online]. Available: `https://arc.aiaa.org/doi/abs/10.2514/6.2025-1163`

In this chapter I describe the general methodology used for search, acquisition, and tracking simulations. I begin by characterizing relevant uncertainties used for particle filter initialization and updating. Refer to section 3.3 for details on the filter and algorithm used. Finally, I provide an overview on the entire simulation methodology and process for evaluating search, acquisition, and tracking performance.

4.1 TLE Based Simulation Method

In my simulations, I assessed target acquisition performance using a simulation model taking a Two Line Element (TLE) obtained from CelesTrak as an input [58]. The simulation assesses the capability of search patterns generated with the algorithm described in section 3.3. This search pattern is generated using the target TLE and related statistical uncertainty information about TLE position and velocity errors. The effectiveness of the generated search pattern is evaluated using a Monte Carlo simulation, again employing the same TLE and uncertainty information. Once a target is acquired I assumed that the system in practice would switch from searching to continuous tracking using an Extended

Kalman Filter (EKF). This work, however, focuses on target acquisition in particular, as acquisition remains a significant concern for system feasibility, and is pre-requisite for continuous tracking. As such, EKF continuous tracking was not explored in depth and is left for future work. Figure 4.1 provides a high-level overview of this process, including conditional logic to switch to continuous tracking.

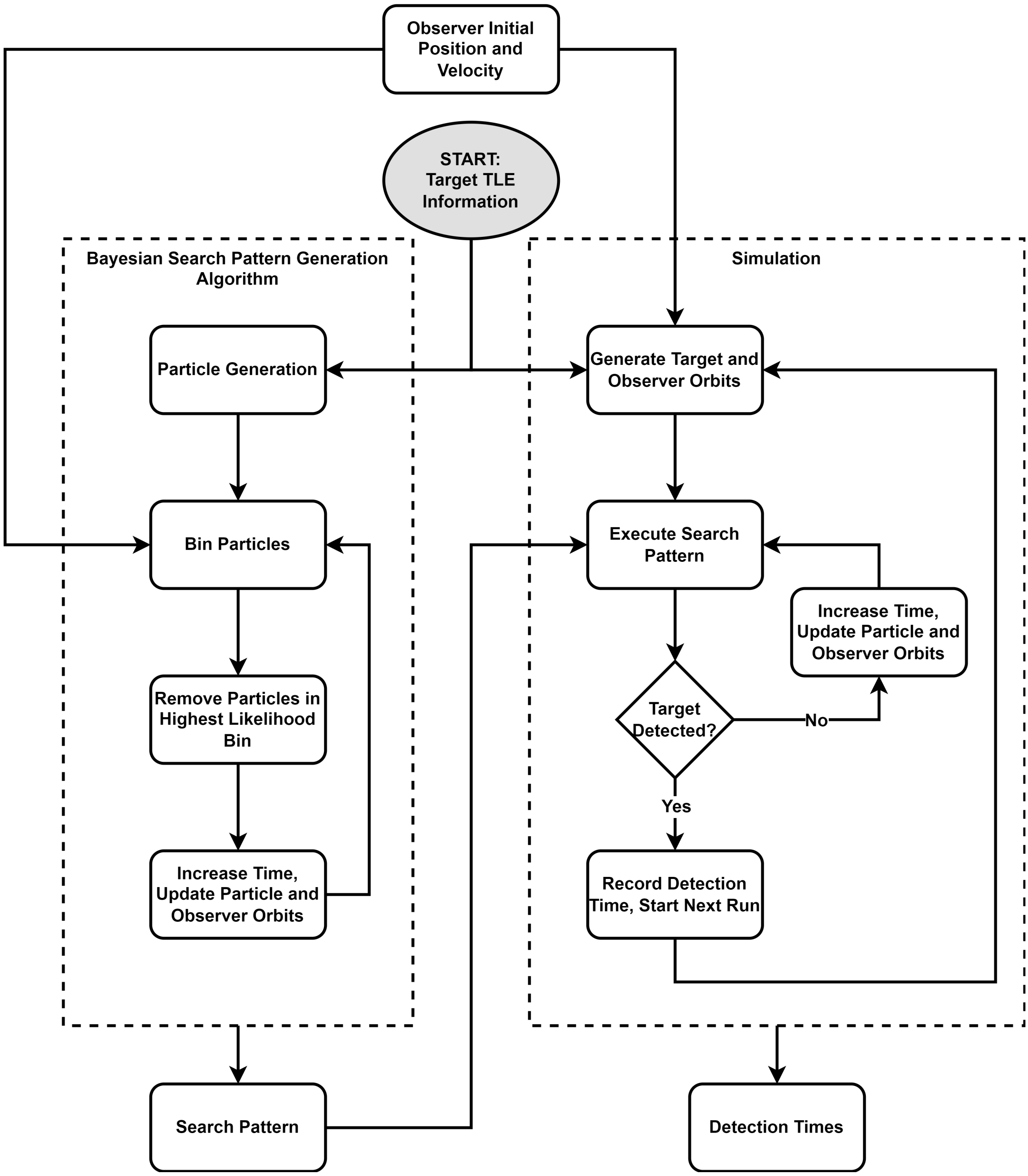

Figure 4.1. Simulation process overview, left side illustrates search pattern generation algorithm covered in Chapter 3.

The simulation results presented in Chapters 7 are based on the hardware specifications of the prototype, presented in Chapter 5. This representative system consists of a Jenoptik DLEM 20 laser rangefinder [63] and Optotune MR-15-30 fast steering mirror [64]. Key theoretical specifications of the combined system are provided in Table 5 in Section 5.1. Between the fast steering mirror and the laser rangefinder, the laser rangefinder measurement frequency of 20 Hz was the limiting factor for system measurement speed. Therefore I used a fixed time step of 0.05 seconds for both search pattern generation and Monte Carlo simulations. For all simulations the default beam axis, that is, the direction of the outgoing laser beam from the system when the steering mirror has zero tip or tilt, was fixed along the observing satellite's radial direction.

There were a few key assumptions and simplifications I implemented for search pattern generation. Primarily I assumed no measurement noise, meaning that if a target is not detected it is assumed to not be present with 100% certainty. I also assumed negligible dynamic modeling uncertainty when propagating orbits using Cowell's method, given that relevant search windows are extremely short, typically well under five minutes. Importantly, I assumed infinite beam range for both search pattern generation and Monte Carlo simulation. I defined detection solely by whether or not a target fell within the beam divergence cone for a given pointing angle at a given time step. Finally, I did not resample the particle filter, causing total particle attrition and subsequent search performance degradation for searches over long time windows, specifically in the "parallel" orbital case (see Section 3.1.5).

4.1.1 Monte Carlo Simulation

I expected that an increasing number of particles should increase search pattern performance, albeit with diminishing returns. Evaluation of this convergence helps to validate the search pattern generation technique by demonstrating its ability to approximate an effective pattern. I also expected that evaluating the true search pattern success rate directly from expended particles during search pattern generation would over-predict target acquisition success rates. Therefore, I used Monte Carlo simulations to compare the performance of generated search patterns more reliably than directly comparing particle filter acquisition rates.

The Monte Carlo method [65] involves taking a large amount of repeated random samples to estimate statistical properties. Because Monte Carlo methods only rely on stochastic inputs and a good system definition, they are useful in approximating solutions in applications with high uncertainty and complexity.

I conducted Monte Carlo simulations by generating a target based on initial TLE position and velocity uncertainty. I propagated the orbits of both the observer and each target individually using Cowell's method [18] integrated through a MATLAB Simulink model using a fixed step fourth order Runge-Kutta. In these simulations the observing spacecraft executed the same search pattern across 10,000 runs of the simulation, and the time of first acquisition for each scenario was recorded. Each run generated a different target, therefore causing variability in performance between simulation runs.

4.1.2 Two Line Element Position and Velocity Uncertainty

I required an initial target position and velocity uncertainty estimate to conduct both search pattern generation and Monte Carlo simulation. I examined expected errors associated with one day old LEO TLE data. TLE position uncertainty has been explored extensively by a variety of authors [66], [67], [68]. However velocity uncertainty is not well documented. I estimated mean velocity standard error using the derivative of mean motion. The mean motion of an orbit is simply the average angular speed of an orbiting body over a full orbit. The mean motion derivative (n') for a tracked body can be found directly from line 1, columns 34-43 of a TLE. This mean motion derivative from a TLE is halved and in units of revolutions per day squared, therefore I converted the mean motion derivative to rad/s^2, symbolized by $\dot{n}$, given in Equation 4.1.

$$\dot{n} = \frac{4\pi n'}{86,400^2} \tag{4.1}$$

Then I estimated the 1-sigma velocity error, σ_v, for a TLE after a single day by Equation 4.2, where r is the target orbit radius and Δt is the amount of seconds in a day (86,400 seconds).

$$\sigma_v = \Delta V \approx \dot{n} r \Delta t \tag{4.2}$$

$$\Delta V \approx (86,400)\dot{n} r \tag{4.3}$$

I assume the estimated 1-sigma velocity error from Eq. 4.2 was primarily along-track error. I approximated radial and cross-track velocity error was as 10% of the along-track error, as no independent estimates for these components were available. I assumed this 10% scaling to represent the possibility of smaller radial and cross-track error components, as along-track error should dominate, with 10% chosen arbitrarily. Table 3 summarizes the target TLE position and velocity uncertainties.

Table 3. TLE uncertainty with respect to satellite orbit frame

Parameter	**Radial**	**Along-Track**	**Cross-Track**
Position 1-σ (m) [66]	102	471	126
Velocity 1-σ (m/s)	$(8,640)\dot{n}r$	$(86,400)\dot{n}r$	$(8,640)\dot{n}r$

4.1.3 Parameters of Interest

There are some key parameters to assess when analyzing the capability of generated search patterns. I define a search window as the total amount of time a target remains in the observing system's Field of Regard (FOR). An important parameter to evaluate is the overall success rate of target acquisition, characterizing the ability of a search pattern to consistently acquire a target over a given search window. Related is the mean acquisition time, based only on the cases where a target is acquired. Finally, analyzing the standard deviation of acquisition time and total search window time provides a complete view of how acquisition events are distributed over a search window.

4.2 Spherical Surface Bin Generation

To execute the search pattern generation algorithm, bins must be generated over a spherical surface. While there are simple geometric tessellations for a circular beam over a flat surface, the problem faced here is tessellation over a spherical surface. This is not a trivial geometric problem, however an approximate solution for relative even spacing over a sphere can be obtained using a Fibonacci lattice [69]. Equation 4.5 provides the Fibonacci lattice equations, defining the azimuth (ϕ), and elevation (θ) angles, for $2N+1$ points distributed along a spherical surface. I used these points to define bin center locations over the spherical surface.

$$\phi_i = \frac{4\pi i}{1+\sqrt{5}} \tag{4.4}$$

$$\theta_i = \cos^{-1}\left(\frac{2i}{2N+1}\right) \tag{4.5}$$

where i ranges from $\pm N$. This means that to define the Fibonacci lattice, all that is required is an estimate of the number of points to distribute $(2N+1)$. I estimated the amount of points required by taking the ratio of FOR area to the area of a single beam. Both FOR and beam areas are described by the surface area of a spherical cap. The system FOR is defined as $\theta \leq 50°$ and the divergence half angle defined as $\alpha = 4 \times 10^{-4}$, both specified in Table 5 of Section 5.1. The surface area of a unit sphere spherical cap with half angle β is calculated using Equation 4.6.

$$A_{FOR} = 2\pi(1-\cos\beta) \tag{4.6}$$

Then I calculated the ratio of FOR to beam area, the number of bins in the FOR being n.

$$n = \frac{A_{FOR}}{A_{beam}} \tag{4.7}$$

$$n = \frac{1 - \cos(50^\circ)}{1 - \cos\alpha} \tag{4.8}$$

$$n = 4,465,155 \tag{4.9}$$

The simulation had to sift through these nearly 4.5 million bins for each time step when generating a search pattern. While generating a search pattern, I limited the bins of interest to those within a conical region whose half-angle equals the maximum particle elevation angle at each time step. This was done to reduce the computational cost and time taken to generate a search pattern.

4.3 Camera-Based Simulation Methodology

There is precedence for using space-based cameras for RSO detection [70], [71], [72], however such capabilities are not widely adopted as of yet. In the context of this thesis, implementing a camera for search and acquisition has the potential to greatly improve acquisition performance compared to using solely a TLE based search. The wide field-of-view (FOV) of a camera system may allow much faster acquisition by giving a refined initial position estimate of a target compared to TLE based uncertainty. This benefit is analogous to using a widened beam for improved search and acquisition activities used by some optical link ground stations [35].

To establish whether a camera-cued system improves target acquisition I simulated target acquisition for two orbiting satellites, assuming a camera measurement of the target was taken 5 seconds prior to the beginning of search. Aside from this initial camera measurement update, the search pattern generation process remains unchanged. The simulation of an observer using a camera to initiate a search pattern was similar to that detailed in Section 4.1. However, every randomly generated target should have its own modeled camera measurement, used to update the initial target position uncertainty from the baseline TLE uncertainty. Therefore, the search pattern generated for each target was different, unique to their target's modeled camera measurement.

Before modeling the camera measurement, I randomly selected one particle as the true target that the camera measurement model will be based on. I refer to this selected particle as the true target going forward, as it is used in each run to determine if the generated search is successful or not. I then performed the simulation for an observer using an initial camera based measurement by iterating the following steps for 1,000 runs:

1. Generate TLE based particle distribution.
2. Select a random particle from TLE distribution as true target.
3. Define the vector between the observer starting location and the true target location.
4. Model the camera measurement as a single illuminated pixel.
5. Update the priori TLE distribution using the modeled camera measurement.
6. Run the search pattern generation algorithm.
7. During each step of the search pattern generation, check whether the true target lies within the current search pattern beam.
8. If the true target lies within the search pattern beam, record a hit, the hit time, and end the current run.

The details of the new steps in this process are described in the following subsections.

4.3.1 Camera Measurement Uncertainty Model

For my simulations I used the specifications of the Fast Aural Imager (FAI) on board the CASSIOPE satellite. I decided to use the FAI as a representative camera as there has been a lot of interest and work exploring the feasibility of using FAI for RSO detection already [70], [71], [72]. The relevant specifications for the FAI can be found below in Table 4.

Table 4. CASSIOPE FAI Key Specifications [72]

Parameter	Value
Pixels	256× 256
Aperture Diameter	1.7 cm
Pixel size	26 μm
Effective focal length	1.38 cm

The instantaneous field of view (IFOV) is the angular size of one pixel. For a single pixel of CASSIOPEs FAI I calculated the IFOV with Equation 4.10 [72]:

$$IFOV = \frac{\text{pixel size}}{\text{focal length}} \tag{4.10}$$

$$IFOV = \frac{26 \times 10^{-6}}{1.38 \times 10^{-2}} \tag{4.11}$$

$$IFOV = 0.00188 \text{ rad} = 0.108^\circ \tag{4.12}$$

To justify when treating the target as a point source is appropriate I considered a target with a nominal diameter of 1 metre. For the case where the distance between observer and target, R, is much larger than 1 metre:

$$\text{target angular size} \approx \frac{1}{R} \tag{4.13}$$

Then the angular size of the target is smaller than the size of a pixel when the distance between observer and target is:

$$IFOV > \text{target angular size} \tag{4.14}$$

$$0.00188 > \frac{1}{R} \tag{4.15}$$

$$R > \frac{1}{0.00188} \tag{4.16}$$

$$R > 532 \text{ m} \tag{4.17}$$

For all the orbital cases I considered, the closest pass distances much larger than 532 metres, therefore I considered treating the target as a point source was appropriate.

The theoretical angular size of a diffraction-limited image can be found by calculating the full width at half maximum (FWHM) of an Airy disk [73]. I calculated the Airy disk FWHM using Equation 4.18 [73], where λ is the wavelength of light, and d is the aperture diameter. I used $\lambda = 700$ nm to represent red visible light, yielding a more conservative estimate of the diffraction-limited spread as a larger wavelength increases the size of the FWHM.

$$FWHM = 1.03\frac{\lambda}{d} \tag{4.18}$$

$$FWHM = 1.03\frac{700 \times 10^{-9}}{1.7 \times 10^{-2}} \tag{4.19}$$

$$FWHM = 4.24 \times 10^{-5} \text{ rad} = 0.00241^\circ \tag{4.20}$$

Because this diffraction-limited width is much smaller than the size of a single pixel, the Airy disk FWHM is fully captured by a single pixel. In other words, the light from a point source will only illuminate a single pixel. Therefore, I determined that the FAI is under-sampled and the image from a point source will be poorly resolved and should appear as a single pixel. This single pixel assumption is consistent with simulated FAI images of RSOs presented in Clark [72] and Clemens [70]. In this case the dominant source of uncertainty is the pixel size (quantization) error. Because quantization is the dominant driver of uncertainty I assumed a uniform uncertainty distribution over the angular area of a pixel. The standard deviation, σ_{camera} in one axis for a uniform distribution over a pixel is:

$$\sigma_{camera} = IFOV\frac{\#\text{ pixels}}{\sqrt{12}} \tag{4.21}$$

$$\sigma_{camera} = 0.00188\frac{1}{3.46} \tag{4.22}$$

$$\sigma_{camera} = 0.000543 \text{ rad} = 0.031^\circ \tag{4.23}$$

For comparison, the average uncertainty for a TLE in the along-track direction was 471 m, in the angular domain. Therefore when the distance between observer and target is much larger than 471 m, the initial angular uncertainty for the average LEO TLE is:

$$\sigma_{TLE} \approx \frac{471}{R} \tag{4.24}$$

Therefore I expect the camera to show improved performance up to a distance of:

$$\sigma_{camera} < \sigma_{TLE} \tag{4.25}$$

$$0.000543 < \frac{471}{R} \tag{4.26}$$

$$R < \frac{471}{0.000543} \tag{4.27}$$

$$R < 867400 \text{ m} \tag{4.28}$$

Based on these calculations a camera similar to FAI should show an improvement in initial uncertainty up to a range of 867.4 km. I did not assume sources of noise apart from quantization, such as those from focus, background radiation, jitter, or misalignment due to thermal expansion. These sources of noise should reduce the target acquisition performance improvements of a camera-cued search over a TLE based search. However, as long as these additional sources of noise all together are less than a magnitude higher than quantization error, the camera-cued search should still improve target acquisition performance.

4.3.2 Initial Uncertainty Bayesian Update

The initial TLE-defined uncertainty distribution, $\mathbf{X}$, is defined by a multivariate normal distribution with mean location μ, and covariance matrix, Σ. This initial TLE uncertainty distribution is described in Section 4.1.

$$\mathbf{X} = \mathcal{N}(\mu, \Sigma) \tag{4.29}$$

I modeled the uncertainty distribution of the target true position, if it were based solely on an illuminated pixel, as a uniform distribution, $\mathcal{U}$. This uniform distribution applies to a square angular region bounded by two horizontal angular bounds, a_1 and a_2, and two vertical angular bounds, b_1 and b_2. To achieve this uniform distribution in simulation, once the true target was chosen I randomly generated the angular bounds such that the target lie randomly between two vertical and horizontal angles both separated by the width of a pixel. Finally, the camera-based target uncertainty distribution, $\mathbf{M}$, can be described by Equation 4.30.

$$\mathbf{M} = \mathcal{U}(a_1, a_2, b_1, b_2) \tag{4.30}$$

Combining the TLE-defined uncertainty distribution with the additional information provided by an illuminated pixel in a camera measurement requires a Bayesian update on a particle by particle basis, as per Equation 4.31.

$$P(x|\mathbf{M}) = \frac{P(\mathbf{M}|x)P(x)}{P(\mathbf{M})} \tag{4.31}$$

where:

- $P(x|\mathbf{M})$ is the probability that particle x is the target location given measurement $\mathbf{M}$.
- $P(\mathbf{M}|x)$ is the probability that measurement $\mathbf{M}$ occurs given that particle x is the target location. This is 1 if the particle is within the pixel region and 0 if outside.
- $P(x)$ is the prior probability that particle x is the target location. This is achieved directly from sampling of the prior distribution $\mathbf{X}$.
- $P(\mathbf{M})$ is the prior probability that measurement $\mathbf{M}$ occurs, which is a constant, and can therefore be essentially ignored by normalizing the posterior distribution.

Therefore, the Bayesian update can be achieved by removing all particles from the initial TLE uncertainty that are not within the pixel bounds.

Chapter 5

Prototype Methodology

> Portions of this chapter have been adapted and reproduced with permission (Appendix B) from:
> [20] W. Ediger *et al.*, "Spacedust-laser/rf: Time of flight methods for space situational awareness," in *Proceedings of the 2023 AMOS Conference*, Copyright © 2023 Advanced Maui Optical and Space Surveillance Technologies Conference (AMOS) – www.amostech.com, Advanced Maui Optical and Space Surveillance Technologies Conference (AMOS), 2023. [Online]. Available: `https://amostech.com/2023-technical-papers/`

This chapter presents the design for a prototype steerable laser system. The prototype does not use a camera to cue steering and was used to test and validate models used for ranging performance and Bayesian search performance. This chapter also discusses the experimental methodologies used for testing the prototype.

5.1 Key Hardware Selection and Specifications

This section details the key hardware selected for the prototype and details relevant specifications for each piece. Table 5 summarizes key hardware specifics for each component of the prototype.

Table 5. Prototype key hardware specifications.

Jenoptik DLEM 20 Laser Rangefinder [63]	**Value**	**Unit**
Beam divergence half angle	0.4	mrad
Maximum measurement rate	20	Hz
Range measurement accuracy 1-σ	0.5	m
Optotune MR-15-30 Fast Steering Mirror [64]	**Value**	**Unit**
Mirror diameter	15	mm
Mirror albedo	95	%
Resolution	22	μrad
Repeatability	40	μrad
Optical FOV (circular radius)	50	°
Large angle step (20°) settling time	13	ms
Small angle step (0.1°) settling time	3	ms

5.1.1 Laser Rangefinder

The Jenoptik DLEM 20 is a low-weight, compact, and low-power commercial laser rangefinder. I could easily configure the DLEM 20 through its serial bus, allowing adjustment of measurement time, measurement frequency, and range gating.

5.1.2 Fast-Steering Mirror

The Optotune MR-15-30 is a lightweight, compact, fast-steering mirror suitable for small mobile platforms. The MR-15-30 has been implemented in other fine-pointing laser applications such as medical devices, optical communication systems, and automotive control systems [64]. The Optotune MR-15-30 is a tip and tilt mirror, allowing a beam to be steered along two axes. This mirror has a maximum optical deflection angle of 50 degrees in both axes, providing a FOR comparable to the OAK-1W optical cueing camera FOV. The most pressing issue with the Optotune MR-15-30, and wide FOV fast-steering mirrors more generally, is the small size of the mirror compared to the laser emitter and receiver, adversely effecting maximum detectable ranges. The implications of the mirror size on detectable ranges is derived and analyzed in Chapter 6.

5.2 Prototype Design

The prototype was created to test ranging performance and target acquisition without camera cueing. This assembly consisted of the Optotune MR-15-30 FSM and Jenoptik DLEM 20 LRF, as well as a stepper motor to precisely adjust the LRF relative to the mirror along one axis. The prototype was used for experimental detectable range testing and search pattern performance testing. For search pattern performance testing the LRF was changed out for a laser pointer. An annotated photo of the prototype can be seen in Figure 5.1.

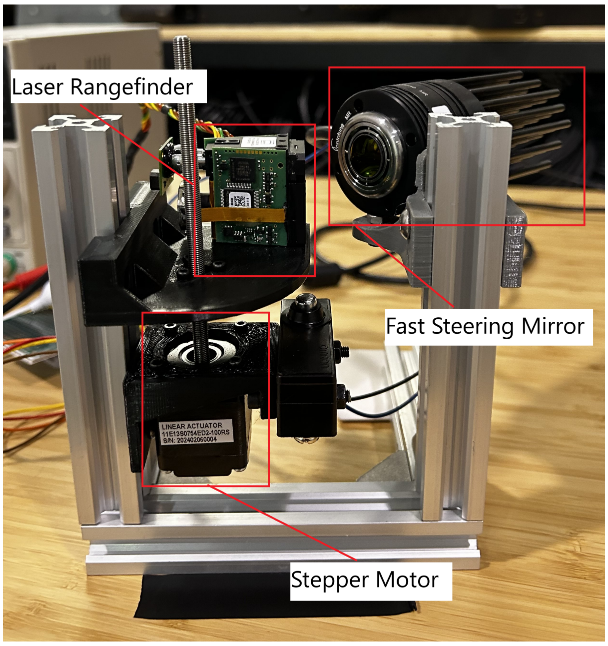

Figure 5.1. Annotated prototype assembly, stepper motor was used to position the LRF relative to the FSM for range testing.

5.3 Mirror Steering Coordinate System and Keystone Error

This section details the mirror steering coordinate system used to control the Optotune FSM, as defined by Optotune. I also provide a derivation of the non-linear distortion caused by placing the beam at a general incident angle relative to the mirror resting position. I refer to this distortion as keystone error, as it is similar to the familiar distortion seen when projecting images on to a tilted plane by the same name [74].

5.3.1 Mirror Coordinate System

The Optotune MR-15-30 is steered by specifying two input voltages, one to control the horizontal (X) axis of the mirror and the other controlling the vertical (Y) axis. An operator coding the mirror would specify two steering angles rather than a direct voltage. This input angle is described in the operations manual for the Optotune MR-15-30 [75] using the optical angle of the mirror, which is twice the tilt angle. The command, (X,Y), to steer the mirror is defined by linear coordinates with the following transformation relating to the horizontal axis mirror tilt angle (θ_x) and vertical axis mirror tilt angle ($theta_y$). Note that these angles, θ_x and θ_y, are defined by the angle of reflection of a hypothetical beam aimed head on to the mirror, rather than the physical mirror tip/tilt angles. The definition of θ_x and θ_y is illustrated in Figure 5.2.

$$X = \frac{\tan(\theta_x)}{\tan(50°)}, \quad Y = \frac{\tan(\theta_y)}{\tan(50°)} \tag{5.1}$$

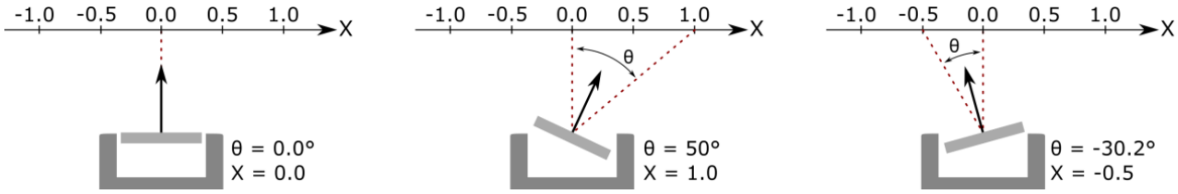

Figure 5.2. Diagram from Optotune MR-15-30 manual [75] showing Optotune mirror at different tilt angles and the corresponding X and θ_x values. Note in this image that θ is θ_x. Note that θ_x does not correspond to the arrow that denotes the mirror surface outward normal vector, but rather the direction of a reflected beam striking the mirror vertically.

The maximum optical angle achievable by the mirror is 50°, therefore the bounds for the Optotune mirror are defined by the circle:

$$X^2 + Y^2 = 1 \tag{5.2}$$

To derive the reflection equation I considered a fixed vector representing a beam, $\hat{b}$, and the mirror surface outward normal vector, $\hat{m}$, and note how changing $\hat{m}$ changes the reflected beam vector, $\hat{r}$, as illustrated in Figure 5.3.

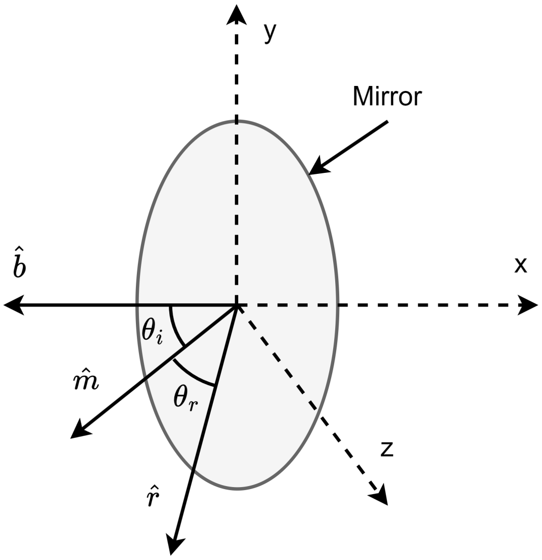

Figure 5.3. Keystone error description coordinate system.

Firstly, the reflection vector is linearly dependent on the beam and mirror surface vectors since all three unit vectors must be co-planar.

$$\hat{r} = A\hat{b} + B\hat{m} \tag{5.3}$$

Secondly, from the law of reflection $\cos\theta_i = \cos\theta_r$ and therefore:

$$\hat{r} \cdot \hat{m} = \hat{b} \cdot \hat{m} \tag{5.4}$$

The synthesis of the above two equations then yields:

$$A\hat{b} \cdot \hat{m} + B\hat{m} \cdot \hat{m} = \hat{b} \cdot \hat{m} \tag{5.5}$$

$$A\hat{b} \cdot \hat{m} + B = \hat{b} \cdot \hat{m} \tag{5.6}$$

$$B = (1 - A)\hat{b} \cdot \hat{m} \tag{5.7}$$

Finally, from the law of reflection, the angle between incident and reflected rays is twice that of the incident angle:

$$\hat{r} \cdot \hat{b} = \cos(2\theta_i) \tag{5.8}$$

$$(A\hat{b} + B\hat{m}) \cdot \hat{b} = 2\cos^2\theta_i - 1 \tag{5.9}$$

$$A\hat{b} \cdot \hat{b} + B\hat{m} \cdot \hat{b} = 2(\hat{b} \cdot \hat{m})^2 - 1 \tag{5.10}$$

$$A + (1 - A)(\hat{b} \cdot \hat{m})^2 = 2(\hat{b} \cdot \hat{m})^2 - 1 \tag{5.11}$$

$$(1 + A)(\hat{b} \cdot \hat{m})^2 = 1 + A \tag{5.12}$$

Since $\hat{b} \cdot \hat{m} \neq 0$ it follows that:

$$A = -1 \tag{5.13}$$

and

$$B = 2(\hat{b} \cdot \hat{m}) \tag{5.14}$$

Yielding the final key reflection equation:

$$\hat{r} = 2(\hat{b} \cdot \hat{m})\hat{m} - \hat{b} \tag{5.15}$$

Using the above reflection equation, I can now figure out the relationship between the mirror outward normal vector, $\hat{m}$, and the command angles, θ_x and θ_y. The variable d is defined by the MR-15-30 manual [75] as the magnitude of the vector $< \tan\theta_x \tan\theta_y 1 >$, which is convenient for the following calculations. The definition for d is given in Equation 5.16.

$$d = \sqrt{\tan^2\theta_x + \tan^2\theta_y + 1} \tag{5.16}$$

The frame for the following derivations is fixed, with the origin placed at the mirror centre. The z axis is always fixed, outward from a plane, and defines the centre of the laser steering field of regard. The x axis of the frame is parallel to the ground, and the y axis completes a right hand Cartesian basis. The set of unit vectors, $< \hat{\imath}, \hat{\jmath}, \hat{k} >$ denote the unit vectors of this right-hand Cartesian coordinate system. Any reference to the default mirror orientation refers to the mirror outward normal direction when the control angles are both zero, $(\theta_x, \theta_y) = (0, 0)$.

The following derivation assumes the incident beam is aligned with the outward normal vector of the mirror when the command angles are both zero. This is the setup assumed in the MR-15-30 manual [75], however this configuration was not used for my prototype. This configuration is illustrated with respect to the fixed reference frame in Figure 5.4.

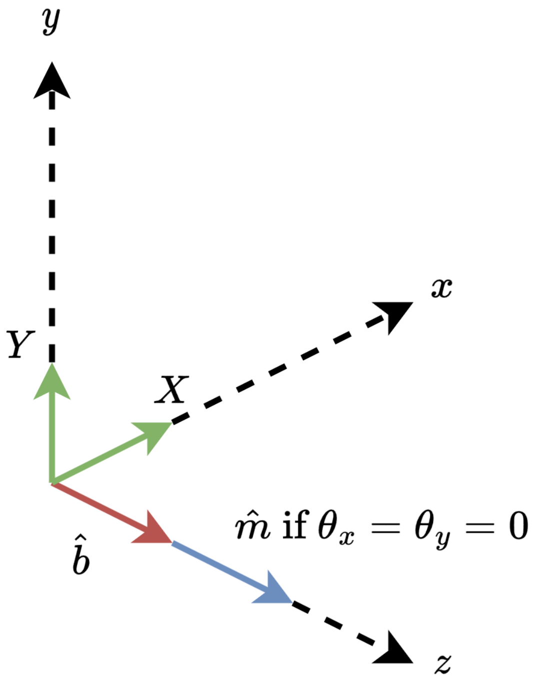

Figure 5.4. Mirror and laser configuration as defined by the MR-15-30 manual [75].

The reason I am deriving the mirror outward normal vector here using this configuration is so that I can then apply a rotation matrix, $\mathbf{R}$, to the result for a general configuration. Once $\hat{m}$ is defined for a general configuration, I can then relate the input command angles, θ_x and θ_y, to the reflected beam direction, $\hat{r}$.

$$\hat{b} = \begin{bmatrix} 0 \\ 0 \\ 1 \end{bmatrix} \tag{5.17}$$

$$\hat{r} = \frac{1}{d} \begin{bmatrix} \tan\theta_x \\ \tan\theta_y \\ 1 \end{bmatrix} \tag{5.18}$$

Then from the reflection equation, the mirror pointing direction, $\hat{m}$, can be derived:

$$2(\hat{b} \cdot \hat{m})\hat{m} - \hat{b} = \hat{r} \tag{5.19}$$

$$2(\hat{b} \cdot \hat{m})\hat{m} = \hat{r} + \hat{b} \tag{5.20}$$

$$\hat{m} = \frac{\hat{r} + \hat{b}}{|\hat{r} + \hat{b}|} \tag{5.21}$$

Then using the above equation and the definition of the Optotune mirror coordinates:

$$\hat{m} = \frac{1}{\sqrt{2d(d+1)}} \begin{bmatrix} \tan\theta_x \\ \tan\theta_y \\ d+1 \end{bmatrix} \tag{5.22}$$

5.3.2 Keystone Error

Keystone error is a type of optical distortion that occurs when a mirror and projecting source are misaligned. Although this effect is described as an error in the field of projection, for beam steering this effect is just a consequence of the law of reflection. Understanding the keystone error effect is important to properly calibrate a system relative to real world coordinates, such that I can derive a transformation that takes mirror tilt angles and translates them to the beam pointing direction. To demonstrate the keystone effect I considered the path of a collimated beam reflecting off an ideal mirror for various mirror angles relative to the beam. **R** is a rotation matrix defining the orientation of the mirror with input control angles equal to zero, relative to the fixed frame. To apply this rotation to the default mirror orientation, the following change must be made to $\hat{m}$:

$$\hat{m} = \frac{1}{\sqrt{2d(d+1)}}\mathbf{R}\begin{bmatrix} \tan\theta_x \\ \tan\theta_y \\ d+1 \end{bmatrix} \tag{5.23}$$

5.3.2.1 Prototype Keystone Error

For the prototype the default mirror orientation was at an angle of -45 degrees from the x axis. The two control axes of the mirror (X,Y) were also rotated by 90 degrees. Therefore the rotation matrix $\mathbf{R}$ is given in Equation 5.24. The incident laser vector was $\hat{b} = \hat{\imath}$.

$$\mathbf{R} = \mathbf{R}_Y(45^\circ)\mathbf{R}_Z(-90^\circ) = \begin{bmatrix} 0 & \frac{1}{\sqrt{2}} & \frac{1}{\sqrt{2}} \\ -1 & 0 & 0 \\ 0 & -\frac{1}{\sqrt{2}} & \frac{1}{\sqrt{2}} \end{bmatrix} \tag{5.24}$$

This configuration is illustrated in Figure 5.5.

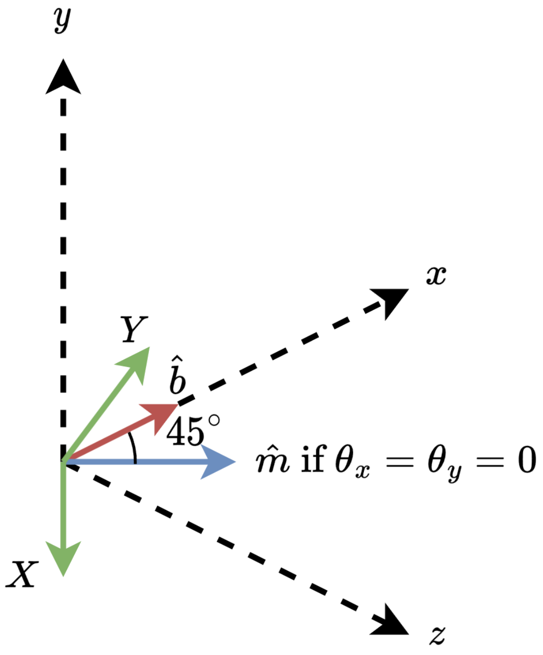

Figure 5.5. Mirror and laser configuration for the prototype.

Then the mirror pointing direction is described by:

$$\hat{m} = \frac{1}{\sqrt{2d(d+1)}} \begin{bmatrix} 0 & \frac{1}{\sqrt{2}} & \frac{1}{\sqrt{2}} \\ -1 & 0 & 0 \\ 0 & -\frac{1}{\sqrt{2}} & \frac{1}{\sqrt{2}} \end{bmatrix} \begin{bmatrix} \tan\theta_x \\ \tan\theta_y \\ d+1 \end{bmatrix} \tag{5.25}$$

$$\hat{m} = \frac{1}{2\sqrt{d(d+1)}} \begin{bmatrix} \tan\theta_y + d + 1 \\ -\sqrt{2}\tan\theta_x \\ d + 1 - \tan\theta_y \end{bmatrix} \tag{5.26}$$

Then solving for $\hat{r}$ using Equation 5.15:

$$\hat{r} = \frac{\tan\theta_y + d + 1}{2d(d+1)} \begin{bmatrix} \tan\theta_y + d + 1 \\ -\sqrt{2}\tan\theta_x \\ d + 1 - \tan\theta_y \end{bmatrix} - \begin{bmatrix} 1 \\ 0 \\ 0 \end{bmatrix} \tag{5.27}$$

$$\hat{r} = \frac{\tan\theta_y + d + 1}{2d(d+1)} \begin{bmatrix} \tan\theta_y + d + 1 - \frac{2d(d+1)}{\tan\theta_y + d + 1} \\ -\sqrt{2}\tan\theta_x \\ d + 1 - \tan\theta_y \end{bmatrix} \tag{5.28}$$

5.3.3 Inverse Keystone Correction

To steer the beam towards a desired direction I must compute the mirror steering command signals, X and Y, based on the desired beam pointing vector, $\hat{r}$. Here I note that the desired beam pointing unit vector, $\hat{r}$, can be described by its Cartesian components:

$$\hat{r} = \begin{bmatrix} \hat{r}_x \\ \hat{r}_y \\ \hat{r}_z \end{bmatrix} \tag{5.29}$$

As previously derived, the mirror surface normal is related to the incident and reflected beam vectors by:

$$\hat{m} = \frac{\hat{r} + \hat{b}}{|\hat{r} + \hat{b}|} \tag{5.30}$$

$$\hat{m} = \frac{\hat{r} + \hat{b}}{\sqrt{(\hat{r}_x + \hat{b}_x)^2 + (\hat{r}_y + \hat{b}_y)^2 + (\hat{r}_z + \hat{b}_z)^2}} \tag{5.31}$$

$$\hat{m} = \frac{\hat{r} + \hat{b}}{\sqrt{\hat{r}_x^2 + \hat{r}_y^2 + \hat{r}_z^2 + \hat{b}_x^2 + \hat{b}_y^2 + \hat{b}_z^2 + 2(\hat{r}_x\hat{b}_x + \hat{r}_y\hat{b}_y + \hat{r}_z\hat{b}_z)}} \tag{5.32}$$

$$\hat{m} = \frac{\hat{r} + \hat{b}}{\sqrt{2(1 + \hat{r} \cdot \hat{b})}} \tag{5.33}$$

Combining the above with the general definition for $\hat{m}$, accounting for rotation of the default mirror orientation:

$$\hat{m} = \frac{1}{\sqrt{2d(d+1)}}\mathbf{R}\begin{bmatrix} \tan\theta_x \\ \tan\theta_y \\ d+1 \end{bmatrix} \tag{5.34}$$

$$\frac{\hat{r} + \hat{b}}{\sqrt{2(1 + \hat{r} \cdot \hat{b})}} = \frac{1}{\sqrt{2d(d+1)}}\mathbf{R}\begin{bmatrix} \tan\theta_x \\ \tan\theta_y \\ d+1 \end{bmatrix} \tag{5.35}$$

$$\mathbf{R}^{-1}\frac{(\hat{r} + \hat{b})}{\sqrt{2(1 + \hat{r} \cdot \hat{b})}} = \frac{1}{\sqrt{2d(d+1)}}\begin{bmatrix} \tan\theta_x \\ \tan\theta_y \\ d+1 \end{bmatrix} \tag{5.36}$$

$$\tag{5.37}$$

I define the following unit vector $\hat{g}$ for notation simplicity:

$$\begin{bmatrix} \hat{g}_x \\ \hat{g}_y \\ \hat{g}_z \end{bmatrix} = \mathbf{R}^{-1}\frac{(\hat{r} + \hat{b})}{\sqrt{2(1 + \hat{r} \cdot \hat{b})}} \tag{5.38}$$

This is a system of three equations that can be solved explicitly, yielding $\tan\theta_x$, $\tan\theta_y$, and d as a functions of $\hat{r}$ and $\hat{b}$.

$$\begin{bmatrix} \hat{g}_x \\ \hat{g}_y \\ \hat{g}_z \end{bmatrix} = \frac{1}{\sqrt{2d(d+1)}} \begin{bmatrix} \tan\theta_x \\ \tan\theta_y \\ d+1 \end{bmatrix} \tag{5.39}$$

Starting with the equation from the $\hat{g}$ vector z component:

$$\hat{g}_z = \frac{d+1}{\sqrt{2d(d+1)}} \tag{5.40}$$

$$\hat{g}_z = \frac{\sqrt{d+1}}{\sqrt{2d}} \tag{5.41}$$

$$\hat{g}_z^2 = \frac{d+1}{2d} \tag{5.42}$$

$$2d\hat{g}_z^2 = d+1 \tag{5.43}$$

$$(2\hat{g}_z^2 - 1)d = 1 \tag{5.44}$$

$$d = \frac{1}{2\hat{g}_z^2 - 1} \tag{5.45}$$

The command signals are then:

$$X = \frac{\tan\theta_x}{\tan(50^\circ)} = \frac{\hat{g}_x\sqrt{2d(d+1)}}{\tan(50^\circ)} \tag{5.46}$$

$$Y = \frac{\tan\theta_y}{\tan(50^\circ)} = \frac{\hat{g}_y\sqrt{2d(d+1)}}{\tan(50^\circ)} \tag{5.47}$$

5.3.3.1 Inverse Keystone Correction for Prototype

For the prototype, the laser vector, $\hat{b}$ and the rotation matrix, $\mathbf{R}$, are:

$$\hat{b} = \hat{\imath} \tag{5.48}$$

$$\mathbf{R} = \mathbf{R}_Y(45^\circ)\mathbf{R}_Z(-90^\circ) = \begin{bmatrix} 0 & \frac{1}{\sqrt{2}} & \frac{1}{\sqrt{2}} \\ -1 & 0 & 0 \\ 0 & -\frac{1}{\sqrt{2}} & \frac{1}{\sqrt{2}} \end{bmatrix} \tag{5.49}$$

Then following the above process I found:

$$\begin{bmatrix} \hat{g}_x \\ \hat{g}_y \\ \hat{g}_z \end{bmatrix} = \mathbf{R}^{-1} \frac{(\hat{r} + \hat{b})}{\sqrt{2(1 + \hat{r} \cdot \hat{b})}} \tag{5.50}$$

$$\begin{bmatrix} \hat{g}_x \\ \hat{g}_y \\ \hat{g}_z \end{bmatrix} = \frac{1}{\sqrt{2(1 + \hat{r}_x)}} \begin{bmatrix} 0 & -1 & 0 \\ \frac{1}{\sqrt{2}} & 0 & -\frac{1}{\sqrt{2}} \\ \frac{1}{\sqrt{2}} & 0 & \frac{1}{\sqrt{2}} \end{bmatrix} \begin{bmatrix} \hat{r}_x + 1 \\ \hat{r}_y \\ \hat{r}_z \end{bmatrix} \tag{5.51}$$

$$\begin{bmatrix} \hat{g}_x \\ \hat{g}_y \\ \hat{g}_z \end{bmatrix} = \frac{1}{2\sqrt{1 + \hat{r}_x}} \begin{bmatrix} -\sqrt{2}\hat{r}_y \\ \hat{r}_x - \hat{r}_z + 1 \\ \hat{r}_x + \hat{r}_z + 1 \end{bmatrix} \tag{5.52}$$

Then I solved for d, X, and Y:

$$d = \frac{2(1 + \hat{r}_x)}{(\hat{r}_x + \hat{r}_z + 1)^2 - 2(1 + \hat{r}_x)} \tag{5.53}$$

$$X = \frac{-\hat{r}_y \sqrt{d(d+1)}}{\sqrt{1 + \hat{r}_x}\tan(50^\circ)} \tag{5.54}$$

$$Y = \frac{(\hat{r}_x - \hat{r}_z + 1)\sqrt{d(d+1)}}{\sqrt{2(1 + \hat{r}_x)}\tan(50^\circ)} \tag{5.55}$$

5.4 Prototype Testing Methods

Two types of tests were performed with the prototype. The purpose of the first test was to determine the effect of the FSM size on the ranging performance of the LRF. The purpose of the second test was to determine the real world efficacy of the Bayesian search pattern for stationary and moving targets. The focus of this second test was on target acquisition as opposed to ranging performance. For this second test the LRF was swapped for a laser pointer to allow for visual confirmation of performance and to be compatible with a light detecting diode placed on the target. In this section the search and acquisition testing methods are discussed for a stationary and a moving target. The ranging test method is detailed in Chapter 6, as it is given appropriate context there.

These acquisition tests were conducted using STARLab's Vicon motion tracking system which is capable of measuring position with sub-millimetre accuracy. The Vicon system returns time-tagged position data for objects defined by motion tracking infrared reflective markers. For all tests using the Vicon system, the prototype and target were both defined as objects for position tracking.

5.4.1 Test Environment Setup

Prior to performing these tests it was essential to align the prototype and Vicon coordinate systems. Alignment ensured that measurements obtained from the Optotune can be trusted when compared to data recorded by the Vicon system. To achieve alignment, I used a large board with orthogonal markings to ensure that the beam reflected off the default mirror orientation is level in all axes. I leveled the system by ensuring the beam hit the same point at different distances along the y-axis of the Vicon system, see Figure 5.6. I also steered the laser vertically and horizontally to ensure vertical and horizontal movements were aligned with the Vicon x and z axes.

(a) Leveling board close to prototype (b) Leveling board far from prototype

Figure 5.6. Leveling procedure

5.4.2 Stationary Target Testing Method

The target used for this test was a small rover capable of pre-coded movement. Attached to the rover was a light detecting diode which helped to establish acquisition of the target apart from visual confirmation. This rover can be seen in Figure 5.7.

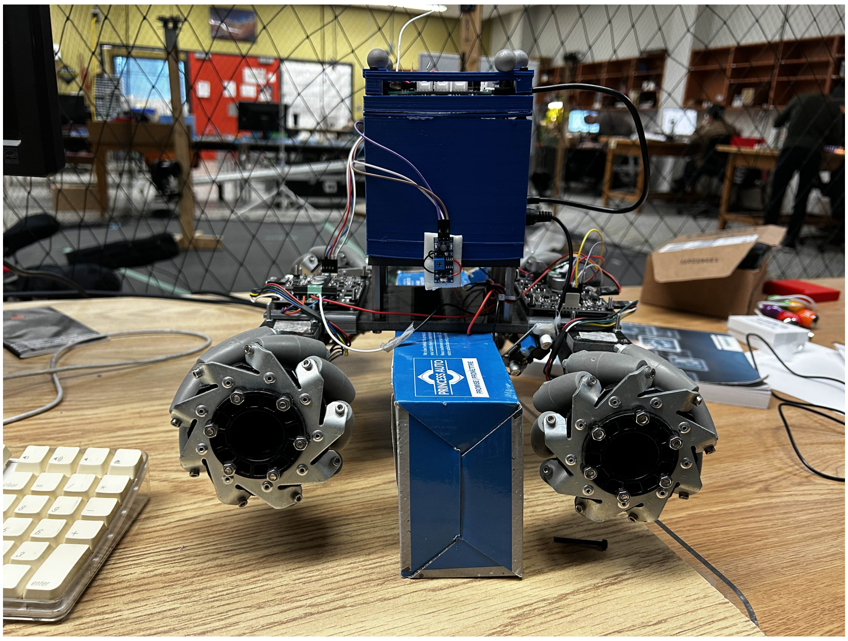

Figure 5.7. Rover used as a target for prototype testing

For the stationary target test the rover was kept stationary between runs. The purpose of this test was to establish the viability of the Bayesian search pattern generation algorithm discussed in Chapter 3 compared with an Archimedes spiral search, commonly used in optical communications [35]. Both the Bayesian search pattern and Archimedes spiral pattern were generated prior to testing. The target was moved between runs in an attempt to match the positional uncertainty used to generate the two search patterns. Ten tests of each search pattern were conducted, outputs from each run included FSM mirror angles, time-tagged light detecting diode output, and Vicon position data for both the observing prototype and target.

Because the Bayesian and Archimedes spiral search patterns were generated prior to testing I had to define initial uncertainties to generate these patterns. Using the coordinates defined in Figure 5.8, I generated the patterns using the position mean vector, μ, given by Equation 5.56, and position covariance matrix, σ, given in Equation 5.57, which defines the target mean position aligned with the default axis of the laser at a distance of 2 metres and a horizontal and vertical position standard deviation of 1 centimetres. Each generated pattern had 1,000 discrete steps, each denoting a laser pointing vector. At a nominal measurement rate of 20 Hz, this equates to each pattern taking 50 seconds to execute.

$$\mu = \begin{bmatrix} 0 \\ 0 \\ 2 \end{bmatrix} \text{ m} \tag{5.56}$$

$$\Sigma = \begin{bmatrix} 0.01^2 & 0 & 0 \\ 0 & 0.01^2 & 0 \\ 0 & 0 & 0 \end{bmatrix} \text{ m}^2 \tag{5.57}$$

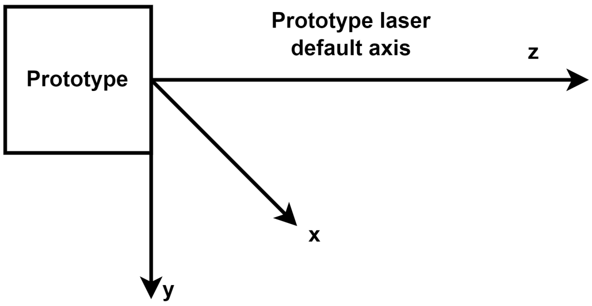

Figure 5.8. Initial uncertainty coordinate system

5.4.3 Moving Target Testing Method

The methodology for this test was also very similar to that described in Section 5.4.2. Again, the same leveling and set up procedure was used. The target used was the same small rover used in camera-less stationary target testing. In this test the rover drove from right to left at speeds varying from 100-250 mm/s, beginning at a distance of 2 metres along the default laser axis and to the right of this axis by 2 metres. The purpose of this test was to establish the viability of the Bayesian search pattern generation algorithm discussed in Chapter 3 on a moving target, compared to simulated performance of the same pattern. The Bayesian search pattern was generated prior to testing. The target was moved between runs in an attempt to match the uncertainty patterns used to generate the two search patterns. Ten tests were conducted, outputs from each run included FSM mirror angles, time-tagged light detecting diode output, and Vicon position data for both the observing prototype and target.

Again, because the Bayesian search pattern was generated prior to testing I had to define initial uncertainties to generate the pattern. Using the coordinates defined in Figure 5.8, I generated the patterns using the mean position vector, μ_p, given in Equation 5.58 to meet the above mentioned initial position of the target, and position covariance matrix, σ_p, given in Equation 5.59 to define a 5 centimetre accuracy of the initial position. Because the target is moving for these tests I also defined a velocity mean and covariance with a mean velocity to the left of 150 mm/s and an x-axis velocity standard deviation of 50 mm/s, see Equations 5.60 and 5.61 respectively. The generated pattern had 1,000 discrete steps, each denoting a laser pointing vector. At a nominal measurement rate of 10 Hz, this equates to each pattern taking 100 seconds to execute. This 10 Hz measurement rate was based on the results of the stationary testing with the prototype.

$$\mu_p = \begin{bmatrix} 2 \\ 0 \\ 2 \end{bmatrix} \text{ m} \tag{5.58}$$

$$\Sigma_p = \begin{bmatrix} 0.05^2 & 0 & 0 \\ 0 & 0.05^2 & 0 \\ 0 & 0 & 0.05^2 \end{bmatrix} \text{ m}^2 \tag{5.59}$$

$$\mu_v = \begin{bmatrix} -0.150 \\ 0 \\ 0 \end{bmatrix} \text{ m/s} \tag{5.60}$$

$$\Sigma_v = \begin{bmatrix} 0.05^2 & 0 & 0 \\ 0 & 0 & 0 \\ 0 & 0 & 0 \end{bmatrix} (\text{m/s})^2 \tag{5.61}$$

Chapter 6

Important Performance Trade-offs and Prototype Range Analysis

Portions of this chapter have been adapted and reproduced with permission (Appendix B) from:
[22] W. M. Ediger and P. A. Ferguson, "Feasibility of space-based laser ranging for resident space object detection," in *AIAA SCITECH 2025 Forum*. DOI: `10.2514/6.2025-1163`. eprint: `https://arc.aiaa.org/doi/pdf/10.2514/6.2025-1163`. [Online]. Available: `https://arc.aiaa.org/doi/abs/10.2514/6.2025-1163`
[23] W. Ediger and P. Ferguson, "Laser rangefinder and steering mirror optimization by radar and geometric modeling," in *2025 IEEE SENSORS*, 2025, pp. 1–4. DOI: `10.1109/SENSORS59705.2025.11330595` ©2025 IEEE

In this chapter I analyze the relationship and trade-offs between key performance parameters for general space-based laser ranging platforms using fast steering mirrors. The two primary requirements for a space-based laser ranging platform are to steer a beam to hit a small fast-moving target, and to also receive enough return power from the target to reliably read the range between observer and target. These two performance requirements are in competition due to fundamental hardware limitations; such as laser beam divergence, the innate relationship between time and distance in time of flight measurements, and the limited size of fast steering mirrors.

I then derive a geometric model that I used to predict the ranging capability of a laser rangefinder paired with a small fast steering mirror. To verify this model I conducted a ranging experiment using the prototype introduced in Chapter 5. I then use this model to estimate the ranging capability of the ranging prototype with respect to diffuse and retro-reflective targets.

6.1 Important Performance Trade-offs

This section outlines the trade-offs between key performance metrics for a general space-based laser ranging system. I first define the key performance parameters I will be analyzing. I then look at the relationship between these parameters in the context of a space-based laser ranging platform.

6.1.1 Key Performance Parameters

The key performance parameters I identified as being important for determining the feasibility of a general space-based laser ranging system are:

- Maximum detectable range, R_{max}, (m): The maximum range that the laser rangefinder and mirror system can detect a target. Higher maximum detectable ranges allow a greater variety of targets to be sensed by the system.
- Scanning frequency, f, (Hz): The scanning frequency is the frequency at which individual measurements occur. Scanning frequency accounts for the time required to steer the beam to a given location and the time required for all measured emissions to travel to and from the target. I expect a higher scanning frequency to improve search and acquisition performance by allowing for more measurements in the same amount of time.
- Measurement uncertainty covariance, Σ: The measurement uncertainty covariance describes the variance and correlation of measurement errors relative to the true target location.

For clarity I also define some key hardware specifications that will be referenced in this chapter:

- Angular steering speed, ω, (rad/s): The angular steering speed is how fast the laser beam can be steered in the angular domain. The angular steering speed is important both for maintaining a track on an acquired target and for performing efficient search and acquisition operations.

- Field of Regard (FOR), β, (rad): The FOR is the effective area that can be searched at once. The FOR does not define an area that is measured all at once, but rather the region in which a measurement may take place. A higher FOR allows for longer tracking windows compared to a lower FOR.

6.1.2 Performance Trade-offs in Space-Based Ranging Scenarios

To characterize how these key parameters are related I considered the orbital geometry presented in Figure 6.1, with two RSOs occupying the same orbital plane traveling opposite directions: an observer in a circular orbit of radius r_0 and a target in a circular orbit with radius r_1. This orbital geometry assumes a worst case scenario, where the target will have the shortest observation time window and be traveling at the highest possible velocity relative to the observer. Of interest is the distance between both RSOs, R, and the observation angle of the target relative to the observer θ. From its derivation later on, I define the observation angle, θ, as the angle between the vectors $\vec{r_0}$ and $\vec{R}$, as such θ is always a positive value between 0 and π.

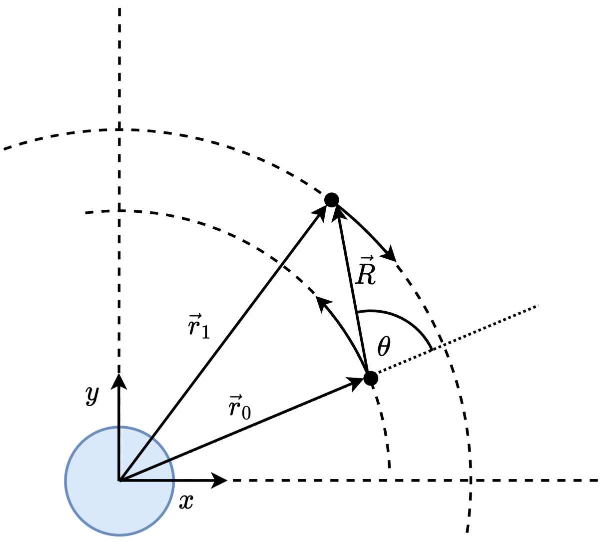

Figure 6.1. Orbital geometry of observer ($\vec{r}_0$) and target ($\vec{r}_1$), the observation angle, θ, is defined from the default viewing axis (zenith) of the observing satellite

The period, T, of a circular orbit from orbital mechanics:

$$T_i = 2\pi\sqrt{\frac{r_i^3}{\mu}} \tag{6.1}$$

where r_i is the radius of the orbit and μ is Earth's standard gravitational parameter, $\mu = 3.986 \times 10^{14}$ m^{3}s^{-2}. The orbital paths can be defined by the following from an arbitrary starting point. For convenience the conjunction of the orbits will define $t = 0$.

$$\vec{r}_0 = \begin{bmatrix} r_0 \cos\left(\frac{2\pi t}{T_0}\right) \\ r_0 \sin\left(\frac{2\pi t}{T_0}\right) \end{bmatrix}, \quad \vec{r}_1 = \begin{bmatrix} r_1 \cos\left(\frac{2\pi t}{T_1}\right) \\ -r_1 \sin\left(\frac{2\pi t}{T_1}\right) \end{bmatrix} \tag{6.2}$$

$$\vec{R} = \vec{r}_1 - \vec{r}_0 \tag{6.3}$$

$$|\vec{R}| = \sqrt{\left[r_1 \cos\left(\frac{2\pi t}{T_1}\right) - r_0 \cos\left(\frac{2\pi t}{T_0}\right)\right]^2 + \left[-r_1 \sin\left(\frac{2\pi t}{T_1}\right) - r_0 \sin\left(\frac{2\pi t}{T_0}\right)\right]^2} \tag{6.4}$$

$$\begin{aligned}|\vec{R}| = \sqrt{r_1^2 \cos^2\left(\frac{2\pi t}{T_1}\right) - 2r_1r_0 \cos\left(\frac{2\pi t}{T_1}\right)\cos\left(\frac{2\pi t}{T_0}\right) + r_0^2\cos^2\left(\frac{2\pi t}{T_0}\right) +} \\ r_1^2 \sin^2\left(\frac{2\pi t}{T_1}\right) + 2r_1r_0 \sin\left(\frac{2\pi t}{T_1}\right)\sin\left(\frac{2\pi t}{T_0}\right) + r_0^2\sin^2\left(\frac{2\pi t}{T_0}\right)\end{aligned} \tag{6.5}$$

$$|\vec{R}| = \sqrt{r_0^2 + r_1^2 + 2r_0r_1\left[\sin\left(\frac{2\pi t}{T_1}\right)\sin\left(\frac{2\pi t}{T_0}\right) - \cos\left(\frac{2\pi t}{T_1}\right)\cos\left(\frac{2\pi t}{T_0}\right)\right]} \tag{6.6}$$

$$|\vec{R}| = \sqrt{r_0^2 + r_1^2 - 2r_0r_1\left[\cos\left(\frac{2\pi t}{T_1} + \frac{2\pi t}{T_0}\right)\right]} \tag{6.7}$$

$$|\vec{R}| = \sqrt{r_0^2 + r_1^2 - 2r_0r_1\cos\left(\frac{2\pi(T_0+T_1)t}{T_0T_1}\right)} \tag{6.8}$$

The observation angle, θ, can be solved from the dot product of $\vec{r}_0$ and $\vec{R}$.

$$\theta = \cos^{-1}\left[\frac{\vec{r}_0 \cdot \vec{R}}{|\vec{r}_0||\vec{R}|}\right] \tag{6.9}$$

$$\theta = \cos^{-1}\left[\frac{r_0r_1\cos\left(\frac{2\pi t}{T_0}\right)\cos\left(\frac{2\pi t}{T_1}\right) - r_0r_1\sin\left(\frac{2\pi t}{T_0}\right)\sin\left(\frac{2\pi t}{T_1}\right) - r_0^2}{r_0\sqrt{r_0^2 + r_1^2 - 2r_0r_1\cos\left(\frac{2\pi(T_0+T_1)t}{T_0T_1}\right)}}\right] \tag{6.10}$$

$$\theta = \cos^{-1}\left[\frac{r_1\cos\left(\frac{2\pi(T_0+T_1)t}{T_0T_1}\right) - r_0}{\sqrt{r_0^2 + r_1^2 - 2r_0r_1\cos\left(\frac{2\pi(T_0+T_1)t}{T_0T_1}\right)}}\right] \tag{6.11}$$

Using this equation, I plotted the observation angle, θ in Figure 6.2 for ten seconds before and after conjunction (nearest pass) with an observer at an altitude of 575 km and target at 600 km.

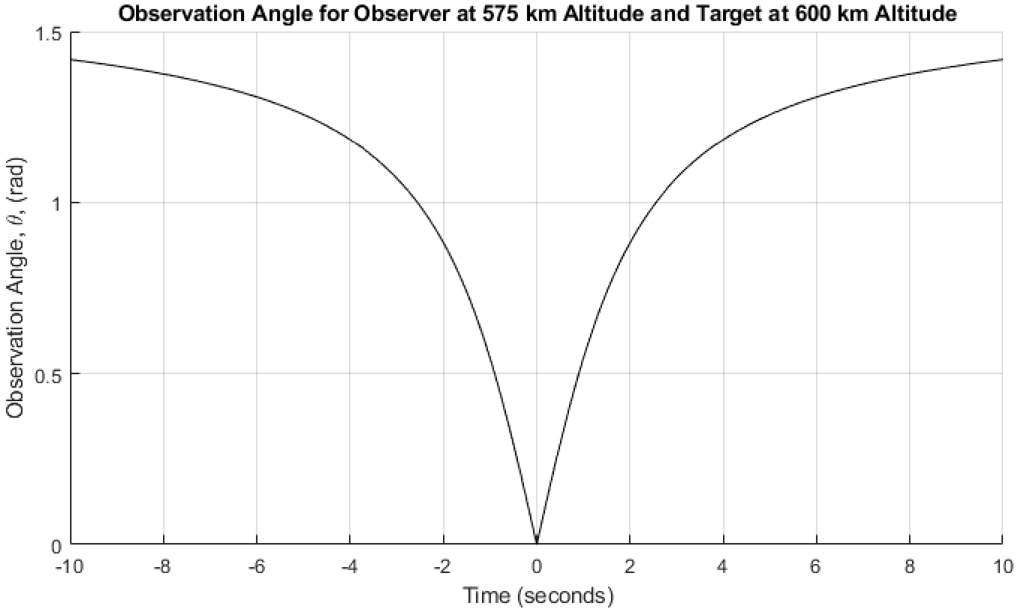

Figure 6.2. Observation angle (rad) for observer at 575 km and target at 600 km, closest pass between observer and target occurs at $t = 0$

Finally, taking the time derivative of observation angle will define the observation angular speed, $\dot{\theta}$. With $\gamma = \dfrac{2\pi(T_0 + T_1)}{T_0 T_1}$:

$$\dot{\theta} = \frac{d}{dt}\cos^{-1}\left[\frac{r_1 \cos\left(\dfrac{2\pi(T_0+T_1)t}{T_0T_1}\right) - r_0}{\sqrt{r_0^2 + r_1^2 - 2r_0r_1\cos\left(\dfrac{2\pi(T_0+T_1)t}{T_0T_1}\right)}}\right] \tag{6.12}$$

$$\dot{\theta} = -\frac{1}{\sqrt{1-\cos^2\theta}}\frac{d}{dt}\left[\frac{r_1\cos(\gamma t) - r_0}{\sqrt{r_0^2 + r_1^2 - 2r_0r_1\cos(\gamma t)}}\right] \tag{6.13}$$

$$\dot{\theta} = -\frac{1}{\sqrt{\sin^2\theta}}\frac{1}{r_0^2 + r_1^2 - 2r_0r_1\cos(\gamma t)}\left\{\frac{d}{dt}[r_1\cos(\gamma t) - r_0]\sqrt{r_0^2 + r_1^2 - 2r_0r_1\cos(\gamma t)} - \right.$$
$$\left.[r_1\cos(\gamma t) - r_0]\frac{d}{dt}\left[\sqrt{r_0^2 + r_1^2 - 2r_0r_1\cos(\gamma t)}\right]\right\} \tag{6.14}$$

$$\dot{\theta} = -\frac{1}{|\sin\theta|}\frac{1}{r_0^2 + r_1^2 - 2r_0r_1\cos(\gamma t)}\left\{-r_1\gamma\sin(\gamma t)\sqrt{r_0^2 + r_1^2 - 2r_0r_1\cos(\gamma t)} - \right.$$

$$\left.[r_1\cos(\gamma t) - r_0]\frac{\frac{d}{dt}[r_0^2 + r_1^2 - 2r_0r_1\cos(\gamma t)]}{2\sqrt{r_0^2 + r_1^2 - 2r_0r_1\cos(\gamma t)}}\right\} \tag{6.15}$$

$$\dot{\theta} = -\frac{1}{|\sin\theta|}\frac{1}{r_0^2 + r_1^2 - 2r_0r_1\cos(\gamma t)}\left\{-r_1\gamma\sin(\gamma t)\sqrt{r_0^2 + r_1^2 - 2r_0r_1\cos(\gamma t)} - \right.$$

$$\left.\frac{[r_1\cos(\gamma t) - r_0]r_0r_1\gamma\sin(\gamma t)}{\sqrt{r_0^2 + r_1^2 - 2r_0r_1\cos(\gamma t)}}\right\} \tag{6.16}$$

$$\dot{\theta} = -\frac{1}{|\sin\theta|}\frac{-r_1\gamma\sin(\gamma t)\sqrt{r_0^2 + r_1^2 - 2r_0r_1\cos(\gamma t)} - \cos\theta r_0r_1\gamma\sin(\gamma t)}{r_0^2 + r_1^2 - 2r_0r_1\cos(\gamma t)} \tag{6.17}$$

$$\dot{\theta} = \frac{\sqrt{r_0^2 + r_1^2 - 2r_0r_1\cos(\gamma t)} + \cos\theta r_0}{|\sin\theta|}\frac{r_1\gamma\sin(\gamma t)}{r_0^2 + r_1^2 - 2r_0r_1\cos(\gamma t)} \tag{6.18}$$

$$\dot{\theta} = \frac{r_1\cos(\gamma t) - r_0 + \cos^2\theta r_0}{\cos\theta|\sin\theta|}\frac{r_1\gamma\sin(\gamma t)}{r_0^2 + r_1^2 - 2r_0r_1\cos(\gamma t)} \tag{6.19}$$

$$\dot{\theta} = \frac{r_1\cos(\gamma t) - r_0\sin^2\theta}{\cos\theta|\sin\theta|}\frac{r_1\gamma\sin(\gamma t)}{r_0^2 + r_1^2 - 2r_0r_1\cos(\gamma t)} \tag{6.20}$$

The maximum angular speed occurs at the moment of conjunction ($t = 0$). A discontinuity exists at $t = 0$. To resolve this, I took the maximum angular speed as the limit of this function at $t = 0^+$.

$$\dot{\theta}_{max} = \lim_{t\to 0^+}\dot{\theta} \tag{6.21}$$

$$\dot{\theta}_{max} = \lim_{t\to 0^+}\left[\frac{r_1\cos(\gamma t) - r_0\sin^2\theta}{\cos\theta|\sin\theta|}\frac{r_1\gamma\sin(\gamma t)}{r_0^2 + r_1^2 - 2r_0r_1\cos(\gamma t)}\right] \tag{6.22}$$

$$\dot{\theta}_{max} = \frac{r_1^2\gamma}{r_0^2 + r_1^2 - 2r_0r_1}\lim_{t\to 0^+}\left[\frac{\sin(\gamma t)}{|\sin\theta|}\right] \tag{6.23}$$

Unfortunately, the limit converges in the numerator and denominator to zero, therefore I applied L'Hopital's rule. Also note that since I am only looking at the right side of $t = 0$, then I can treat $|\sin\theta|$ as $\sin\theta$.

$$\dot{\theta}_{max} = \frac{r_1^2\gamma}{r_0^2 + r_1^2 - 2r_0r_1} \lim_{t\to 0^+} \left[\frac{\dfrac{d}{dt}\sin(\gamma t)}{\dfrac{d}{dt}\sin\theta}\right] \tag{6.24}$$

$$\dot{\theta}_{max} = \frac{r_1^2\gamma}{(r_0 - r_1)^2} \lim_{t\to 0^+} \left[\frac{\gamma\cos(\gamma t)}{\dot{\theta}\cos\theta}\right] \tag{6.25}$$

$$\dot{\theta}_{max} = \frac{r_1^2\gamma}{(r_0 - r_1)^2}\frac{\gamma}{\dot{\theta}_{max}} \tag{6.26}$$

$$\dot{\theta}_{max}^2 = \frac{r_1^2\gamma^2}{(r_1 - r_0)^2} \tag{6.27}$$

$$\dot{\theta}_{max} = \pm\frac{r_1\gamma}{r_1 - r_0} \tag{6.28}$$

The positive solution is correct, considering that the observation angle θ should increase after the observer and target pass by each other.

$$\dot{\theta}_{max} = \frac{r_1\gamma}{r_1 - r_0} \tag{6.29}$$

$$\dot{\theta}_{max} = \frac{r_1}{r_1 - r_0}\frac{2\pi(T_0 + T_1)}{T_0T_1} \tag{6.30}$$

$$\dot{\theta}_{max} = \frac{r_1}{r_1 - r_0}\frac{4\pi^2\left(\sqrt{\dfrac{r_0^3}{\mu}} + \sqrt{\dfrac{r_1^3}{\mu}}\right)}{4\pi^2\sqrt{\dfrac{r_0^3r_1^3}{\mu^2}}} \tag{6.31}$$

$$\dot{\theta}_{max} = \sqrt{\mu}\frac{\sqrt{r_0^3} + \sqrt{r_1^3}}{(r_1 - r_0)\sqrt{r_0^3r_1}} \tag{6.32}$$

By knowing the observer and target orbits, Equation 6.32 can therefore be used to estimate the required steering speed for tracking that target. For instance an observer at an altitude of 575 km tracking a target at an altitude of 600 km will require a steering speed of 0.606 rad/s at the moment of conjunction. Figure 6.3 plots Equation 6.20 for the case of an observer at an altitude of 575 km and a target at an altitude of 600 km.

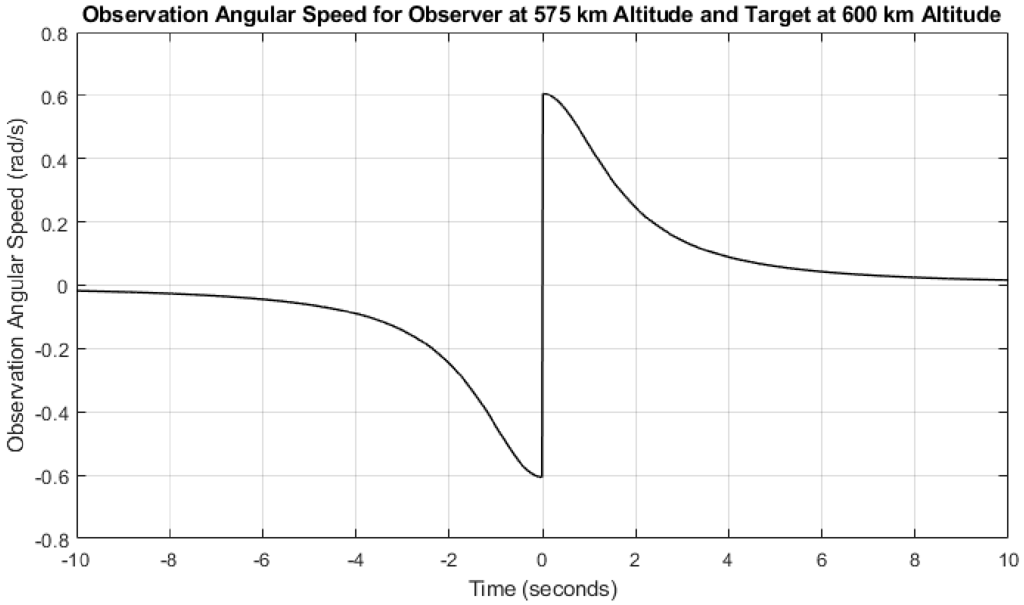

Figure 6.3. Observation angular speed (rad/s) for observer at 575 km and target at 600 km, closest pass between observer and target occurs at $t = 0$

The specifications for the Optotune MR-15-30 fast steering mirror used in the prototype can be found in Table 5 of Chapter 5. This mirror has a mechanical large angle step (20°) settling time of 13 ms. The optical angle (the angle the beam is steered through) is twice the mechanical angle, or 40°. I estimated the steering speed of the Optotune MR-15-30 by Equation 6.33 as approximately 53.7 rad/s.

$$\omega \approx \frac{\text{Optical Large Angle Step}}{\text{Settling Time}} \tag{6.33}$$

$$\omega \approx \frac{40\pi/180}{0.013} \tag{6.34}$$

$$\omega \approx 53.7 \text{ rad/s} \tag{6.35}$$

I now define the relationship between maximum detection range and FOR. I define angle β as the FOR half-angle, as illustrated in Figure 6.4. For these calculations I am also assuming the observer is always looking in the zenith direction, that is, away from Earth along the observers radial vector.

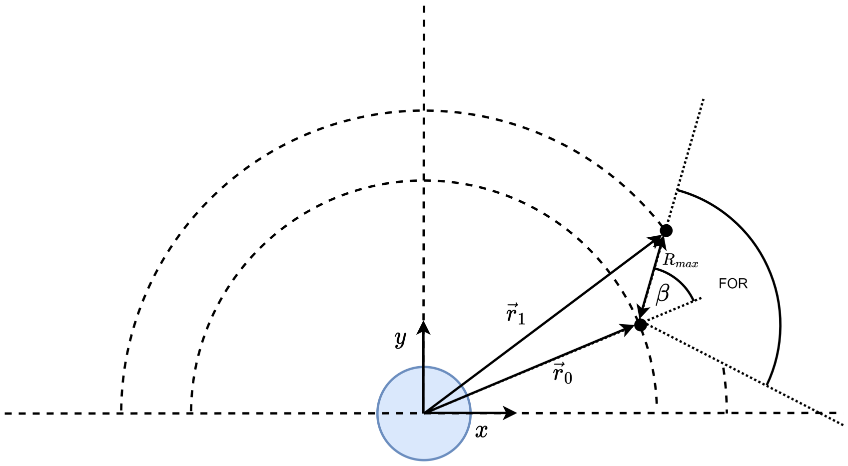

Figure 6.4. Orbital geometry of observer ($\vec{r}_0$) and target ($\vec{r}_1$) at the edge of the FOR. FOR half angle, β, is defined from the radial viewing axis (zenith) of the observing satellite. Relating to the geometry presented in Figure 6.1: R_{max} is the magnitude of the vector $\vec{R}$ when $\theta = \beta$.

I used Equation 6.11 to define when the target reaches the edge of the observer FOR, given by Equation 6.36.

$$\cos\beta = \frac{r_1\cos(\gamma t) - r_0}{\sqrt{r_0^2 + r_1^2 - 2r_0r_1\cos(\gamma t)}} \tag{6.36}$$

I solve for $\cos(\gamma t)$ explicitly in order to calculate $|\vec{R}|$; this indicates the distance between observer and target when the target is at the border of the observer's FOR. Consequently, this distance is the maximum possible between observer and target while the target still occupies the observers FOR.

$$\cos\beta\sqrt{r_0^2 + r_1^2 - 2r_0r_1\cos(\gamma t)} = r_1\cos(\gamma t) - r_0 \tag{6.37}$$

$$\cos^2\beta[r_0^2 + r_1^2 - 2r_0r_1\cos(\gamma t)] = [r_1\cos(\gamma t) - r_0]^2 \tag{6.38}$$

$$[r_0^2 + r_1^2 - 2r_0r_1\cos(\gamma t)]\cos^2\beta = r_1^2\cos^2(\gamma t) - 2r_0r_1\cos(\gamma t) + r_0^2 \tag{6.39}$$

This is quadratic, so:

$$0 = r_1^2\cos^2(\gamma t) + 2r_0r_1(\cos^2\beta - 1)\cos(\gamma t) + r_0^2(1 - \cos^2\beta) - r_1^2\cos^2\beta \tag{6.40}$$

$$0 = r_1^2\cos^2(\gamma t) - 2r_0r_1\sin^2\beta\cos(\gamma t) + r_0^2\sin^2\beta - r_1^2\cos^2\beta \tag{6.41}$$

Applying the quadratic equation:

$$\cos(\gamma t) = \frac{2r_0 r_1 \sin^2\beta \pm \sqrt{4r_0^2 r_1^2 \sin^4\beta - 4r_1^2(r_0^2\sin^2\beta - r_1^2\cos^2\beta)}}{2r_1^2} \tag{6.42}$$

$$\cos\left(\frac{2\pi(T_0+T_1)t}{T_0T_1}\right) = \frac{r_0\sin^2\beta \pm \sqrt{r_0^2\sin^4\beta + r_1^2\cos^2\beta - r_0^2\sin^2\beta}}{r_1} \tag{6.43}$$

$$\cos\left(\frac{2\pi(T_0+T_1)t}{T_0T_1}\right) = \frac{r_0\sin^2\beta \pm \sqrt{r_0^2\sin^2\beta(\sin^2\beta - 1) + r_1^2\cos^2\beta}}{r_1} \tag{6.44}$$

$$\cos\left(\frac{2\pi(T_0+T_1)t}{T_0T_1}\right) = \frac{r_0\sin^2\beta \pm \sqrt{-r_0^2\sin^2\beta\cos^2\beta + r_1^2\cos^2\beta}}{r_1} \tag{6.45}$$

$$\cos\left(\frac{2\pi(T_0+T_1)t}{T_0T_1}\right) = \frac{r_0\sin^2\beta \pm |\cos\beta|\sqrt{r_1^2 - r_0^2\sin^2\beta}}{r_1} \tag{6.46}$$

The correct solution is the positive one, since the solution must satisfy the condition that $\beta = 0$ when $t = 0$, corresponding to the time of nearest pass (conjunction). Then the maximum possible range based on the FOR can be found from Equation 6.8:

$$R_{max} = \sqrt{r_0^2 + r_1^2 - 2r_0\left(r_0\sin^2\beta + |\cos\beta|\sqrt{r_1^2 - r_0^2\sin^2\beta}\right)} \tag{6.47}$$

Equation 6.47 provides the trade-off between maximum detection range and FOR. This function is plotted in Figure 6.5 for the case where an observer has an altitude of 575 km and a target has an altitude of 600 km.

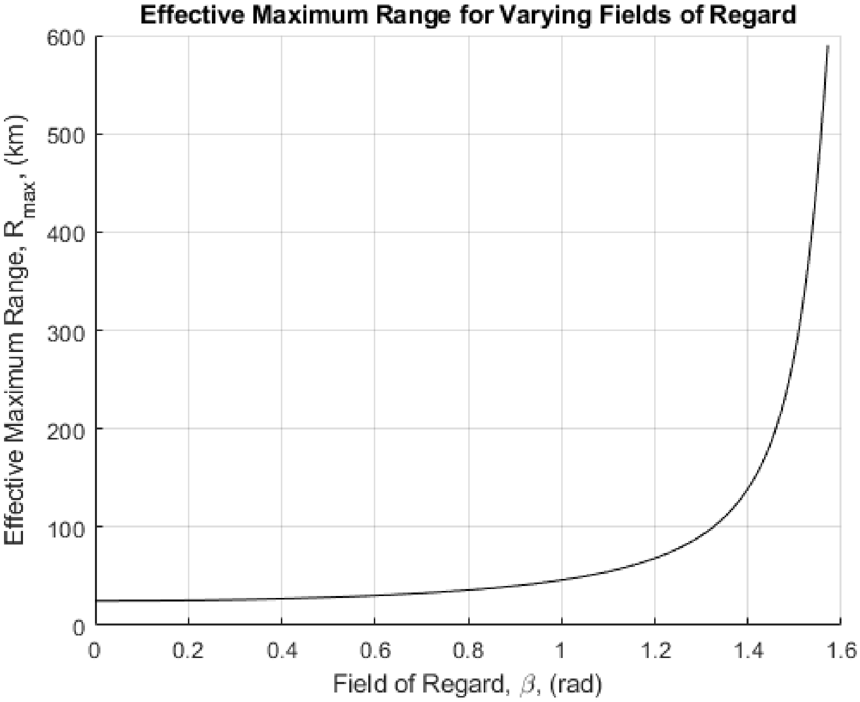

Figure 6.5. Maximum effective range vs effective field of regard for an observer at 575 km altitude and a target at 600 km

I will illustrate the importance of this trade-off with an example. Consider an observer orbit of 575 km altitude, a maximum detection range of 5 km, and a FOR half angle of 50°. Then the target altitude should be 578.2 km to have the maximum detection range occur at the edge of the FOR. If the target altitude was higher than 578.2 km, then the target would drift out of the maximum detection range before reaching the edge of the FOR, as such, this additional FOR is effectively useless, and reducing the observer FOR would have no adverse effect on performance. Likewise, if the target altitude was below 578.2, then when the target is within the FOR, the target would be capable of being ranged by the observer, and a larger FOR would increase the effective observation time window. With this in mind, one could use the observer orbit, worst-case target orbit of interest, and observer range capability to determine a FOR requirement. The process of selecting one requirement over another is highly mission dependent. Most likely a mission would first define observer orbit, r_0, and target orbits, r_1, and then either range capability, R_{max}, or observer FOR, β, would be determined based on laser rangefinder or steering optics specifications respectively.

I also investigated the overall system scanning rate, f, and how it relates to both mirror steering speed, ω, and maximum range capability, R_{max}. The overall system scanning rate is particularly important for target acquisition; more measurements in the same search window increases the chance of a target being acquired. The overall system scanning rate depends on the sum of time it takes to steer the mirror, t_{steer}, and the time it takes to take a laser ranging measurement, $t_{measure}$.

$$f = \frac{1}{t_{steer} + t_{measure}} \tag{6.48}$$

The time it takes to steer the mirror depends on the angular steering distance, $\Delta\theta$, and the mirror steering speed, ω.

$$t_{steer} = \frac{\Delta\theta}{\omega} \tag{6.49}$$

The amount of time taken to measure is proportional to the maximum range capability, R_{max}. This relationship arises from the radar equation for lasers [55] applied to a diffuse target, presented later in this chapter, in Equation 6.101. I present Equation 6.101 here as well under Equation 6.50 to derive the relationship between measurement time and maximum range:

$$R_{max} = \left[\rho_M^2 \rho \frac{A_M A_r r^2}{A_T \pi \alpha^2} \left(\frac{P_T}{P_R}\right)\right]^{1/4} \tag{6.50}$$

where R_{max} is the range capability of the overall laser system, ρ_M is the reflectivity of the steering mirror, ρ is the reflectivity of the target object, A_M is the effective mirror area, A_r is the effective laser rangefinder receiver area, A_T is the laser emitter area, α is the laser beam divergence half angle, r is the target nominal radius, and $\left(\frac{P_T}{P_R}\right)$ is the transmit to received power ratio. Because they are either defined by static geometry, or are a constant material property, all terms except for the transmit to received power ratio, $\frac{P_T}{P_R}$ and the range capability, R_{max} are constant. Therefore the transmit to received power ratio is proportional to the quartic of the range capability:

$$\frac{P_T}{P_R} \propto R_{max}^4 \tag{6.51}$$

The signal-to-noise ratio (SNR) is defined as:

$$SNR = \frac{\text{signal power}}{\text{noise power}} \tag{6.52}$$

The signal is the received power, P_R, and I assume noise as constant with respect to signal strength. I define the minimum measurement cut-off SNR as SNR_0. If any returned signal had an SNR below this value the measurement would not occur, thus SNR_0 is the SNR related to the range capability, R_{max}. This cut-off SNR is constant for the given laser ranging system.

$$P_R \propto SNR_0 \tag{6.53}$$

The laser rangefinder sends several laser pulses, N pulses, with a set pulse rate, f_{pulse}, and measures the accumulation of returning photons from these pulses over a given measurement window, t_{meas} to achieve a sufficient signal to noise ratio. This relationship is:

$$t_{meas} = \frac{N}{f_{pulse}} \tag{6.54}$$

These pulses have the same energy, dependent on the amount of photons emitted. The overall energy of all these photons over all pulses gives the emitted power, P_T. Therefore P_T is proportional to the amount of pulses:

$$P_T \propto N \tag{6.55}$$

Then from Equations 6.51-6.55, I can derive the following:

$$\frac{P_T}{P_R} \propto R_{max}^4 \tag{6.56}$$

$$\frac{N}{SNR_0} \propto R_{max}^4 \tag{6.57}$$

$$N \propto R_{max}^4 \tag{6.58}$$

$$t_{meas} f_{pulse} \propto R_{max}^4 \tag{6.59}$$

Therefore, since f_{pulse} is constant, the measurement time is proportional to the quartic of range capability:

$$t_{measure} \propto R_{max}^4 \tag{6.60}$$

This relationship is validated by plotting the measurement time against range capability provided by the specifications for the DLEM laser rangefinder [63] in Figure 6.6.

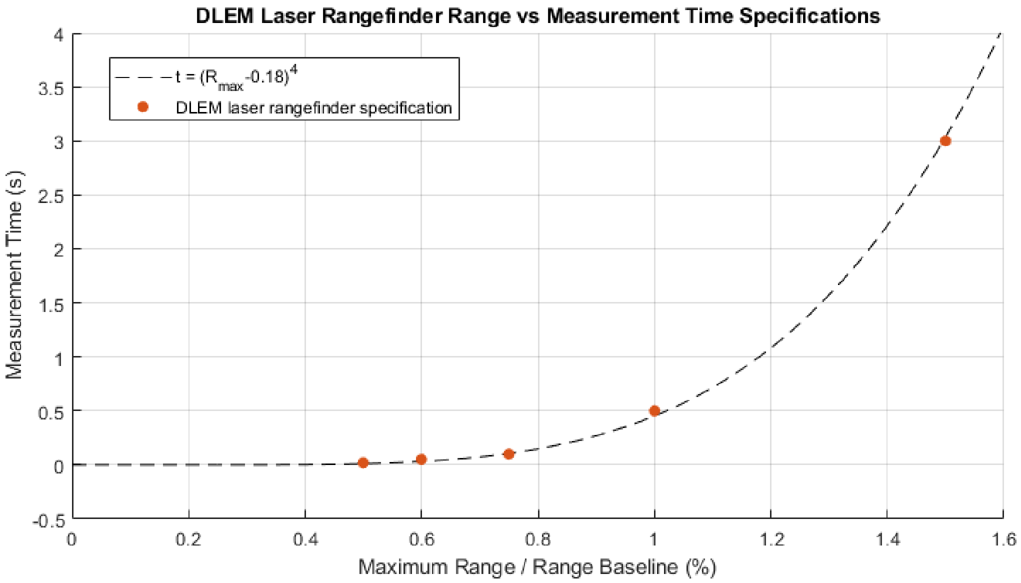

Figure 6.6. DLEM laser rangefinder range vs measurement time specification plotted against proposed quartic range model

Finally, the relationship between overall system scanning rate, mirror steering speed, and maximum range capability is:

$$f = \frac{1}{\dfrac{\Delta\theta}{\omega} + kR_{max}^4} \tag{6.61}$$

where k is a proportionality constant representing the photon detection capability of the laser rangefinder. As a result, to increase overall scanning rate either the system steering speed or photon detection capability of the laser rangefinder must be increased.

Finally, I assessed the uncertainty associated with a single laser ranging measurement caused by beam divergence, steering mirror angular resolution, and steering mirror 1-sigma angular repeatability. I modeled this uncertainty as a probability distribution of the true position of the target. Specifically, I assumed the true target position is uniformly distributed over a circular region of radius ρ. The variance in one axis for a uniform distribution isolated to a circle of radius ρ is given by Equation 6.66.

$$\sigma_x^2 = \frac{\iint_A x^2 dA}{A} \tag{6.62}$$

$$\sigma_x^2 = \frac{\iint_A (r\cos\theta)^2 r dr d\theta}{\pi\rho^2} \tag{6.63}$$

$$\sigma_x^2 = \frac{\int_0^{2\pi}\int_0^{\rho} r^3 \cos^2\theta dr d\theta}{\pi\rho^2} \tag{6.64}$$

$$\sigma_x^2 = \frac{\rho^4 \int_0^{2\pi} \cos^2\theta d\theta}{4\pi\rho^2} \tag{6.65}$$

$$\sigma_x^2 = \frac{\rho^2}{4} \tag{6.66}$$

The same result occurs for σ_y. I then defined the radius for this uniform distribution as the distance defined by beam divergence, α, steering mirror resolution, ν, steering mirror repeatability, κ, and target to observer range, R. I assumed each of the angular effects, α, ν, and κ, are independent. I combined the angular effects using root sum square to obtain an equivalent angular error. Then, this equivalent angular error was multiplied by the observer range, giving the total measurement error radius, as in Equation 6.67.

$$\rho = R\sqrt{\alpha^2 + \nu^2 + \kappa^2} \tag{6.67}$$

Then using Equation 6.66:

$$\sigma_x^2 = \sigma_y^2 = \frac{R^2(\alpha^2 + \nu^2 + \kappa^2)}{4} \tag{6.68}$$

Finally, the entire covariance matrix, Σ, can be described by Equation 6.69, with the z-axis of the covariance matrix presented is in the direction of the beam. The variance along this z-axis is defined by the laser range accuracy specification, σ_z.

$$\Sigma = \begin{bmatrix} \frac{R^2(\alpha^2 + \nu^2 + \kappa^2)}{4} & 0 & 0 \\ 0 & \frac{R^2(\alpha^2 + \nu^2 + \kappa^2)}{4} & 0 \\ 0 & 0 & \sigma_z^2 \end{bmatrix} \tag{6.69}$$

6.2 Maximum Detectable Range Analysis

This section details the process and analysis of a determining the maximum detectable range of a laser rangefinder theoretically. Two different target surface properties are analyzed: a diffuse reflecting target and a retro-reflective target.

6.2.1 Laser Rangefinder Ranging Capability Factors

Time of flight sensors emit particles (or waves) of a known, constant speed and measure the time it takes for the particle (or wave) to make a round trip from a target back to the sensor. Sensors that emit electromagnetic radiation have the capability to predict the behaviour of these particles, given the speed of light in a vacuum is fixed. For instance, laser range-finders and radar both use electromagnetic radiation to determine relative positions of objects in their vicinity. Combining time-of-flight measurements with sensor pointing information provides a complete three-dimensional measurement of a target's location.

Laser rangefinders determine the distance to a target by measuring the time of flight between the emission and return of photons. Time of flight measurements are based on the relationship between distance, speed, and time, given in Equation 6.70.

$$d = \frac{c\Delta t}{2} \tag{6.70}$$

where d is the distance between observer and target, c is the speed of light in the relevant medium the light is passing though, and Δt is the time it takes between signal emission and return. Although laser rangefinders are very effective in measuring the range between an observer, there are some potential issues limiting the range of laser range-finders for space-based tracking:

1. Dispersion of light intensity due to beam divergence

2. Changes in photon speed due to medium

3. Target surface reflectivity
4. Inaccuracy due to averaging between measurements of a moving object
5. Velocity aberration

The following subsections describe in more detail the individual effect of the above factors and whether they must be accounted for in a space-based tracking situation. Following this section, a more in-depth mathematical analysis of the non-negligible factors is given.

6.2.1.1 Beam Divergence

Due to light diffraction, a laser beam will increase in diameter as it propagates through space. This effect is called beam divergence, in this thesis the divergence half-angle, α, is used to describe beam divergence. Figure 6.7 illustrates the geometry of this effect.

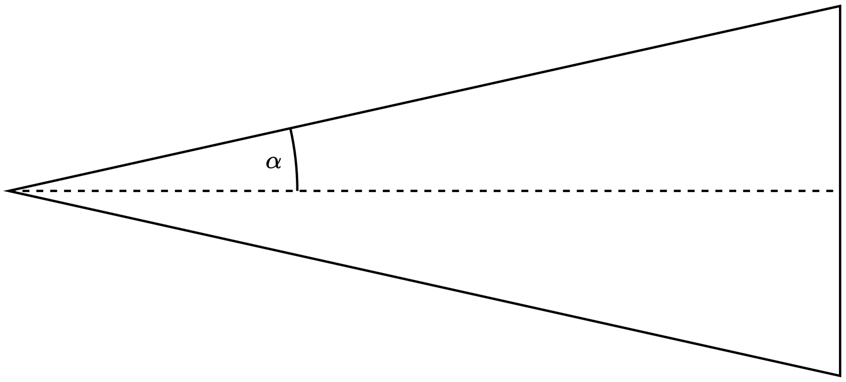

Figure 6.7. Illustation of beam divergence propagation, beam travels left to right

Since beam divergence disperses energy from an emitted beam, the divergence half-angle has a significant effect on the maximum detectable range. That is, all else being equal, a larger beam divergence results in a lower maximum achievable range for a laser rangefinder. This effect is explored in Section 6.2.2.

6.2.1.2 Speed of Light in a Medium

The speed of light in vacuum is 299,792,458 m/s [76], however the speed of light in a medium is slower. For instance in the atmosphere at sea level the speed of light is 299,704,675 m/s [77]. This effect has implications for the accurate function of a rangefinder as the speed used in equation 6.70 must reflect the speed of light given the medium it is traveling in. For instance, a rangefinder in space that is tuned to use the speed of light in the atmosphere will read a distance that is 99.97% the actual range. Overall, this error is negligible for a space-based platform as the emitted and received beam remain solely in vacuum, therefore this error is easily corrected by proper rangefinder calibration prior to mission implementation.

The effect that a medium has on the speed of light also has implications for the signal to noise ratio. Attenuation occurs due to molecules absorbing specific wavelengths of light, or molecules otherwise scattering light, causing beam dispersion. This effect is negligible in low Earth orbit due to the relative lack of atmospheric gases at this altitude. As such for a space-based platform ranging space-based targets, the effect of atmospheric attenuation is negligible.

6.2.1.3 Target Surface Reflectivity

Light emitted from the laser rangefinder must reflect off the target and return to achieve a successful measurement. The way that light reflects off the target is determined by its surface properties. In this thesis I explored two broad categories of surface reflectivity: diffuse and retro-reflective. Diffuse surfaces disperse the returned laser beam while retro-reflectors maintain the laser beam's focus. Therefore diffuse targets are far more range-limited compared to retro-reflective targets. The effect of surface reflectivity is explored in Section 6.2.2.

6.2.1.4 Moving Target Range Inaccuracy

For a laser rangefinder to make an accurate measurement, enough emitted photons must be returned to the rangefinder receiver to overcome typical environmental noise. Therefore the Signal-to-Noise Ratio (SNR) is the key parameter that determines whether a measurement is successful or not. The SNR can be increased by averaging the measurements from several pulses over a specified time window, at the expense of system responsiveness. Relative motion along the axis of a laser range-finder beam causes inaccuracy due to this pulse averaging. Because this method averages the return over multiple beams, the measured range is the average range of the object over the entire measurement time. This effect is documented for the JENOPTIK DLEM 20 laser rangefinder to reduce the maximum detectable range of the rangefinder by up to 10% [63], depending on the target speed. Additionally, this effect impacts the accuracy of ranging measurements. This impact on accuracy can be approximated by taking the average of the target range from the first pulse, R_1, and last pulse, R_2, of the measurement window [63], given in Equation 6.71.

$$R_{measurement} = \frac{R_1 + R_2}{2} \tag{6.71}$$

By simulating two satellites traveling in the same orbital plane but in opposite directions an upper limit of this error can be determined. For instance, considering an observer occupying an altitude of 575 km and a target occupying an altitude of 600 km causes the theoretical ranging errors given in Figure 6.8.

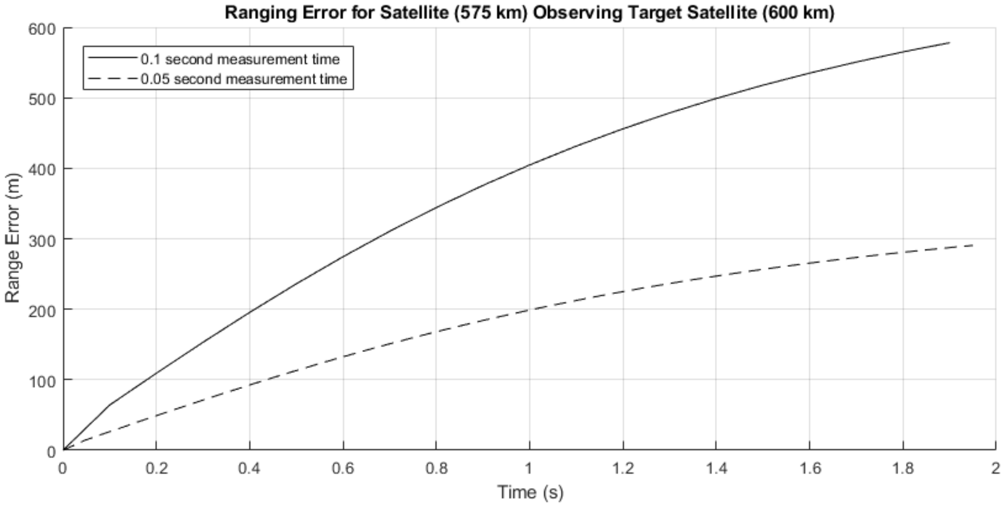

Figure 6.8. Ranging error for an observer with measurement time of 0.05 seconds and 0.1 seconds, occupying an altitude of 575 km. Measured target occupies an orbital altitude of 600 km and travels in the opposite direction of the observer. Time $t = 0$ is the moment of closest approach between the two satellites.

In the case of a 0.05 second measurement window the ranging error remains below 280 metres between the time of conjunction and the time the target falls outside the observer field of regard (around 2 seconds). A lower measurement time reduces the amount of distance the target will travel between the start and end of the pulses, therefore reducing the error caused by relative motion. This error also depends on the relative geometry and dynamics of observer and target. For instance, if the observer and target travel in the same direction, this error is expected to be comparatively small since the relative velocities between both satellites is also comparatively small. This error should also decrease as the distance between observer and target orbital altitudes increases.

6.2.1.5 Velocity aberration

Velocity aberration describes the effect that relative tangential motion has on the trajectory of a ray of light from a target far away. This effect is important for astronomical measurements but also for ensuring that returned light from a target lands on the receiver. This effect is really only relevant when ranging targets with retro-reflective surfaces when the beam remains focused during return. Velocity aberration causes an angular offset, δ, of the returning beam according to Equation 6.88.

$$\tan(\theta') = \frac{\sin\theta}{v_{rel}/c + \cos\theta} \tag{6.72}$$

where v_{rel} is the relative velocity between observer and target and c is the speed of light, as long as the relative speed is relatively small compared to the speed of light. Equation 6.88 results from the stellar aberration equation [27], Equation 6.72. Where θ' is the angle a laser rangefinder is pointing relative to the velocity vector and θ is the angle that the laser beam returns from the target.

The angular offset, δ is the difference between the angle the laser rangefinder is pointed, θ', and the angle the laser beam returns, θ.

$$\delta = \theta - \theta' \tag{6.73}$$

$$\delta = \theta - \tan^{-1}\left(\frac{\sin\theta}{v_{rel}/c + \cos\theta}\right) \tag{6.74}$$

The maximum of this function (and therefore the worst case aberration) with respect to

θ can be determined by calculating the derivative:

$$\frac{d\delta}{d\theta} = \frac{d}{d\theta}\left[\theta - \tan^{-1}\left(\frac{\sin\theta}{v_{rel}/c + \cos\theta}\right)\right] \tag{6.75}$$

$$\frac{d\delta}{d\theta} = 1 - \frac{1}{1 + \left(\frac{\sin\theta}{v_{rel}/c + \cos\theta}\right)^2}\frac{d}{d\theta}\left(\frac{\sin\theta}{v_{rel}/c + \cos\theta}\right) \tag{6.76}$$

$$\frac{d\delta}{d\theta} = 1 - \frac{(v_{rel}/c + \cos\theta)^2}{(v_{rel}/c + \cos\theta)^2 + \sin^2\theta}\frac{\cos\theta(v_{rel}/c + \cos\theta) + \sin^2\theta}{(v_{rel}/c + \cos\theta)^2} \tag{6.77}$$

$$\frac{d\delta}{d\theta} = 1 - \frac{\cos\theta(v_{rel}/c + \cos\theta) + \sin^2\theta}{(v_{rel}/c + \cos\theta)^2 + \sin^2\theta} \tag{6.78}$$

$$\frac{d\delta}{d\theta} = 1 - \frac{\cos^2\theta + v_{rel}/c\cos\theta + \sin^2\theta}{(v_{rel}/c)^2 + 2v_{rel}/c\cos\theta + \cos^2\theta + \sin^2\theta} \tag{6.79}$$

$$\frac{d\delta}{d\theta} = 1 - \frac{1 + v_{rel}/c\cos\theta}{(v_{rel}/c)^2 + 2v_{rel}/c\cos\theta + 1} \tag{6.80}$$

$$\frac{d\delta}{d\theta} = \frac{(v_{rel}/c)^2 + v_{rel}/c\cos\theta}{(v_{rel}/c)^2 + 2v_{rel}/c\cos\theta + 1} \tag{6.81}$$

This derivative never reaches zero between $[0, \pi/2]$, therefore the maximum occurs at either 0 or $\pi/2$. The angular offset is always larger for $\theta = \pi/2$, so then the maximum angular offset is:

$$\delta_{max} = \frac{\pi}{2} - \tan^{-1}\left(\frac{1}{v_{rel}/c}\right) \tag{6.82}$$

$$\frac{\pi}{2} - \delta_{max} = \tan^{-1}\left(\frac{1}{v_{rel}/c}\right) \tag{6.83}$$

$$\tan(\frac{\pi}{2} - \delta_{max}) = \frac{1}{v_{rel}/c} \tag{6.84}$$

$$\cot(\delta_{max}) = \frac{1}{v_{rel}/c} \tag{6.85}$$

$$\tan(\delta_{max}) = \frac{v_{rel}}{c} \tag{6.86}$$

$$\delta_{max} = \tan^{-1}\left(\frac{v_{rel}}{c}\right) \tag{6.87}$$

For the case that $v_{rel} << c$ the small angle approximation holds, resulting in Equation 6.88.

$$\delta_{max} \approx \frac{v_{rel}}{c} \tag{6.88}$$

In order to capture the returned beam from a retroreflector the beam must widen at least as much as this angular offset. In other words, the divergence half-angle of the beam must be equal to or larger than this offset. For the case of an observer occupying an altitude of 575 km and a target occupying an altitude of 600 km, traveling in the opposite direction, this offset is calculated to be at most $\theta = 0.05$ mrad. The laser rangefinder investigated in this thesis has a divergence half-angle of $\alpha = 0.4$ mrad so this effect was not considered further. However, it should be considered if a system plans to implement a narrow beam. In such a case, the target retro-reflector may be designed to effectively widen the returning beam [28].

6.2.2 The Radar Equation

The radar equation describes the relationship between key parameters of an electromagnetic ranging sensor, such as the eponymous radar, or laser rangefinders. The radar equation is well established in literature for analyzing the capability of both ground and space-based laser systems ranging satellites [37], [51], [52], [53]. The radar equation encompasses the following parameters, most of which were described briefly in the above sections:

- Range
- Target reflectivity
- Transmitter power
- Antenna/Receiver aperture
- Losses such as attenuation

Most directly relevant to my work is the form of radar equation presented by Forrester and Hulme [55] on the application of a laser detecting a diffuse target, as provided in equation 6.89.

$$P_r = \frac{P_t A_r}{\pi R^2} \eta e^{-2kR} \tag{6.89}$$

where P_r is the received laser power, P_t is emitted laser power, A_r is the receiver aperture area, R is the distance between the laser emitter and target, η is the ratio of reflected to incident radiant flux at the target, and k is the atmospheric attenuation coefficient. To simplify my work I assume that atmospheric attenuation is negligible, as such I assumed $k = 0$. Incorporating this assumption results in the following:

$$P_r = \frac{P_t A_r}{\pi R^2}\eta \tag{6.90}$$

6.2.2.1 Diffuse Targets

Diffuse surfaces reflect light uniformly in all directions. A Lambertian surface is commonly used to model diffuse surfaces [37], [53], [55], [56]. Lambertian surfaces are defined by having a constant radiance, independent of observation angle. The irradiance of a Lambertian surface follows Lambert's cosine law:

$$I_{reflected} = I_{incident}\rho\cos\theta \tag{6.91}$$

where I is the light intensity in W/m^2, ρ is the reflectivity of the target, and θ is the angle of incidence. The factor η is defined as the ratio of the reflected, $\Phi_{reflected}$ to incident radiant flux, $\Phi_{incident}$. Radiant flux is equivalent to the product of irradiance and area. Therefore, when presented with a target smaller than the beam diameter I have to consider the areas of the target and the beam I have to consider the areas of the target, A, and the beam, $\pi\alpha^2 R^2$, resulting in Equation 6.95.

$$\eta = \frac{\Phi_{reflected}}{\Phi_{incident}} \tag{6.92}$$

$$\eta = \frac{I_{reflected}A_{reflected}}{I_{incident}A_{incident}} \tag{6.93}$$

$$\eta = \frac{I_{incident}\rho\cos\theta A_{reflected}}{I_{incident}A_{incident}} \tag{6.94}$$

$$\eta = \frac{\rho A\cos^2\theta}{\pi\alpha^2 R^2} \tag{6.95}$$

where A is the target area, α is the beam divergence half angle, and R is the distance between observer and target. I made the assumption that the target is always normal to the observer ($\theta = 0$), yielding an idealized scenario and therefore an upper bounds for η

and consequently, an upper bounds for maximum achievable range R, given by Equation 6.96.

$$\eta = \frac{\rho A}{\pi \alpha^2 R^2} \tag{6.96}$$

6.2.2.2 Retroreflective Targets

Retroreflective surfaces reflect light back in the direction of their source. Wojtanowski et al. provide a comprehensive derivation of the return for a corner cube retroreflector (see Figure 6.9), including experimental empirical characterization of the effect different angles of incidence have on the far field diffraction pattern [37]. Based on the results of Wojtanowski et al. [37] a corner cube retro-reflector target normal to the observer Equation 6.97 can be used for η.

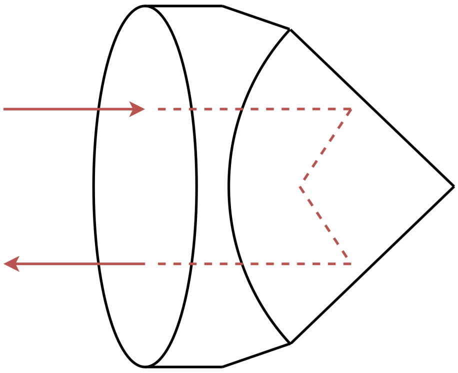

Figure 6.9. Illustration of corner cube retroreflector (re-drawn from Degnan [56]). The geometry of the corner cube retroreflector directs the reflected ray back along the same path as the incident ray.

$$\eta = 0.63 \frac{4 \rho A^2}{\alpha^2 \lambda^2 R^2} \tag{6.97}$$

where ρ is the reflectivity of the retroreflector, A is the area of corner cube retroreflector, α is the beam divergence half angle, R is the distance between observer and target, and λ is the laser wavelength.

6.2.3 Return Energy Model

The radar equation used to model the return from a laser rangefinder paired with a fast-steering mirror is given by Equations 6.98 and 6.99.

$$\frac{P_R}{P_T} = \rho_M^2 \frac{A_M}{A_T} \frac{A_r}{\pi R^2} \eta \tag{6.98}$$

$$\eta = \begin{cases} \dfrac{\rho r^2}{\alpha^2 R^2}, & \text{diffuse surface} \\ 0.63 \dfrac{4\rho \pi^2 r^4}{\alpha^2 \lambda^2 R^2}, & \text{retroreflective surface} \end{cases} \tag{6.99}$$

The effective mirror area, A_M, laser transmitter area, A_T, and mirror reflectance, ρ_M, have been included to account for the geometry of a steering mirror that is smaller than the laser emitter aperture. The effect of mirror geometry is explored in depth in Section 6.3. Note that the target area has been substituted with $A = \pi r^2$, assuming a target with a nominal radius of r. If the calculated energy ratio, $\frac{P_r}{P_t}$, for a measurement exceeds a threshold value, the measurement is considered valid. This threshold value is dependent on the laser rangefinder specifications. This model is used to estimate the laser tracking system's maximum range for targets with and without retroreflectors.

The threshold energy ratio, $\left(\frac{P_r}{P_t}\right)_0$ was determined by using the specifications for Jenoptik's DLEM line of laser rangefinders [63] alongside Equation 6.100.

$$\left(\frac{P_R}{P_T}\right)_0 = \frac{\rho A_r A}{\pi^2 \alpha^2 R_{max}^4} \tag{6.100}$$

Equation 6.100 is the radar equation for the case of a diffuse target. Relevant ranging specifications for each DLEM laser rangefinder model [63] and their associated energy ratio thresholds calculated using Equation 6.100 are tabulated in Table 6. A beam filling target is a target who's area encompasses the entire beam-width at the given range, in other words $A = \pi \alpha^2 R_{max}^2$.

Table 6. Jenoptik DLEM range specifications and energy ratios [63]

Model	A	A_r	ρ	R_{max}	$\left(\frac{P_R}{P_T}\right)_0$
	[m^2]	**[mm^2]**		**[m]**	
DLEM 20	Beam filling	314	0.5	4500	2.47×10^{-12}
DLEM 30	Beam filling	800	0.5	8000	1.99×10^{-12}
DLEM 45	Beam filling	1662	0.5	11000	2.19×10^{-12}

The lowest energy ratio threshold was found to be 1.99×10^{-12} for all DLEM models. Therefore, a value of 1.99×10^{-12} was taken as the threshold ratio for further analysis.

The maximum achievable range, R, for a diffuse reflecting target as a function of target size, r, can be found by solving for range in the diffuse case of Equation 6.98, resulting in Equation 6.101.

$$R_{max} = \left[\rho_M^2 \rho \frac{A_M A_r r^2}{A_T \pi \alpha^2} \left(\frac{P_T}{P_R}\right)_0\right]^{1/4} \tag{6.101}$$

However there is a limiting range for the diffuse case when the target becomes beam-filling ($r = \alpha R$). The following then holds:

$$R_{max} = \left[\rho_M^2 \rho \frac{A_M A_r}{A_T \pi} \left(\frac{P_T}{P_R}\right)_0\right]^{1/2} \tag{6.102}$$

Similarly, the maximum range for a retroreflective target can be found by solving for the positive real roots of R in the retroreflective case of Equation 6.98, resulting in Equation 6.103.

$$R_{max} = \left[0.63 \rho_M^2 \rho \frac{4\pi A_M A_r r^4}{A_T \alpha^2 \lambda^2} \left(\frac{P_T}{P_R}\right)_0\right]^{1/4} \tag{6.103}$$

6.3 Laser to Mirror Geometry Optimization

From qualitative analysis of Equations 6.102 and 6.103, it can be seen that the maximum detectable range can be increased by increasing receiver area A_r, target size r, the mirror area ratio $\frac{A_M}{A_T}$, or by decreasing beam divergence α or wavelength λ. Note that since beam divergence is proportional to wavelength, a decrease in wavelength should have an emphasized effect. Of these parameters, the easiest to adjust for a prototype is the mirror area ratio. The receiver area, A_r, in this case is also limited by the small size of the mirror, therefore it is defined as the intersecting area between the projected mirror area and receiver aperture. As such, it was of interest to model the geometry of the laser rangefinder and steering mirror in the prototype to determine the optimal positioning of both devices relative to each other. Figures 6.11 and 6.10 provide diagrams for the relevant geometries and dimensions of the DLEM 20 and Optotune MR-15-30 used for the following calculations.

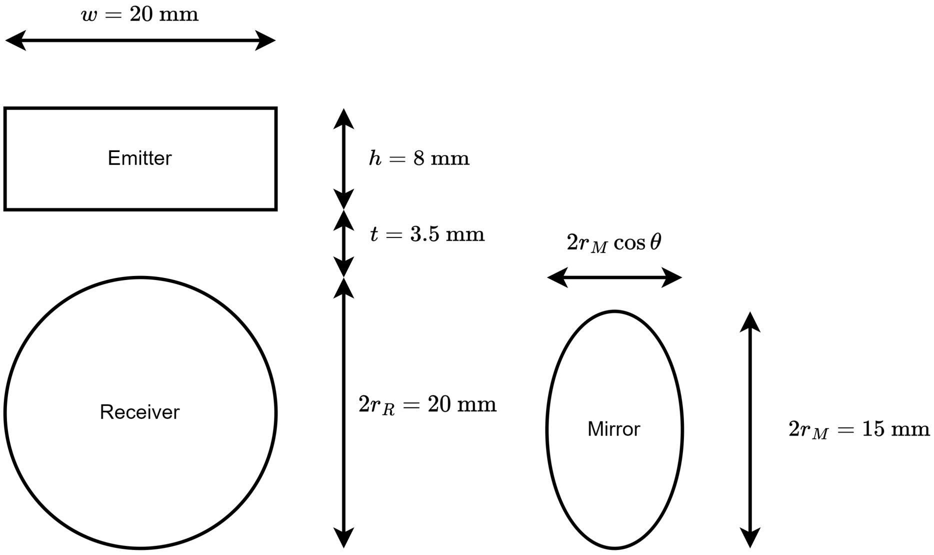

Figure 6.10. Laser rangefinder [63] (left) and tilted mirror projection [64] (right) dimensions. Where w and h are the laser emitter aperture width and height respectively, t is the offset between emitter and receiver apertures, r_R is the receiver aperture radius, and r_M is the FSM radius.

Based on the geometry of Figure 6.10, $A_r = 0$ when $d < t + h/2 - r_M$, and $A_M = 0$ when $d > t + h$. Therefore, meaningful values of η only occur for $t + h/2 - r_M \leq d \leq t + h$. I am trying to maximize the following parameter, which will be referred to as J to simplify notation:

$$J = A_r \frac{A_M}{A_T} \tag{6.104}$$

In the following subsections I define each area independently.

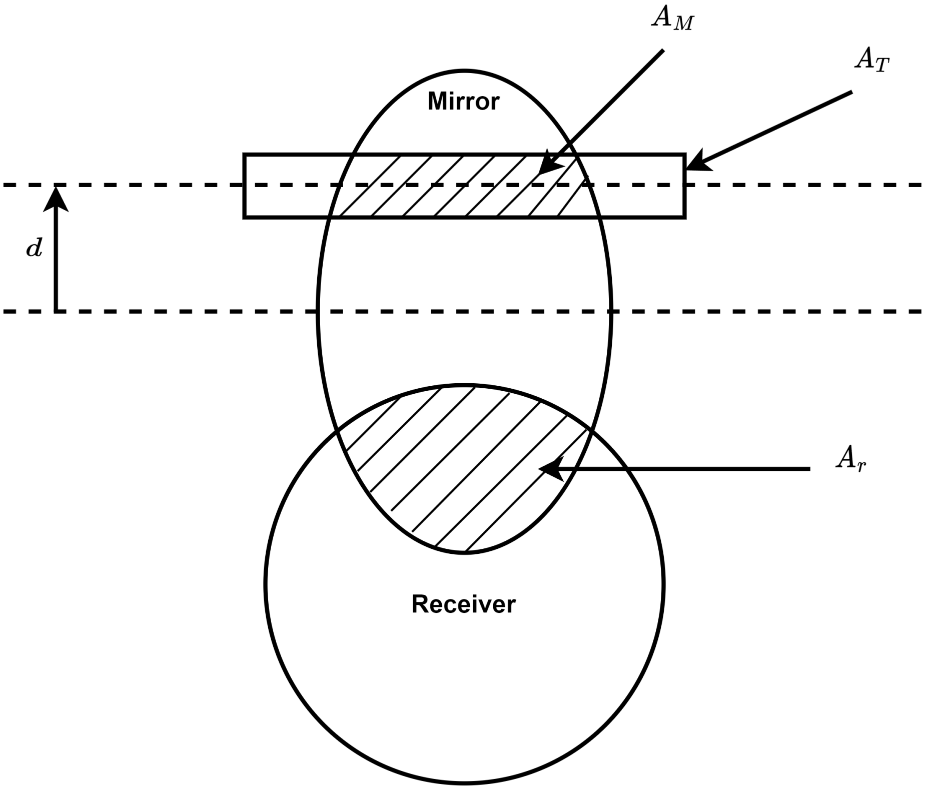

Figure 6.11. Geometric relationship between areas. Rectangle represents laser emitter area, the circular mirror is tilted and so the projection of this area appears elliptical. Shaded areas represent intersections of interest. Datum d is measured from the centreline of the mirror to the centreline of the emitter.

6.3.1 Transmitter Area A_T

I calculated this area directly from the laser rangefinder specifications.

$$A_T = hw \tag{6.105}$$

$$A_T = 8(20) \tag{6.106}$$

$$= 160\ \text{mm}^2 \tag{6.107}$$

6.3.2 Mirror Area A_M

Geometrically, A_M is the area between two parallel chords of an ellipse, separated by h (8 mm). Equation 6.108 describes the ellipse representing the mirror given a horizontal tilt angle of θ_x:

$$r_M^2 = \frac{x^2}{\cos^2\theta_x} + y^2 \tag{6.108}$$

The corresponding area captured by the mirror, A_M, can then be calculated by Equation 6.109:

$$A_M = \begin{cases} 2\cos\theta \displaystyle\int_{d-\frac{h}{2}}^{d+\frac{h}{2}} \sqrt{r_M^2 - y^2}dy, & 0 \leq d < r_M - \dfrac{h}{2} \\ 2\cos\theta \displaystyle\int_{d-\frac{h}{2}}^{r_M} \sqrt{r_M^2 - y^2}dy, & r_M - \dfrac{h}{2} \leq d \leq t + h \end{cases} \tag{6.109}$$

For the first case when 0 mm $\leq d <$ 3.5 mm, and $r_M = 7.5$ mm as according to the dimensions in Figure 6.10:

$$\begin{aligned} A_M =& 2\cos\theta_x \int_{d-4}^{d+4} \sqrt{7.5^2 - y^2}dy \\ =& \cos\theta_x \Big[(d+4)\sqrt{7.5^2-(d+4)^2} - (d-4)\sqrt{7.5^2-(d-4)^2} \\ &+ 7.5^2\left(\sin^{-1}\frac{d+4}{7.5} - \sin^{-1}\frac{d-4}{7.5}\right)\Big] \end{aligned}$$

Then for the second case when 3.5 mm $< d \leq$ 11.5 mm:

$$\begin{aligned} A_M &= 2\cos\theta_x \int_{d-4}^{7.5} \sqrt{7.5^2 - y^2}dy \\ &= \cos\theta_x \left[-(d-4)\sqrt{7.5^2-(d-4)^2} + 7.5^2\left(\frac{\pi}{2} - \sin^{-1}\frac{d-4}{7.5}\right)\right] \end{aligned}$$

6.3.3 Receiver Area A_r

A_r is defined by the intersection of an elliptical mirror projection and circular receiver aperture, as shown in Figure 6.12. The receiver's circle is described by Equation 6.110.

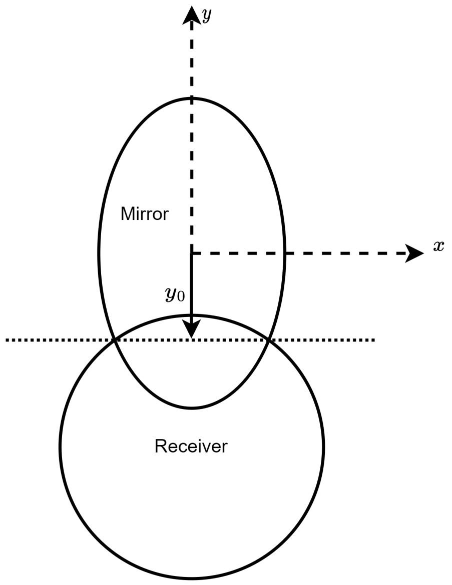

Figure 6.12. Tilted mirror and receiver area relative geometry

$$r_R^2 = x^2 + (y + r_R + t + h/2 - d)^2 \tag{6.110}$$

The vertical intersection offset, y_0, between the receiver circle and mirror ellipse can be found by finding the point of intersection between both curves. I solved for y_0 by beginning with Equation 6.111, assuming the mirror ellipse and receiver circle have equal

x values at their point of intersection.

$$x_{receiver} = x_{mirror} \tag{6.111}$$

$$\sqrt{r_R^2 - (y_0 + r_R + t + h/2 - d)^2} = \cos\theta_x \sqrt{r_M^2 - y_0^2} \tag{6.112}$$

I defined a temporary variable $\tau = r_R + t + \frac{h}{2}$ to simplify notation:

$$\sqrt{r_R^2 - (y_0 + \tau - d)^2} = \cos\theta_x \sqrt{r_M^2 - y_0^2} \tag{6.113}$$

$$r_R^2 - (y_0 + \tau - d)^2 = (r_M^2 - y_0^2)\cos^2\theta_x \tag{6.114}$$

$$(\cos^2\theta_x - 1)y_0^2 - 2(\tau - d)y_0 = -r_R^2 + r_M^2\cos^2\theta_x + (\tau - d)^2 \tag{6.115}$$

$$(-\sin^2\theta_x)y_0^2 - 2(\tau - d)y_0 = -r_R^2 + r_M^2\cos^2\theta_x + (\tau - d)^2 \tag{6.116}$$

Using the quadratic formula, for the case when $\theta_x \neq 0$:

$$y_0 = \frac{2(\tau - d) \pm \sqrt{4(\tau - d)^2 - 4(-\sin^2\theta_x)[r_R^2 - \cos^2\theta_x r_M^2 - (\tau - d)^2]}}{2(-\sin^2\theta_x)} \tag{6.117}$$

$$y_0 = \frac{(\tau - d) \pm \sqrt{(\tau - d)^2 + \sin^2\theta_x[r_R^2 - \cos^2\theta_x r_M^2 - (\tau - d)^2]}}{-\sin^2\theta_x} \tag{6.118}$$

$$y_0 = \frac{(d - \tau) \pm \sqrt{\cos^2\theta_x(\tau - d)^2 + \sin^2\theta_x[r_R^2 - \cos^2\theta_x r_M^2]}}{\sin^2\theta_x} \tag{6.119}$$

Using the prototype dimensions:

$$y_0 = \frac{(d - 17.5) + \sqrt{\cos^2\theta_x(17.5 - d)^2 + \sin^2\theta_x(10^2 - 7.5^2\cos^2\theta_x)}}{\sin^2\theta_x} \tag{6.120}$$

However, for the special case when $\theta_x = 0$:

$$-2(\tau - d)y_0 + r_R^2 - r_M^2 - (\tau - d)^2 = 0 \tag{6.121}$$

$$y_0 = \frac{r_R^2 - r_M^2 - (\tau - d)^2}{2(\tau - d)} \tag{6.122}$$

Using the prototype dimensions:

$$y_0 = \frac{10^2 - 7.5^2 - (17.5 - d)^2}{2(17.5 - d)} \tag{6.123}$$

The receiver area, A_r, can therefore be computed as in Equation 6.124.

$$A_r = 2\int_{y_0}^{d-r_M} \sqrt{r_R^2 - (y + r_R + t + h/2 - d)^2}dy + 2\cos\theta \int_{-r_M}^{y_0} \sqrt{r_M^2 - y^2}dy \tag{6.124}$$

Inserting the actual dimensions of the prototype:

$$A_r = 2\int_{y_0}^{d-7.5} \sqrt{10^2 - (y + 17.5 - d)^2}dy + 2\cos\theta_x \int_{-7.5}^{y_0} \sqrt{7.5^2 - y^2}dy \tag{6.125}$$

$$= 10^2\left[\frac{\pi}{2} - \sin^{-1}\left(\frac{y_0 + 17.5 - d}{10}\right)\right] - (y_0 + 17.5 - d)\sqrt{10^2 - (y_0 + 17.5 - d)^2} \tag{6.126}$$

$$+ y_0\cos\theta_x\sqrt{7.5^2 - y_0^2} + 7.5^2\cos\theta_x\left[\sin^{-1}\left(\frac{y_0}{7.5}\right) + \frac{\pi}{2}\right] \tag{6.127}$$

6.3.4 Optimization of Area Ratio

I found the maximum area ratio, J, for varying mirror tilt angles, θ, numerically using MATLAB with a step size for d of 0.0001 mm. Table 7 summarizes the optimal height to set the laser rangefinder, d for different key mirror tilt angles. Angles of $\theta_x = 20°$ and $\theta_x = 70°$ represent the farthest tilt angles for the Optotune MR-15-30 mirror as set up in the prototype, with the default position being $\theta_x = 45°$. The position $d = 5.865$ presents the best choice for the prototype as an in-between for both extremes, as such it is what was chosen for further range calculations.

Table 7. Area ratio for key mirror tilt angles

θ_x **[deg]**	d **[mm]**	J_{max} **[mm^2]**
20	5.910	17.894
45	5.865	10.947
70	5.783	2.774

Figure 6.13 shows that the optimal mirror position varies between 5.918 mm and 5.750 mm for different mirror tilt angles. The mirror position is static and so should be chosen to give an adequate value regardless of mirror tilt angle. An average position value between the extremes of the mirror range of motion would therefore be appropriate.

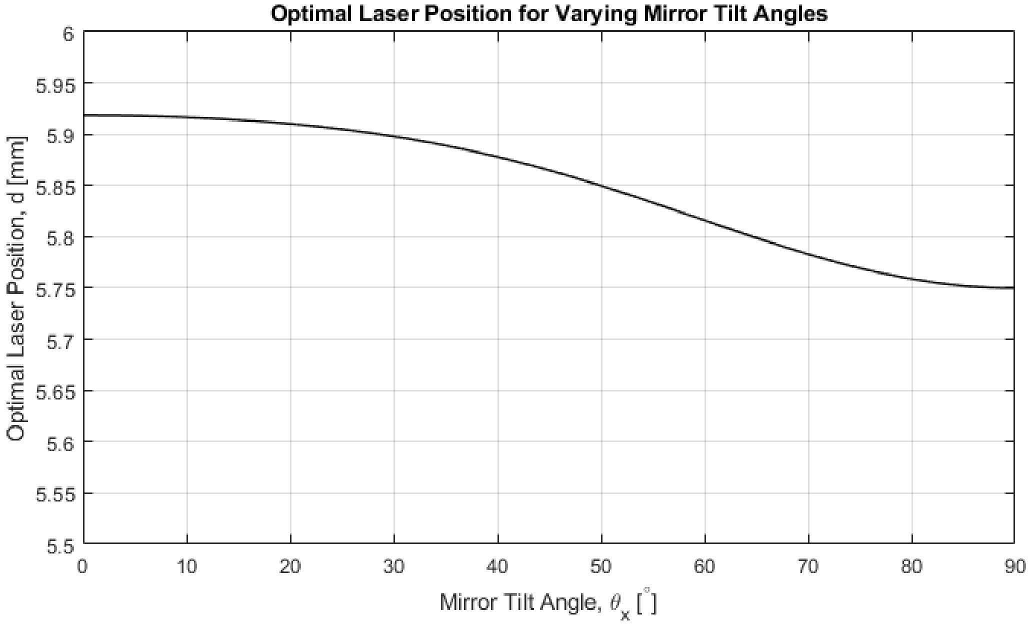

Figure 6.13. Optimal mirror position for different mirror tilt angles, for completeness all angles between 0° and 90° are provided.

Plotting the optimal area ratios for different mirror tilt angles, as in Figure 6.14 shows that the optimal area ratio, J_{opt}, starts to decrease quickly once mirror tilt angles increase past 20°.

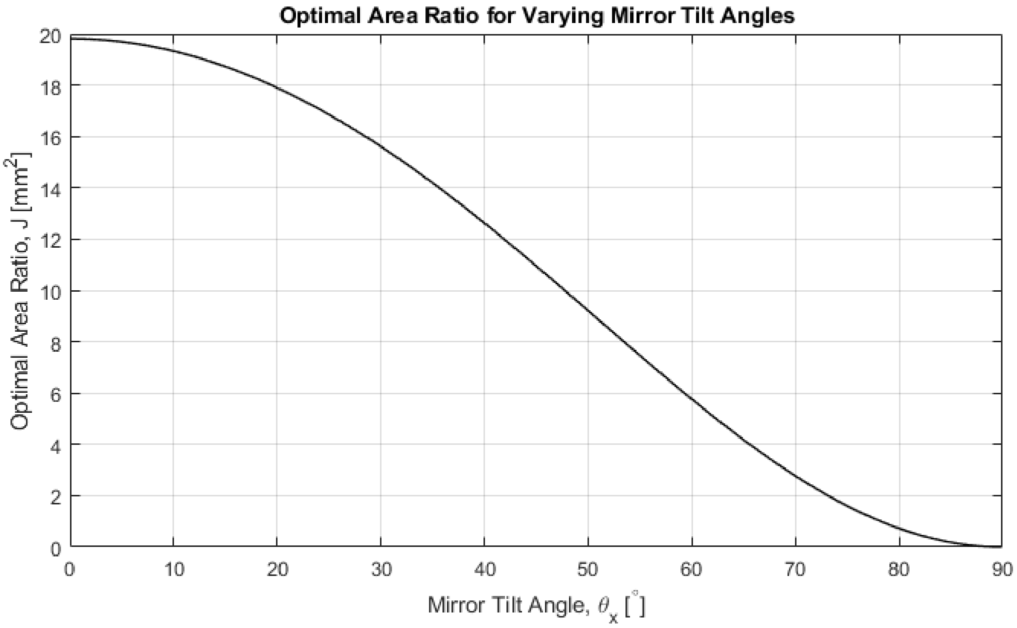

Figure 6.14. Optimal area ratio, J_{opt}, for different mirror tilt angles. For completeness, all angles between 0° and 90° are provided.

This decrease in the optimal area ratio, J_{opt}, suggests that a hardware configuration in which mirror tilt angles are kept as shallow as possible is preferred to maximize ranging performance. However such a head-on configuration creates a blind spot in the middle of the field-of-regard as this location would be occupied by the range finder. Worse, this occlusion becomes larger the closer the laser rangefinder is to the mirror. As such, I chose to keep the 45° default orientation for the prototype to avoid this issue.

6.4 Prototype Range Testing Results

To validate the theoretical model, I conducted experiments using the prototype in a series of hallways of different lengths. I positioned the prototype at the end of a hallway and had it perform laser measurements in concentric circles up to 3 degrees from the default pointing axis. This scanning pattern was used to help mitigate the possibility of any small angle misalignment in the assembly of the prototype. The prototype stepper motor was used to adjust the vertical alignment of the LRF relative to the FSM in steps of 0.25 mm. For each vertical offset, the prototype performed a scan to attempt detecting the end of the hallway. When a successful return from the hallway wall occurred I recorded the vertical offset, d, along with the measured hallway length. The highest and lowest vertical offset for the hallway of a given length was used in the final analysis, representing the cut-off offsets for the system. This process was repeated in five hallways of varying lengths, yielding a total of ten data points to compare with the model. Figure 6.15 compares the theoretical model to the experimental data.

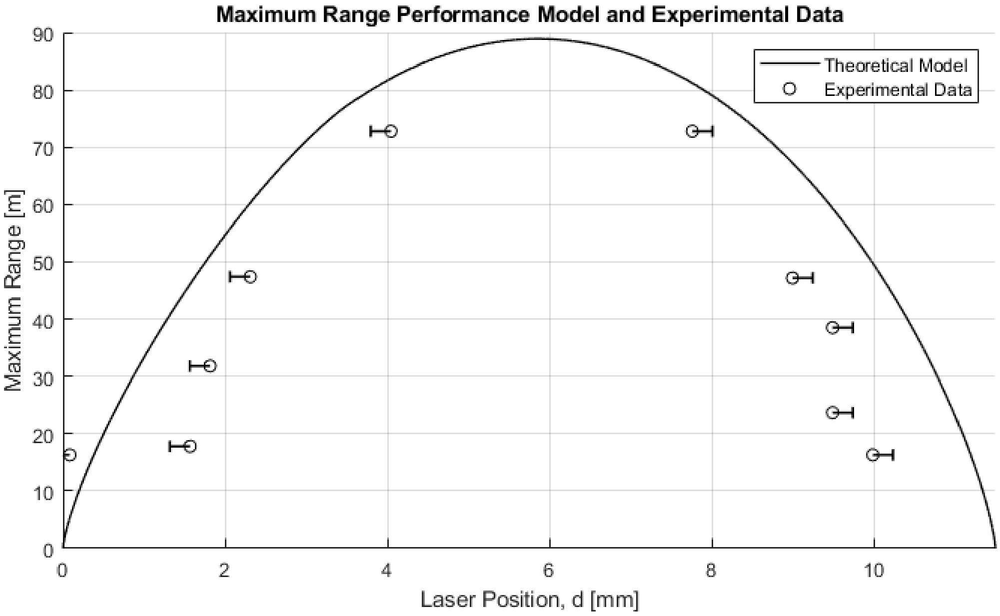

Figure 6.15. Radar equation theoretical model for target reflectance of 0.1 plotted alongside experimental data. Error bars denote the uncertainty in where the true cutoff is for a given range measurement due to the step size used in experiment.

Although the experimental data set consists of only 10 measurements, the measured ranges follow the general trend of the model, demonstrating that the model reasonably explains the occlusions effect on ranging performance. The experimental data appears pushed inward compared to the model, suggesting possible additional losses not accounted for by the model. This loss is possibly due to non-normal incidence between the laser and hallway wall, vertical tilt angle of the mirror relative to the laser, or variations in hallway wall surface reflectance. Overall, the geometric model estimating ranging performance appears reasonably validated by the experimental data, particularly in its ability to estimate an optimal geometric placement of the laser relative to the mirror.

6.5 Maximum Detectable Range Analysis Results

In this section I provide analytical results based on combining Equations 6.102 and 6.103 with the laser to mirror optimization in Section 6.3.4 to determine theoretical range limits of the prototype in a space-based setting. Table 8 details the parameters input into Equations 6.102 and 6.103.

Table 8. Maximum detectable range analysis input parameters based on prototype specifications

Parameter	**Symbol**	**Value**	**Units**
Mirror tilt angle	θ_x	45	deg
Laser height	d	5.865	mm
Effective area ratio	J	10.947	mm^2
Mirror reflectivity	ρ_M	0.95	-
Diffuse target reflectivity	$\rho_{diffuse}$	0.5	-
Retroreflector reflectivity	$\rho_{retroreflective}$	0.85	-
Beam divergence	α	0.4×10^{-3}	rad
Light wavelength	λ	1550	nm
Power ratio threshold	$\left(\dfrac{P_T}{P_R}\right)_0$	1.99×10^{-12}	-

Figures 6.16 and 6.17 plot the maximum achievable range for diffuse and retroreflective targets according to Equations 6.102 and 6.103 respectively.

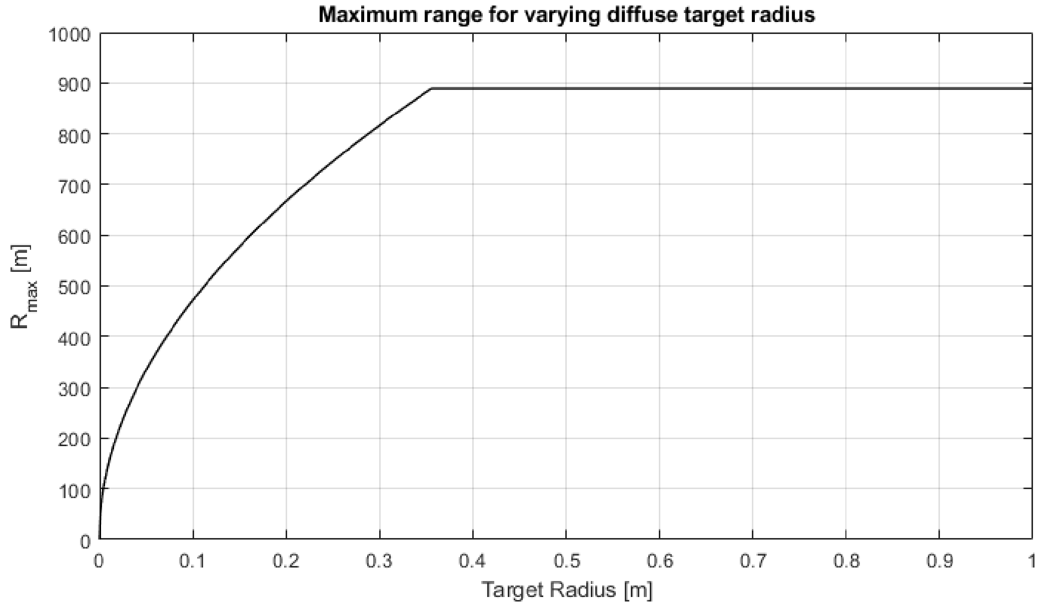

Figure 6.16. Maximum detectable range for diffuse targets of varying size, discontinuity occurs when target becomes beam-filling.

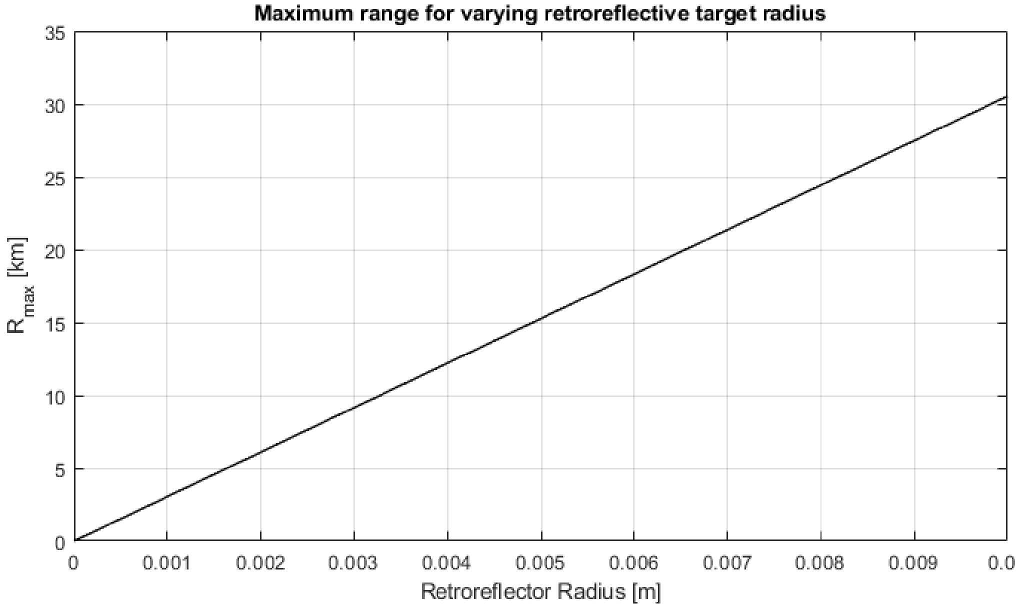

Figure 6.17. Maximum detectable range for retroreflective targets of varying size, target size axis scaled to represent typical retroreflector sizes [56], [78].

Based on the results of this analysis I expect that under idealized conditions the ranging prototype can achieve detection ranges close to 900 metres for diffuse targets and greater than 15 kilometres for general retroreflective targets. However, these results assume the mirror is not steering the laser and the target surface is perpendicular to the observer. As evidenced by the analysis in Section 6.3.4, the mirror tilt angle has a meaningful effect on ranging performance, creating an assymetrical field of regard. That is, one side of the FOR can only detect targets very close to the observer and the other side can detect targets both near and far. Regardless, the ideal diffuse case limit of 900 metres is already dangerously close for an observing satellite, such that an attempt to make a detection at this distance would introduce unnecessary risk to a mission. For this reason alone, the hardware used on the ranging prototype is not appropriate for diffuse target ranging on a space-based system.

6.6 Theoretical Ranging Performance Without Mirror Occlusion

In this section I consider what size mirror would be required to fully capture the beam from a DLEM 20 LRF, and how much that would increase range performance. I determined the required mirror size by taking the overall dimensions of the DLEM 20, from Figure 6.10, and considered the mirror at it's max tip or tilt, 25° for both. This calculation is then completed by Equations 6.128 and 6.131.

$$\text{Mirror Length} = \frac{\text{DLEM Length}}{\cos(\text{Tilt Angle})} \tag{6.128}$$

$$\text{Mirror Length} = \frac{31.5}{\cos(25^\circ)} \tag{6.129}$$

$$\text{Mirror Length} = 34.8 \text{ mm} \tag{6.130}$$

$$\text{Mirror Width} = \frac{\text{DLEM Width}}{\cos(\text{Tip Angle})} \tag{6.131}$$

$$\text{Mirror Width} = \frac{20}{\cos(25^\circ)} \tag{6.132}$$

$$\text{Mirror Width} = 22.1 \text{ mm} \tag{6.133}$$

Therefore, a rectangular mirror with dimensions of 35 by 22 mm should be capable of capturing the entire emitted and returned signals for a DLEM 20 LRF.

If the occlusion effect is eliminated, the area ratio, J becomes the size of the receiver aperture, A_r. The DLEM 20 receiver aperture has an area of 314.2 mm^2. The non-occluded maximum range capability $R_{max,non}$ for diffuse targets is related to the occluded range capability, $R_{max,occ}$ through the ratio of the non-occluded J_{non} to the occluded J_{occ} used in the prior range analysis. For a diffuse target the maximum range scales by the square root of J and can be found by Equation 6.134.

$$R_{max,non} = R_{max,occ} \left(\frac{J_{non}}{J_{occ}} \right)^{1/2} \tag{6.134}$$

$$R_{max,non} = 900 \left(\frac{314.2}{10.947} \right)^{1/2} \tag{6.135}$$

$$R_{max,non} = 4,821 \text{ m} \tag{6.136}$$

Therefore the maximum range capability is predicted to increase to just under 5 km for a diffuse target if a properly sized mirror is used. The range capability when ranging a retroreflective target scales by the quartic root of J, and can therefore be found by Equation 6.137.

$$R_{non} = R_{occ} \left(\frac{J_{non}}{J_{occ}} \right)^{1/4} \tag{6.137}$$

$$R_{non} = R_{occ} \left(\frac{314.2}{10.947} \right)^{1/4} \tag{6.138}$$

$$R_{non} = 2.31 R_{occ} \tag{6.139}$$

Therefore, by using a properly sized mirror, the ranging capability of the DLEM 20 should increase by a factor of 2.31 compared to the result presented in Figure 6.17 for a retroreflective target.

6.7 Trade-off Summary

First, I summarize key findings from the analysis in this chapter here:

- The required mirror steering speed decreases as the nominal orbital distance between observer and target $(r_1 - r_0)$ increases.

- The FOR can effectively cap the ranging capability of the observer, depending on the relative orbital geometries.
- The overall system scanning rate must decrease to detect targets at increasing range, assuming all other hardware specifications remain the same.
- The beam divergence, FSM resolution, FSM repeatability, and target range define the accuracy of a given measurement.

Further, Table 9 summarizes the direct trade-offs discussed in this chapter. Note that the FOR does not directly increase the range capability, but can effectively cap R_{max} if the FOR is too small for a given orbital configuration.

Table 9. Effect of increased hardware characteristics on key performance parameters

Increased Hardware Parameter	R_{max}	f	**Measurement Accuracy**
Beam Divergence, α	↓	-	↓
LRF Measurement Time, t_{meas}	↑	↓	-
FSM Steering Speed, ω	-	↑	-
FSM Resolution, ν	-	-	↑
FSM Repeatability (1-σ), κ	-	-	↑
Mirror Size	↑	-	-
Field of Regard, β	↑	-	-

Table 16 in Chapter 8 summarizes the above trade-offs, alongside observed trade-offs regarding acquisition performance.

Chapter 7

Results and Discussion

> Portions of this chapter have been adapted and reproduced with permission (Appendix B) from:
> [22] W. M. Ediger and P. A. Ferguson, "Feasibility of space-based laser ranging for resident space object detection," in *AIAA SCITECH 2025 Forum*. DOI: `10.2514/6.2025-1163`. eprint: `https://arc.aiaa.org/doi/pdf/10.2514/6.2025-1163`. [Online]. Available: `https://arc.aiaa.org/doi/abs/10.2514/6.2025-1163`

The following chapter discusses the results from simulations and experiments. First, I present a simulated comparison between the Bayesian search algorithm discussed in Chapter 3 with the Archimedes spiral search, commonly used in optical communications [35], applied for a stationary object. The purpose of this comparison is to demonstrate that the Bayesian search algorithm generates patterns of comparable efficiency to prior search methods. Next, I present experimental results to validate the stationary target search simulation model by comparing hit rates and mean acquisition times. I then present experimental results for the case of a moving target, a rover with an attached photo detector and compare this to the simulation model output. Next, I present results for a simulation of an orbiting observer spacecraft viewing a target in three distinct orbital geometry cases at two nominal distances. This simulation demonstrates how the Bayesian search may perform on an actual SSA mission. Finally, I present results for similar simulations assuming a modeled camera measurement of the target is used to inform search and acquisition.

7.1 Stationary Target Acquisition Testing

To establish the efficacy of the Bayesian search algorithm I compared the acquisition performance of the Bayesian search algorithm outlined in Chapter 3 to an optimized Archimedes spiral search using Monte Carlo simulations. The Bayesian search algorithm used 50,000 particles to generate the pattern over a time span of 1,000 steps, or 50 seconds.

The Archimedes spiral is defined by the polar function presented in Equation 7.1, where r is the radius, β is the rate at which the spiral grows, and θ is the angle measured from the x-axis.

$$r = \beta\theta \tag{7.1}$$

I optimized the Archimedes spiral growth rate, β, for each target uncertainty case by using a numerical search, running Monte Carlo simulations with 10,000 runs for each growth rate. After I estimated the optimal spiral growth rate, a Monte Carlo simulation of 100,000 runs was used to compare the performance of the Bayesian search and the optimized Archimedes spiral. The resulting acquisition performance and mean time to acquire the target is given in Table 10 for targets with increasing positional uncertainty. I assumed the target uncertainty region to be a planar two-dimensional Gaussian distribution with mean centered in the search frame. The covariance used for this Gaussian was defined using standard deviation comparable to those that would occur in a real world conjunction event using the typical RSO TLE uncertainty from Flohrer [66]. For instance, in the case where the conjunction range between the two satellites is 50 km, I found the angular uncertainty by the small angle approximation, given in Equation 7.2.

$$\sigma_{angular} = \frac{\sigma_{TLE}}{\text{Range}} \tag{7.2}$$

$$\sigma_{angular} = \frac{471}{50,000} \tag{7.3}$$

$$\sigma_{angular} = 0.00942 \text{ rad} \tag{7.4}$$

In Table 10 the row titled *Approximate Equivalent Range* reports the range at which the corresponding angular uncertainty would occur, rounded to the nearest multiple of 10 km. Note that I computed the mean acquisition time for both search patterns by averaging only over successful acquisitions; runs in which the target was not acquired were omitted from this average.

Table 10. Bayesian Search vs Archimedes Spiral Search Performance Comparison

Angular Standard Deviation (rad)	0.005	0.01	0.015	0.05
Approximate Equivalent Range (km)	100	50	30	10
Spiral Acquisition	89.42%	51.34%	28.73%	3.11%
Bayes Acquisition	87.69%	49.28%	25.79%	2.51%
Spiral Mean Time (s)	14.77	21.42	23.30	24.45
Bayes Mean Time (s)	13.48	21.80	23.24	24.34

Comparing the performance of both patterns shows that the Bayesian search has very similar performance to the Archimedes spiral in both acquisition success and mean acquisition time. However, acquisition time is slightly faster for the Bayes search when the initial uncertainty is very low. As expected, the acquisition performance of both search types decreases with increasing target uncertainty. These results show that, when considering a stationary target, the Bayesian search algorithms performance is comparable to the typically employed Archimedes spiral search. Figure 7.1 plots the cumulative acquisition probability results from the Monte Carlo simulations.

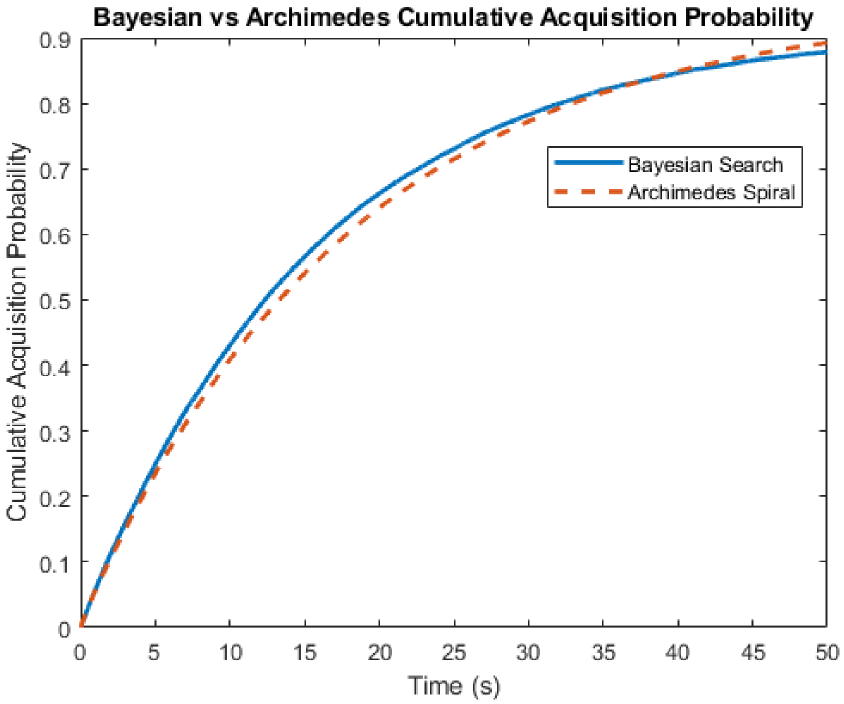

(a) Cumulative acquisition probability for 0.005 rad standard deviation

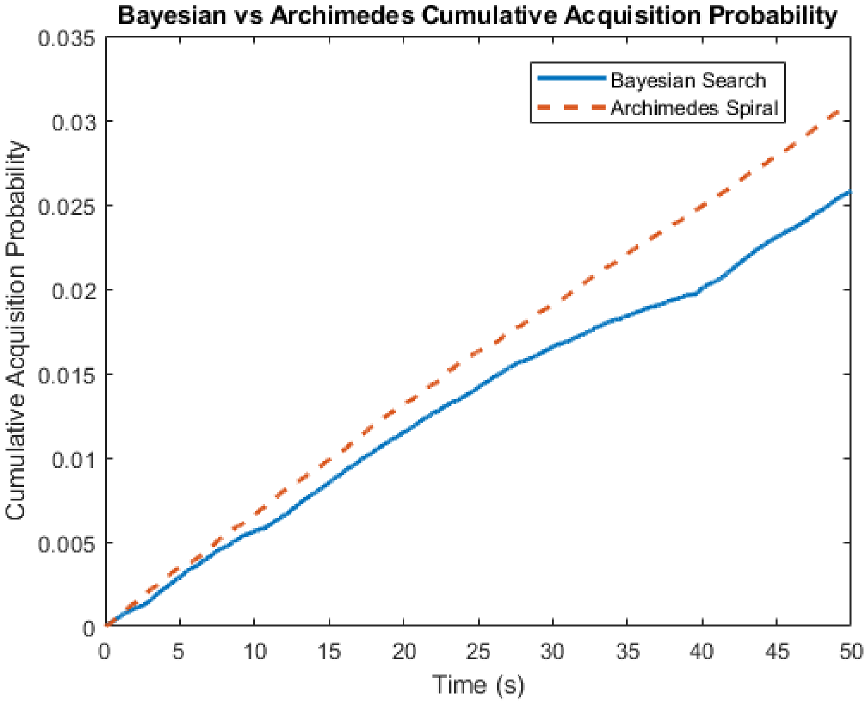

(b) Cumulative acquisition probability for 0.05 rad standard deviation

Figure 7.1. Cumulative probability of acquisition comparison between Bayesian and Archimedes spiral search simulation over entire search time (50 seconds) for 0.005 rad and 0.05 position standard deviations. The cumulative probability accounts for cases where the target was not acquired, therefore these plots do not span from 0 to 1 for cumulative probability. The cumulative probability at the end of the search time (50 seconds) is therefore the overall acquisition rate for each search.

To validate the simulation results I experimentally tested the acquisition performance of the Bayesian and Archimedes spiral patterns using the methodology outlined in Chapter 5. Ten runs of each search pattern were tested. Because it was not possible to precisely replicate the target position uncertainty in the experimental setup, the target uncertainty differed between the nominal simulation and experimental cases, potentially impacting performance outcomes. However, I wanted to compare acquisition performance between simulation and experiment with the same target position uncertainty. Therefore, I ran a new simulation using the same generated search pattern, using the experimentally observed target position variance as the target position uncertainty. After completing the ten runs for each pattern, I calculated the experimental target position mean and covariance parameters from the Vicon position data. The resulting experimental target position mean and covariance are provided in Equations 7.5 and 7.6 for the Bayesian search, and Equations 7.7 and 7.8 for the Archimedes spiral search. To temporally align the simulation with the experiment, I determined the prototype time step to be 0.124 seconds from the time intervals between measurements in the collected prototype data.

$$\mu_x = \begin{bmatrix} -16.8 \\ 7.0 \\ 3053.3 \end{bmatrix} \text{ mm} \tag{7.5}$$

$$\Sigma_x = \begin{bmatrix} 328.7 & -36.6 & 545.2 \\ -36.6 & 70.7 & -673.2 \\ 545.2 & -683.2 & 13697 \end{bmatrix} \text{ mm}^2 \tag{7.6}$$

$$\mu_x = \begin{bmatrix} 6.7 \\ -5.2 \\ 2514.3 \end{bmatrix} \text{ mm} \tag{7.7}$$

$$\Sigma_x = \begin{bmatrix} 260.2 & 75.9 & 2604.3 \\ 75.9 & 461.3 & -16.2 \\ 2604.3 & -16.2 & 213560.0 \end{bmatrix} (\text{mm})^2 \tag{7.8}$$

I then compared the simulated and experimentally measured mean acquisition rate (hit rate) and mean acquisition time for both search patterns. These results are summarized in Table 11.

Table 11. Bayesian search and Archimedes spiral experimental vs simulation search performance comparison

Type	Experiment	Simulation
Spiral Hit Rate	80.0%	63.5%
Bayes Hit Rate	100.0%	77.9%
Spiral Mean Acquisition Time (s)	51.4	50.3
Bayes Mean Acquisition Time (s)	42.3	37.9

Mean acquisition times were similar between simulation and experiment. The spiral's experimental mean acquisition time differed from its simulation by 2.19% and the Bayesian search's experimental mean acquisition time differed from its simulation by 11.61%. These percent differences were calculated using Equation 7.9.

$$\%\ \text{Difference} = \frac{\text{Experimental} - \text{Simulation}}{\text{Simulation}} 100\% \tag{7.9}$$

To determine whether the experimental hit rate results were consistent with the predicted performance from simulation I performed a hypothesis test analysis. I found that the acquisition hit rates were statistically consistent between the simulation and experimental data for both the Archimedes spiral and Bayesian search. This statistical analysis can be found in Appendix B.

7.1.1 Stationary Target Acquisition Discussion

Experimental testing of stationary target search patterns were statistically consistent with simulated performance. Mean acquisition times were also relatively close, with an error between simulation and experiment mean acquisition time found to be 2.19% for the Archimedes spiral and 11.61% for the Bayesian search. These results suggest that the simulation model has decent predictive validity of real prototype performance, at least when a target is stationary.

The Bayesian search algorithm appears to be a flexible alternative to a traditional Archimedes spiral search. The stationary target simulations comparing the Bayesian search and Archimedes spiral show comparable acquisition performance in terms of both hit rates and acquisition times. These results suggest that the Bayesian search pattern generation algorithm produces a search pattern that is reasonably efficient in terms of acquisition probability and time. The main concern with using the Bayesian search as opposed to a functional search such as the Archimedes spiral is the computational time and cost required to generate a pattern. Although I did not quantify computational cost, the Bayesian search relies on counting particles within bins and updating beliefs at each time step, whereas the Archimedes spiral is generated analytically. However, the Archimedes spiral does not have the flexibility of the Bayesian search, being that the Bayesian search algorithm can adapt to a wide variety of initial target position uncertainty distributions.

7.2 Moving Rover Testing

These results are from the test involving the moving rover and the prototype attempting to acquire the target using a Bayesian search, as described in Chapter 5. After collecting data for the ten trials with the moving rover, I calculated the position and velocity variance from the experimental Vicon data. These parameters are the position mean, μ_x, and position covariance, Σ_x, the velocity mean μ_v, and velocity covariance, Σ_v.

$$\mu_x = \begin{bmatrix} 1899.0 \\ 20.0 \\ 2042.2 \end{bmatrix} \text{ mm} \tag{7.10}$$

$$\Sigma_x = \begin{bmatrix} 4029.3 & -5.6 & -313.2 \\ -5.6 & 12.3 & 58.4 \\ -313.2 & 58.4 & 517.9 \end{bmatrix} \text{ mm}^2 \tag{7.11}$$

$$\mu_v = \begin{bmatrix} -152.5 \\ 0.0 \\ -3.6 \end{bmatrix} \text{ mm/s} \tag{7.12}$$

$$\Sigma_v = \begin{bmatrix} 374.3 & -1.4 & 75.9 \\ -1.4 & 0.1 & 0.1 \\ 75.9 & 0.1 & 62.9 \end{bmatrix} (\text{mm/s})^2 \tag{7.13}$$

The simulated performance of the Bayesian pattern using the experimentally measured target position and velocity variance suggested very poor performance. The experimental results were clearly consistent with the simulated search performance as the photodetector on the rover was not hit at all by the beam. Unfortunately, this result does not give a good description of how well the pattern tracked the rover in experiment, nor how well the mean detection time compares between simulation and experiment. Therefore, I decided to implement a "near miss" flag. This flag occurs when the laser pointing vector is within 0.1 degrees of the photodiode and was calculated by comparing the measured beam steering vectors from the Optotune fast steering mirror alongside the Vicon data of the target. The acquisition hit rates and near miss rates for the moving rover simulation and experiment are given in Table 12.

Table 12. Moving rover experimental vs simulation search performance comparison, photodetector basis

Type	Experiment	Simulation
Hit Rate	0.0%	0.91%
Mean Detection Time (s)	N/A	8.5
Near Miss Rate	20.0%	14.4%
Mean Near Miss Time (s)	7.7	8.6

I found that both the acquisition hit rates and near miss rates were statistically consistent between simulation and experiment. This statistical anlaysis can be found in Appendix B.

7.2.1 Moving Rover Testing Discussion

Experimental testing of the moving target search pattern was statistically consistent with simulated performance, both when using the 0.4 mrad detection condition and the 0.1 degree "near miss" condition. The results also show that if the laser beam had a width equal to the near miss condition then the hit rate would increase. This is expected as a wider beam should have an easier time acquiring a target since it illuminates a larger portion of the search space per time step. These experimental results suggest that the simulation model can reasonably capture general dynamics in systems with moving targets that have initial positional and velocity uncertainties.

Across all experimentally tested scenarios, the simulation model demonstrated predictive validity for search pattern acquisition performance. Statistical consistency between simulation and experiment indicates that the model can be trusted in cases where target dynamics and uncertainty are reasonably understood. The near miss condition results validate the expectation that a wider beam would theoretically achieve a higher acquisition rate compared to a narrow beam.

7.3 Simulated Camera-less Orbital Target Acquisition

This section details the acquisition performance results for orbital simulations where an observer is implementing a Bayesian search based on a target's TLE position uncertainty. Table 13 provides acquisition rates from the Monte Carlo simulation for search patterns generated by particle filters of varying sizes. There is a clear increase of acquisition rates with increasing particles, albeit with diminishing returns. In particular, search pattern generation in both parallel orbit cases deleted all particles before the target had left the observation field of regard, causing search patterns to end prematurely. This premature ending of search can be seen in Figure 7.2 for the parallel cases. However, even with the search ending early, the Bayesian search acquired the target over 85% of the time for both parallel orbit cases.

Table 13. Particle filter search pattern target acquisition rates for varying number of particles and orbital geometries

20 km Nominal Radial Distance Altitudes: Target (RCM-2) 597 km, Observer 577 km			
Particles	**Opposite**	**Perpendicular**	**Parallel**
100	2.49 %	3.40 %	11.30 %
1,000	3.63 %	4.30 %	57.20 %
10,000	4.25 %	4.84 %	82.86 %
20,000	4.52 %	5.72 %	87.75 %

50 km Nominal Radial Distance Altitudes: Target (RCM-2) 597 km, Observer 547 km			
Particles	**Opposite**	**Perpendicular**	**Parallel**
100	18.39 %	18.35 %	40.94 %
1,000	35.78 %	40.43 %	83.38 %
10,000	39.29 %	46.79 %	95.40 %
20,000	40.15 %	47.01 %	96.77 %

Generated search patterns follow geometric expectations based on how the target would appear to travel from the perspective of the observing spacecraft. For instance, the search pattern for opposite and parallel orbit configurations sweep across the observer's along-track axis. The perpendicular orbit configuration follows a diagonal between the observer's along-track and cross-track axes, due to the combined motion of the observer (along-track) and target (cross-track). Search patterns for the 20 km separation cases are given in Figure 7.2, patterns start in the positive along-track and progress towards the negative along-track.

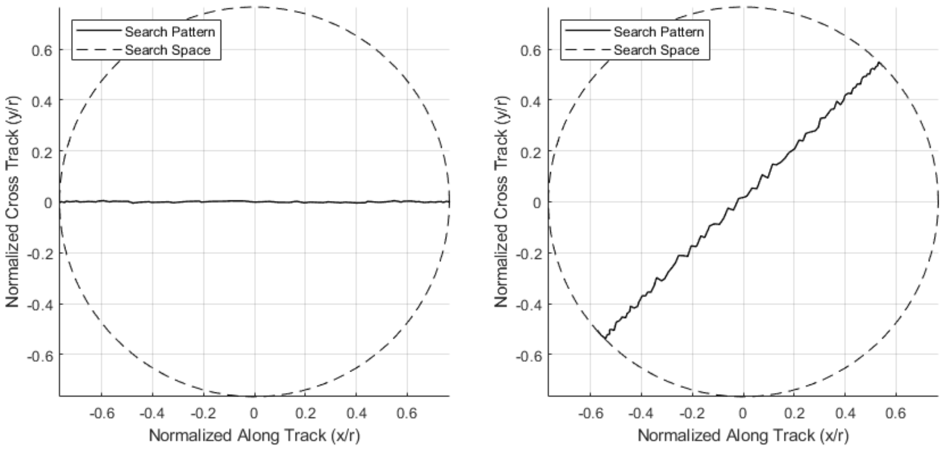

(a) Opposite search pattern (b) Perpendicular search pattern

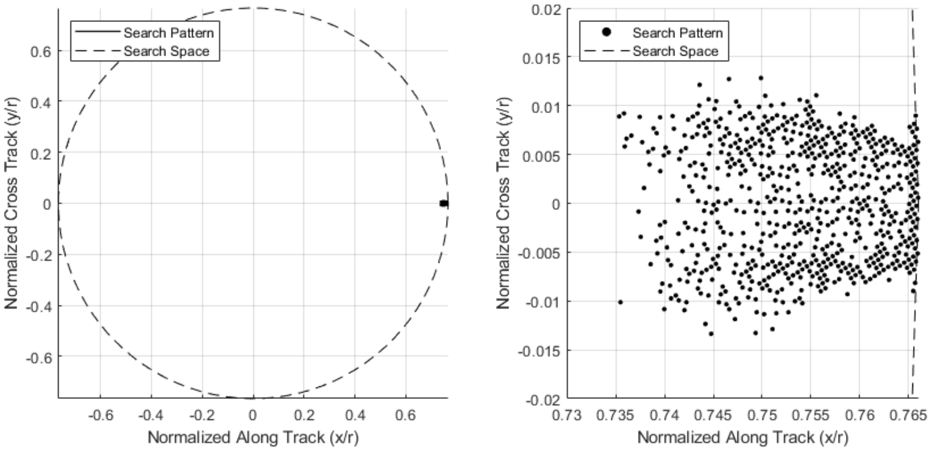

(c) Parallel search pattern, outliers filtered (d) Parallel search pattern, zoomed

Figure 7.2. 20 km radial separation search patterns from observer's perspective. Search pattern vectors are normalized as unit vectors and projected on to the along-track/cross-track plane. From converting spherical to Cartesian coordinates: $\frac{x}{r} = \cos\phi \sin\theta$ and $\frac{y}{r} = \sin\phi \sin\theta$.

Target acquisition statistics are summarized in Table 14. Acquisition time statistics are calculated exclusively from the instances where a target was acquired, excluding those where no target was acquired. For example, of all times a target was hit in the 20 km opposite orbital scenario, the average time recorded for a target to be hit was 1.54 seconds. For the opposite and perpendicular orbital cases the maximum search time is equivalent to the total acquisition time, whereas this is not true for the parallel orbit cases, due to their search pattern's early end.

Table 14. Monte Carlo simulation target acquisition performance for different orbital geometries with nominal observer to target orbital distances of 20 km and 50 km. All search patterns used for Monte Carlo simulations were generated using 20,000 particles

20 km Nominal Radial Distance Altitudes: Target (RCM-2) 597 km, Observer 577 km			
Metric	**Opposite**	**Perpendicular**	**Parallel**
Acquisition Success Rate	4.52 %	5.72 %	87.75 %
Maximum Search Time (s)	3.30	4.65	111.05
Mean Acquisition Time (s)	1.54	2.26	61.06
Median Acquisition Time (s)	1.25	2.18	59.95
Acquisition Time Std. Dev. (s)	1.13	1.51	17.80

50 km Nominal Radial Distance Altitudes: Target (RCM-2) 597 km, Observer 547 km			
Metric	**Opposite**	**Perpendicular**	**Parallel**
Acquisition Success Rate	40.15 %	47.01 %	96.77 %
Maximum Search Time (s)	7.95	11.25	45.90
Mean Acquisition Time (s)	3.13	4.20	26.12
Median Acquisition Time (s)	2.05	2.85	25.90
Acquisition Time Std. Dev. (s)	2.69	3.57	6.41

Figure 7.3 provides cumulative distributions for target acquisition over time for each orbital case. The cumulative distribution functions show that 50 km separated orbits have steeper slopes compared to their respective 20 km separated cases, indicating faster target acquisition for the 50 km separation. This is expected, the beam width at higher distances is effectively larger and can therefore capture more particles per measurement, leading to faster target acquisition convergence. Acquisition success rates for all 50 km cases are higher than their 20 km counterparts, likely due to longer search windows and larger beam widths.

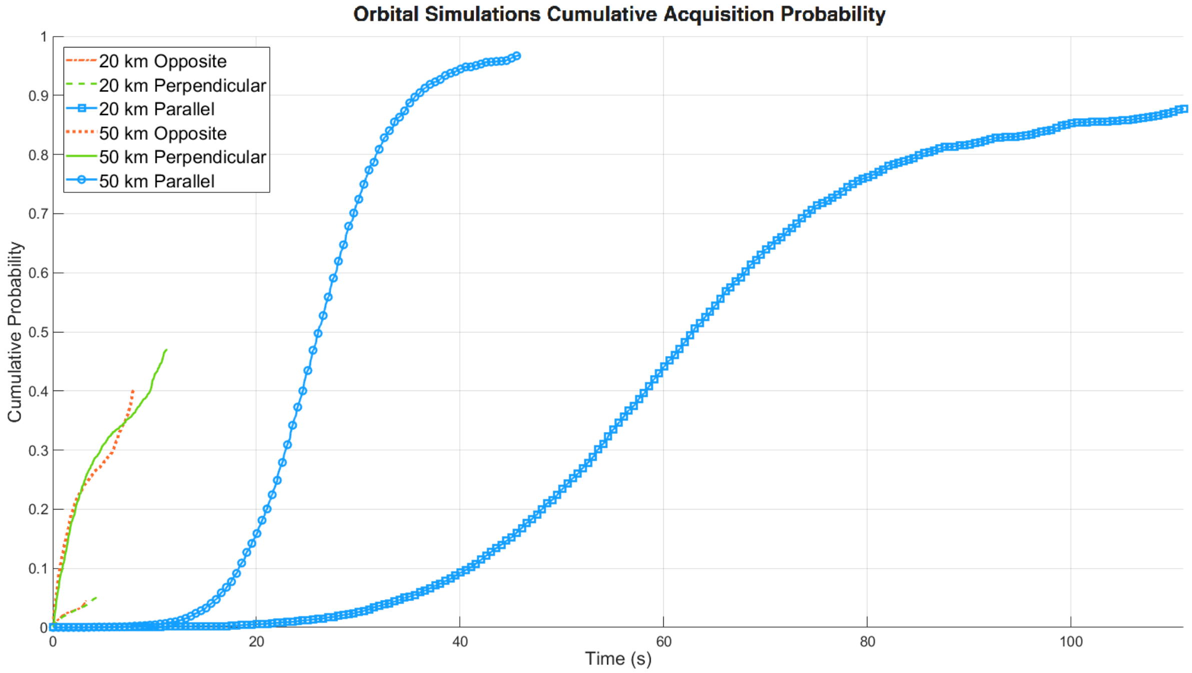

Figure 7.3. Cumulative probability of acquisition comparison for orbital Bayesian search simulation over entire search time for various orbital configurations. The cumulative probability accounts for cases where the target was not acquired, therefore these plots do not all span from 0 to 1 for cumulative probability. The cumulative probability at the end of each orbital configurations effective search time is therefore the overall acquisition rate for each search.

7.3.1 Simulated Camera-less Orbital Target Acquisition Discussion

The Bayesian search pattern generation algorithm shows convergent performance with increased particle sampling. Still, there are issues with this technique, especially for cases with prolonged tracking windows. Long tracking windows, such as those in the parallel orbit cases, often result in the complete deletion of all particles, causing the search patterns to end prematurely, as evidenced by the abrupt end of the search in Figure 7.2c. Periodically reseeding particles throughout the search pattern generation process may prevent the total deletion of all particles. However, this early end to a search pattern does not seem to heavily impact overall acquisition performance as both parallel orbit cases had acquisition rates over 85%.

Target acquisition performance appears highly dependent on both total available tracking time and the initial target angular positional uncertainty relative to the observer. This is made clear by noting the universally higher target acquisition success rates for 50 km nominal target distance compared to the 20 km distance in Figure 7.3. These results suggest that reducing initial angular uncertainty is an effective way to increase acquisition rates. Therefore the combination of a laser tracking system with other RSO detecting sensors capable of providing higher accuracy angular position information warrants exploration. With acquisition rates below 6%, relying solely on TLE data appears insufficient for acquiring targets at ranges below 20 km in non-parallel orbital geometries.

7.4 Camera Initiated Simulated Orbital Target Acquisition

Target acquisition statistics for Monte Carlo simulations of the Bayesian search initiated by combining simulated camera detection based on the specifications of CASSIOPIEs Fast Aural Imager (FAI) are summarized in Table 15. The details regarding the set up for these simulations can be found in Chapter 4. I investigated the opposite and perpendicular orbital cases at nominal radial distances between observer and target of 20 and 50 kilometres for these simulations, but deliberately did not explore the parallel orbital cases. I did not explore the parallel orbital case since a proper comparison of performance between TLE and camera based simulations would be difficult because of the particle attrition problem present in the TLE initiated simulation. Regardless of the particle attrition problem with the parallel orbital case, the Bayesian search already showed extremely high acquisition success using just TLE uncertainty information alone, any improvements from a camera would necessarily be marginal.

Table 15. Camera vs TLE initiated simulation target acquisition statistics

20 km Nominal Radial Distance Altitudes: Target (RCM-2) 597 km, Observer 577 km		
	Opposite	**Perpendicular**
TLE Acquisition	4.52%	5.72%
Camera Acquisition	7.80%	28.40%
Acquisition Improvement	72.57%	396.50%
TLE Mean Time (s)	1.54	2.26
Camera Mean Time (s)	1.52	1.79
Mean Time Improvement	-1.32%	-20.80%

50 km Nominal Radial Distance Altitudes: Target (RCM-2) 597 km, Observer 547 km		
	Opposite	**Perpendicular**
TLE Acquisition	40.15%	47.01%
Camera Acquisition	72.00%	98.20%
Acquisition Improvement	79.33%	108.89%
TLE Mean Time (s)	3.13	4.20
Camera Mean Time (s)	3.20	0.87
Mean Time Improvement	2.24%	-79.29%

For all explored cases, camera initiated search substantially improved acquisition rates, with greater acquisition improvement for the perpendicular case compared to the opposite orbital case. The acquisition rate improvement for the 20 kilometre perpendicular case was particularly high compared to the improvement for the 50 kilometre perpendicular case. Mean acquisition times stayed relatively the same for both opposite orbital cases, but showed meaningful improvement in the perpendicular cases.

7.4.1 Camera Initiated Simulated Orbital Target Acquisition

Camera initiated search simulations demonstrated that the information from even a single camera measurement can meaningfully improve acquisition performance compared to relying solely on TLE initiated searches. Acquisition performance improvement was particularly high for the perpendicular orbital case at a nominal distance of 20 km, suggesting that camera measurements show greater efficacy at close ranges compared to farther distances. This makes sense from a geometric stand-point as regardless of distance the angular width of a pixel remains constant, while the angular width of the TLE uncertainty region reduces with distance. As such, the initial uncertainty reducing effect of an image of a target should be greater at closer relative distances.

Chapter 8

Conclusions

This thesis investigated the feasibility and limitations of using space-based laser ranging systems for resident space object detection. I assessed the feasibility of space-based laser ranging through analysis, simulation, and experimental testing. Importantly, my hypotheses regard space-based laser ranging systems with and without cameras separately. In the following sections I restate each hypothesis and detail how my key contributions correspond with each.

8.1 Hypothesis 1

Hypothesis 1: *A steerable single-point laser rangefinder system consisting of a laser range finder and high-accuracy steerable mirror can acquire and range targets with relative angular rates similar to those observed in low Earth orbit (LEO) conjunction events at distances exceeding 1 km. Target acquisition can be achieved by using predictive dynamics to optimize a search pattern within a dynamic uncertainty region.*

I explored the feasibility of a space-based steerable single-point laser rangefinder system by performing analysis and modeling to relate orbital geometries to key performance metrics for a space-based laser ranging system, presented in Chapter 6. I also analyzed how key performance parameters are effected by key hardware specifications. The maximum detectable range and measurement accuracy were two of these performance parameters, evaluated in Chapter 6. Table 16 summarizes how increased hardware specifications impact these two performance parameters, along with the third important parameter, target acquisition. Target acquisition was evaluated through simulation and experimental results presented in Chapter 7.

A general challenge for fast steering mirrors is their small size, which raised concerns regarding ranging performance. I analyzed the effect of mirror size on maximum range using the radar equation alongside geometric modeling in Chapter 6. I validated this geometric modeling approach by testing the ranging capability of the prototype. The maximum detection range calculated using the radar equation model was just under a kilometre for diffuse reflecting targets and over 15 kilometres for retroreflective targets, depending on the retroreflector radius. This result contradicts my first hypothesis for ranging diffuse reflecting targets with a system using the same hardware as my prototype.

I assessed target acquisition performance using Monte Carlo simulations outlined in Chapter 4, and validated the predictive capability of the simulation method through experimental testing of a prototype outlined in Chapter 5. As presented in Chapter 7, the experimental results for the prototype were consistent with both stationary and moving target simulations when using a Bayesian search pattern algorithm. The results of the Monte Carlo orbital simulations suggest that target acquisition for most orbital configurations using a laser with a beam divergence equal to the prototype beam divergence is difficult at nominal orbital distances below 20 km. In the case of a 20 km nominal orbital distance, the target acquisition rate was below 6% for both the opposite and perpendicular orbital cases. Target acquisition was reasonably successful at nominal orbital distances of 50 km. At 50 km nominal distance, the probability of target acquisition was estimated to exceed 40%. For both the 20 and 50 km orbital distances, the parallel case showed quite high acquisition rates, exceeding 85% for both. Table 16 summarizes how acquisition success is improved or worsened by different design parameters.

Table 16. Key performance parameters and trade-offs

Increased Parameter	**Max Range**	**Accuracy**	**Acquisition**
Beam Divergence, α	Decrease	Worsen	Improve
Rangefinder Measurement Time, t_{meas}	Increase	Worsen	Worsen
Mirror Steering Speed, ω	-	Improve	Improve
Nominal Observer to Target Orbital Distance	-	Worsen	Improve
Mirror Size	Increase	-	-
Field of Regard	-	-	Improve
Initial Uncertainty Region Size	-	-	Worsen

Overall, my first hypothesis is partially supported by the results of this thesis. Although range modeling refutes feasibility for the case of ranging diffuse reflecting targets, the model supports the same prototype hardware being capable of ranging retroreflective targets. The development and evaluation of the Bayesian search pattern generation through both simulation and experimental testing partially supports the target acquisition portion of the hypothesis. Simulated target acquisition rates were reasonably successful for a nominal orbital distance of 50 km, while being largely unsuccessful for cases with a nominal orbital distance of 20 km. For the parallel orbital configurations for both 20 and 50 km nominal orbital distances were close to 90%. Overall, these results suggest that space-based laser ranging with the hardware investigated seems reasonably feasible with the following restrictions:

1. There is prior TLE information on the target with a LEO TLE positional and velocity uncertainty that is equal to or better than the average.
2. The nominal orbital distance between the LEO observer and target is at least 50 km, unless the orbital geometries have the two flying in the same direction in the same orbital plane where an orbital distance of 20 km was found acceptable.

Acquiring a target appears feasible for ranges exceeding 50 km, however retroflective targets can only be measured at ranges around 15 km. Therefore the limiting factor for measuring a target appears to be ranging capability. There are a few ways to improve the ranging performance of the system without heavily impacting acquisition performance. According to the models developed and analysis performed in Chapter 6, as nominal orbital distance between observer and target increases, the required mirror steering speed decreases. For an observer at an altitude of 575 km with a target at a nominal orbital distance of 50 km, the required observation angular speed at the point of conjunction is 0.3 rad/s. This speed is far slower than what the Optotune MR-15-30 is capable of, approximately 53.7 rad/s. Therefore if an operator were to focus on ranging targets at nominal orbital distances of 50 km or higher, then a slower, larger mirror is a reasonable change. A rectangular mirror with dimensions of 35 mm by 22 mm should be capable of capturing the entire emitted and returned signals for the DLEM 20. By eliminating the occlusion effect, the maximum range capability is predicted to increase to just under 5 km for diffuse targets and exceed 35 km for typical retroreflective targets. While 35 km range is still shy of 50 km, a higher power rangefinder or a rangefinder with a larger receiver aperture could be used to increase the maximum range. To achieve a 50 km range, the rangefinder power would only have to increase by a factor of about 4, as the DLEM is a 1 W rangefinder the increased power requirement is 4 W, which is a reasonable power draw for a small satellite. All together, these results suggest that it is feasible to range retroreflective targets without the need of a camera, given the above mentioned restrictions.

8.2 Hypothesis 2

Hypothesis 2: *Incorporating a target-detecting optical camera to provide pointing cues will improve system mean acquisition time and target acquisition performance by providing higher quality uncertainty estimates compared to solely relying on target two-line element propagation.*

My second hypothesis is supported by the simulated camera initiated orbital results in this thesis, outlined in Chapter 4. Orbital simulations of the Bayesian search pattern generation algorithm initiated using modeled camera measurements showed improved target acquisition performance for all cases compared to solely TLE initiated searches. Based on these Monte Carlo simulations, mean acquisition times also either improved or stayed the same. These results show that even a single measurement from a secondary sensor that improve the initial target state estimate also improve search and acquisition performance.

The Monte Carlo simulations that combined TLE information with a single modeled camera measurement of a target showed universal acquisition improvement for both opposite and perpendicular orbital cases. The acquisition rate for the opposite orbital 20 km distance case remained low, just below 8%, while the perpendicular case acquisition rate increased to just below 30%. Both opposite and perpendicular orbital cases for the 50 km nominal orbital distance had simulated acquisition rates over 70%. While 30% at first seems like a low acquisition rate, a satellite may pass by multiple targets per day. As such, 30% is reasonable for overall acquisition performance as nearly a third of passes are expected to produce a measurement. For the specific hardware I explored, implementing a camera cued measurement allows for reasonable acquisition of targets at 20 km nominal orbital distances in perpendicular configurations to the observer.

8.3 Discussion

The results of this thesis highlight the significant role that orbital geometry has in search and acquisition operations. As shown in the Monte Carlo simulation results, without the ability to detect targets at significant distances, target acquisition becomes extremely challenging for most orbital geometries without the aid of secondary sensors, such as RSO detecting cameras. Notably, however, acquisition appears very feasible for orbital geometries with low relative velocities and long tracking windows between observer and target, regardless of distance.

A key contribution of this thesis was demonstrating that even minimal secondary sensor input, such as a single measurement from a camera, can substantially improve search efficiency and reliability. The investigation of using a Bayesian search algorithm for target acquisition showed that TLE based searches are highly constrained to long distance measurements. The introduction of a secondary sensor to reduce initial uncertainty on a targets position greatly improved acquisition performance for unfavourable orbital geometries. Therefore, sensor fusion in space situational awareness missions seems to be very important for space-based RSO detecting systems where target observation windows are short.

Based on the feasibility constraints presented above, it appears that space-based laser ranging systems are technically feasible for short range tandem missions without retroreflectors and detecting general cooperative RSOs equipped with retroreflectors at nominal orbital distances above 50 km. Space-based laser ranging also appears feasible at ranges below 50 km with the aid of RSO detecting cameras and favourable orbital geometries. These findings underscore the importance of incorporating cooperative features on RSOs to enhance visibility, as well as reinforcing the importance of relative orbital geometries when planning space-based space situational awareness missions. Finally, these findings imply that space-based laser ranging alone is not particularly suitable for space debris detection, both because of range limitations and because of the potential lack of TLE information required for search operations.

8.4 Limitations

There are some key limitations that should be considered when evaluating the results of this thesis. First, although generalized where possible, many of the results in this thesis deal with specific pieces of hardware and the implied performance of their specifications. The Jenoptik DLEM 20 laser rangefinder has the constraint of being a low power solution in a small compact form factor. Using this off-the-shelf rangefinder prevents flexibility in orienting the receiver aperture relative to the emitter, which may exacerbate the rangefinder to mirror occlusion issue. Likewise, the Optotune MR-15-30 is, of course, limited in size and was not designed for compatibility with a DLEM 20 rangefinder. Based on the hardware specifications, a system using these two pieces of hardware was constrained to a scanning rate of 20 Hz for simulations. Whereas a higher scanning rate likely improves acquisition performance, broadening the scope of orbital geometries in which a space-based laser ranging system is feasible. Finally, the fast aural imager (FAI) on board CASSIOPIE was used for camera cued Monte Carlo simulations, but the FAI was not designed with RSO detection in mind. So, a higher accuracy RSO detecting camera may be possible and could further improve search and acquisition performance.

Second, the Bayesian search pattern generation algorithm used is not necessarily an optimized search solution. It is possible that a more efficient search strategy exists that outperforms the Bayesian search presented. A more efficient search strategy could also broaden the orbital cases where space-based laser ranging is feasible. I also note that I used the positional uncertainty associated with the average target TLE, where for a specific target this uncertainty may be higher or lower. If the positional accuracy for a specific TLE is higher than that for an average LEO TLE, I would expect the Bayesian search to have better acquisition performance compared to the results presented in my orbital simulations. Interestingly, to me this implies a feedback effect, where the more frequently a target is measured and therefore the positional uncertainty reduced, the easier it is to measure again, at least for the Bayesian search method. These limits regarding the prototype hardware and search algorithm suggest the results in this thesis are conservative compared to a hypothetical space-based system consisting of custom hardware.

8.5 Future Work

This thesis presents several interesting areas that merit future investigation into the feasibility and applications of space-based laser ranging. First, a comprehensive evaluation of available laser rangefinders and fast steering mirrors (among other steering methods) is warranted. Exploring the implications of different combinations of these devices would be a useful expansion on the general trade-offs derived in this thesis. Further, exploring the capabilities of custom hardware solutions optimized for detecting targets at far ranges would be very useful for assessing the general feasibility of space-based laser ranging systems.

Second, further investigation into the specific impacts of design parameters on search and acquisition performance would be useful for designing a better-performing system. I showed the general effects that adjustment of these parameters had on search and acquisition performance, but having a model that analyzes these effects in greater detail would further clarify the feasibility of space-based laser ranging systems.

Third, finding more efficient search and acquisition strategies would improve the feasibility of space-based laser ranging. Particularly, fusing continued target image information with the Bayesian target uncertainty cloud past just the first image could drastically improve target acquisition. I foresee the largest challenge with this approach being computational cost, taking too long to update the underlying distribution between measurements. A generalization of the underlying position uncertainty distribution using a functional, rather than numerical, relationship would drastically reduce computational cost. Related would be the exploration into other sensors for information fusion, such as radar.

Finally, further exploration into the effects of different relative orbital geometries on search and acquisition would help refine where space-based laser ranging is feasible. Related would be a robust study into the effect of relative orbital geometries on RSO detection accuracy as well, both for laser ranging and visual imaging. Work like this is useful for mission planning, both for space situational awareness missions but also in formation flying missions. Incorporating noise into measurement performance from external factors based on these orbital models would also help refine when and where RSO detecting satellites are best used.

References

[1] C. Van Camp and W. Peeters, “A world without satellite data as a result of a global cyber-attack,” *Space Policy*, vol. 59, p. 101 458, 2022, ISSN: 0265-9646. DOI: `https://doi.org/10.1016/j.spacepol.2021.101458`. [Online]. Available: `https://www.sciencedirect.com/science/article/pii/S0265964621000503`.

[2] U. S. Force, *About us*, Accessed: 2025-01-29, 2025. [Online]. Available: `https://www.spaceforce.mil/About-Us/`.

[3] F. Ministry of Armed Forces, *The french space command, organization and missions*, Accessed: 2025-01-29, 2025. [Online]. Available: `https://www.defense.gouv.fr/en/cde/organization-and-missions`.

[4] NASA Orbital Debris Program Office, “History of on-orbit satellite fragmentations, 16th edition,” National Aeronautics and Space Administration, Tech. Rep., 2022, pp. 4–10, 440. [Online]. Available: `https://orbitaldebris.jsc.nasa.gov/library/HOOSF_16e.pdf`.

[5] N. L. Johnson, E. Stansbery, J.-C. Liou, M. Horstman, C. Stokely, and D. Whitlock, “The characteristics and consequences of the break-up of the fengyun-1c spacecraft,” *Acta Astronautica*, vol. 63, no. 1, pp. 128–135, 2008, Touching Humanity - Space for Improving Quality of Life. Selected Proceedings of the 58th International Astronautical Federation Congress, Hyderabad, India, 24-28 September 2007, ISSN: 0094-5765. DOI: `https://doi.org/10.1016/j.actaastro.2007.12.044`. [Online]. Available: `https://www.sciencedirect.com/science/article/pii/S0094576507003281`.

[6] D. J. Kessler and B. G. Cour-Palais, “Collision frequency of artificial satellites: The creation of a debris belt,” *Journal of Geophysical Research: Space Physics*, vol. 83, no. A6, pp. 2637–2646, 1978. DOI: `https://doi.org/10.1029/JA083iA06p02637`. eprint: `https://agupubs.onlinelibrary.wiley.com/doi/pdf/10.1029/JA083iA06p02637`. [Online]. Available: `https://agupubs.onlinelibrary.wiley.com/doi/abs/10.1029/JA083iA06p02637`.

[7] I. Telichev, “Preliminary study on shielding performance of corrugated-plate-core vs. foam-core sandwich panels at hypervelocity impact,” *CEAS Space Journal*, Dec. 2024, ISSN: 1868-2510. DOI: `10.1007/s12567-024-00587-3`. [Online]. Available: `https://doi.org/10.1007/s12567-024-00587-3`.

[8] Federal Communications Commission, “Second report and order and memorandum opinion and order (fcc report fcc-22-74a1),” Federal Communications Commission, Washington, DC, Report and Order FCC 22-74A1, 2022, Adopts requirement for deorbiting non-GEO satellites within 5 years after end of mission, pp. 1–26.

[9] Inter-Agency Space Debris Coordination Committee (IADC), *Iadc space debris mitigation guidelines, revision 4*, `https://www.unoosa.org/res/oosadoc/data/documents/2025/aac_105c_12025crp/aac_105c_12025crp_9_0_html/AC105_C1_2025_CRP09E.pdf`, Presented to the United Nations Committee on the Peaceful Uses of Outer Space Scientific and Technical Subcommittee, February 2025, Various space agencies worldwide, 2025.

[10] J. Murray and T. Kennedy, “Haystack ultra-wideband satellite imaging radar measurements of the orbital debris environment: 2018,” National Aeronautics and Space Administration: Orbital Debris Program Office, Tech. Rep. TP-2020-5006606, 2020. [Online]. Available: `https://ntrs.nasa.gov/api/citations/20205006606/downloads/TP-2020-5006606_HUSIR%20CY18%20Report_final.pdf`.

[11] International Laser Ranging Service (ILRS), *Current satellite missions*, Accessed: 2024-11-20, 2024. [Online]. Available: `https://ilrs.gsfc.nasa.gov/missions/satellite_missions/current_missions/`.

[12] United States Space Force, *Ground-based electro-optical deep space surveillance*, Accessed: 2025-01-29, 2020. [Online]. Available: `https://www.spaceforce.mil/About-Us/Fact-Sheets/Article/2197760/ground-based-electro-optical-deep-space-surveillance/`.

[13] N. Aeronautics and S. Administration, *12.0 identification and tracking systems*, Accessed: 2025-01-29, 2024. [Online]. Available: `https://www.nasa.gov/smallsat-institute/sst-soa/identification-and-tracking-systems/`.

[14] B. Wallace, R. Scott, M. Sale, A. Hildebrand, and R. Cardinal, "The near Earth object surveillance satellite: Mission status and CCD evolution after 18 months on-orbit," in *Proceedings of the Advanced Maui Optical and Space Surveillance Technologies Conference (AMOS)*, Maui, HI, USA: Maui Economic Development Board, Sep. 2014. [Online]. Available: `https://amostech.com/TechnicalPapers/2014/Space_Systems/WALLACE.pdf`.

[15] R. Leitch and H. Ian, "Sapphire: A small satellite system for the surveillance of space," in *Proceedings of the AIAA/USU Conference on Small Satellites*, Utah State University, Logan, UT, USA, 2010. [Online]. Available: `https://digitalcommons.usu.edu/cgi/viewcontent.cgi?article=1194&context=smallsat`.

[16] Defence Research and Development Canada. "Tandem satellites will advance r&d in space domain awareness." Accessed: 2025-07-21. [Online]. Available: `https://science.gc.ca/site/science/en/blogs/defence-and-security-science/tandem-satellites-will-advance-rd-space-domain-awareness`.

[17] D. Vallado and P. Cefola, "Two-line element sets - practice and use," *Proceedings of the International Astronautical Congress, IAC*, vol. 7, pp. 5812–5825, Jan. 2012.

[18] A. de Ruiter, C. Damaren, and J. Forbes, *Spacecraft Dynamics and Control: An Introduction.* Wiley, 2012, p. 151, ISBN: 9781118403327.

[19] M. Navabi and R. Hamrah, "Close approach analysis of space objects and estimation of satellite-debris collision probability," *Aircraft Engineering and Aerospace*

Technology: An International Journal, vol. 87, Sep. 2015. DOI: `10.1108/AEAT-07-2013-0131`.

[20] W. Ediger *et al.*, "Spacedust-laser/rf: Time of flight methods for space situational awareness," in *Proceedings of the 2023 AMOS Conference*, Copyright © 2023 Advanced Maui Optical and Space Surveillance Technologies Conference (AMOS) – www.amostech.com, Advanced Maui Optical and Space Surveillance Technologies Conference (AMOS), 2023. [Online]. Available: `https://amostech.com/2023-technical-papers/`.

[21] Department of National Defence and the Canadian Armed Forces, *Collision course – tracking and de-orbiting space debris*, Accessed: 2025-01-29, 2024. [Online]. Available: `https://www.canada.ca/en/department-national-defence/programs/defence-ideas/element/competitive-projects/challenges/collision-course-tracking-deorbiting-space-debris.html`.

[22] W. M. Ediger and P. A. Ferguson, "Feasibility of space-based laser ranging for resident space object detection," in *AIAA SCITECH 2025 Forum*. DOI: `10.2514/6.2025-1163`. eprint: `https://arc.aiaa.org/doi/pdf/10.2514/6.2025-1163`. [Online]. Available: `https://arc.aiaa.org/doi/abs/10.2514/6.2025-1163`.

[23] W. Ediger and P. Ferguson, "Laser rangefinder and steering mirror optimization by radar and geometric modeling," in *2025 IEEE SENSORS*, 2025, pp. 1–4. DOI: `10.1109/SENSORS59705.2025.11330595`.

[24] C. Smith and B. Greene, "The eos space debris tracking system," in *The Advanced Maui Optical and Space Surveillance Technologies Conference*, S. Ryan, Ed., Jan. 2006, E86.

[25] M. Matney, "Measuring small debris – what you can't see can hurt you," Houston, Texas, USA, 2016. [Online]. Available: `https://ntrs.nasa.gov/api/citations/20160011226/downloads/20160011226.pdf`.

[26] M. A. Steindorfer, G. Kirchner, F. Koidl, P. Wang, B. Jilete, and T. Flohrer, “Daylight space debris laser ranging,” *Nature Communications*, vol. 11, no. 1, 2020. DOI: `10.1038/s41467-020-17332-z`.

[27] R. A. Mould, “Basic relativity,” in Springer, 2002, p. 8.

[28] M. W. Fitzmaurice, “Nasa ground-based and space-based laser ranging systems,” National Aeronautics and Space Administration Goddard Space Flight Center, Tech. Rep., 1978. [Online]. Available: `https://ntrs.nasa.gov/citations/19780009417`.

[29] M. R. Pearlman *et al.*, “The ILRS: Approaching 20 years and planning for the future,” *Journal of Geodesy*, vol. 93, no. 11, pp. 2161–2180, Nov. 2019, ISSN: 1432-1394. DOI: `10.1007/s00190-019-01241-1`. [Online]. Available: `https://doi.org/10.1007/s00190-019-01241-1`.

[30] G. Kirchner, F. Koidl, F. Friederich, I. Buske, U. Völker, and W. Riede, “Laser measurements to space debris from graz slr station,” *Advances in Space Research*, vol. 51, no. 1, pp. 21–24, 2013, ISSN: 0273-1177. DOI: `https://doi.org/10.1016/j.asr.2012.08.009`. [Online]. Available: `https://www.sciencedirect.com/science/article/pii/S0273117712005492`.

[31] M. Laas-Bourez, S. Wailliez, F. Deleflie, A. Klotz, D. Albanese, and N. Saba, “First astrometric observations of space debris with the méo telescope,” *Advances in Space Research*, vol. 49, no. 3, pp. 603–611, 2012, ISSN: 0273-1177. DOI: `https://doi.org/10.1016/j.asr.2011.11.007`. [Online]. Available: `https://www.sciencedirect.com/science/article/pii/S0273117711007666`.

[32] F. Fouladinejad, A. Matkan, M. Hajeb, and F. Brakhasi, “History and applications of space-borne lidars,” *The International Archives of the Photogrammetry, Remote Sensing and Spatial Information Sciences*, vol. XLII-4/W18, pp. 407–414, 2019. DOI: `10.5194/isprs-archives-XLII-4-W18-407-2019`. [Online]. Available: `https://isprs-archives.copernicus.org/articles/XLII-4-W18/407/2019/`.

[33] V. Chan, “Optical satellite networks,” *Journal of Lightwave Technology*, vol. 21, no. 11, pp. 2811–2827, 2003. DOI: `10.1109/JLT.2003.819534`.

[34] J. Ma, X. Li, S. Yu, L. Tan, and Q. Han, “Influence of satellite vibration on optical communication performance for intersatellite laser links,” *Optical Review*, vol. 19, no. 1, pp. 25–28, Jan. 2012, ISSN: 1349-9432. DOI: `10.1007/s10043-012-0004-z`. [Online]. Available: `https://doi.org/10.1007/s10043-012-0004-z`.

[35] H. Kaushal, V. Jain, and S. Kar, “Chapter 4,” in *Free Space Optical Communication*, ser. Optical Networks, 1st ed., New Delhi, India: Springer New Delhi, 2017, pp. 119–136, ISBN: 978-81-322-3691-7. DOI: `10.1007/978-81-322-3691-7`.

[36] Z. Kang, S. Bettadpur, P. Nagel, H. Save, S. Poole, and N. Pie, “GRACE-FO precise orbit determination and gravity recovery,” *Journal of Geodesy*, vol. 94, no. 9, p. 85, Aug. 2020, ISSN: 1432-1394. DOI: `10.1007/s00190-020-01414-3`. [Online]. Available: `https://doi.org/10.1007/s00190-020-01414-3`.

[37] J. Wojtanowski, M. Jakubaszek, M. Zygmunt, B. Sędek, and K. Wójcik, “The expected performance analysis of a retroreflector-supported inter-satellite laser rangefinder designed for polish imaging satellites (piast) space mission,” *Opto-Electronics Review*, vol. 32, no. 3, e150608, 2024. DOI: `10.24425/opelre.2024.150608`. [Online]. Available: `http://journals.pan.pl/Content/131567/PDF-MASTER/OPELRE_2024_32_3_J_Wojtanowski.pdf`.

[38] Y. Kaymak, R. Rojas-Cessa, J. Feng, N. Ansari, M. Zhou, and T. Zhang, “A survey on acquisition, tracking, and pointing mechanisms for mobile free-space optical communications,” *IEEE Communications Surveys & Tutorials*, vol. 20, no. 2, pp. 1104–1123, 2018. DOI: `10.1109/COMST.2018.2804323`.

[39] M. Milaševičius and L. Mačiulis, “A review of mechanical fine-pointing actuators for free-space optical communication,” *Aerospace*, vol. 11, no. 1, 2024, ISSN: 2226-4310. DOI: `10.3390/aerospace11010005`. [Online]. Available: `https://www.mdpi.com/2226-4310/11/1/5`.

[40] H. Zuo and S. He, “Extra large aperture fpcb mirror based scanning lidar,” *IEEE/ASME Transactions on Mechatronics*, vol. 27, no. 1, pp. 93–102, 2022. DOI: `10.1109/TMECH.2021.3058320`.

[41] T. Evans, “Optical development system life cycle for the icesat-2 atlas instrument,” in *2014 IEEE Aerospace Conference*, 2014, pp. 1–12. DOI: `10.1109/AERO.2014.6836306`.

[42] M. Hinkle, *ICESat-2 ATLAS Beam Steering Mechanism (BSM)*, NASA Technical Reports Server (NTRS) Document ID: 20150018098, 2015. [Online]. Available: `https://ntrs.nasa.gov/citations/20150018098`.

[43] TESAT Spacecom, *Scot20 optical communications terminal data sheet*, Accessed: 2025-03-10, 2024. [Online]. Available: `https://www.tesat.de/images/tesat/products/240306_DataSheet_SCOT20_A4_Druck.pdf`.

[44] AAC Clyde Space, *Cubecat lasercom module data sheet*, Accessed: 2025-03-10, 2021. [Online]. Available: `https://www.aac-clyde.space/wp-content/uploads/2021/10/CUBECAT-2.pdf`.

[45] N. Gordon, D. Salmond, and A. Smith, “Novel approach to nonlinear/non-gaussian bayesian state estimation,” *IEE Proceedings F (Radar and Signal Processing)*, vol. 140, pp. 107–113, 2 1993. DOI: `10.1049/ip-f-2.1993.0015`. eprint: `https://digital-library.theiet.org/doi/pdf/10.1049/ip-f-2.1993.0015`. [Online]. Available: `https://digital-library.theiet.org/doi/abs/10.1049/ip-f-2.1993.0015`.

[46] M. Nayak, J. Beck, and B. Udrea, “Design of relative motion and attitude profiles for three-dimensional resident space object imaging with a laser rangefinder,” in *2013 IEEE Aerospace Conference*, 2013, pp. 1–16. DOI: `10.1109/AERO.2013.6496837`.

[47] R. E. Kalman, “A new approach to linear filtering and prediction problems,” *Journal of Basic Engineering*, vol. 82, no. 1, pp. 35–45, Mar. 1960, ISSN: 0021-9223. DOI: `10.1115/1.3662552`. eprint: `https://asmedigitalcollection.asme.org/fluidsengineering/article-pdf/82/1/35/5518977/35\_1.pdf`. [Online]. Available: `https://doi.org/10.1115/1.3662552`.

[48] M. S. Grewal and A. P. Andrews, “Applications of kalman filtering in aerospace 1960 to the present [historical perspectives],” *IEEE Control Systems Magazine*, vol. 30, no. 3, pp. 69–78, 2010. DOI: `10.1109/MCS.2010.936465`.

[49] G. Soysal and M. Efe, “Kalman filter aided cooperative optical beam tracking,” *Radioengineering*, vol. 19, pp. 242–248, Jun. 2010.

[50] M. Driedger and P. Ferguson, “Feasibility study of an orbital navigation filter using resident space object observations,” *Journal of Guidance, Control, and Dynamics*, vol. 44, no. 3, pp. 622–628, 2021. DOI: `10.2514/1.G005210`.

[51] M. Zhang *et al.*, “Analysis of the ranging capability of a space debris laser ranging system based on the maximum detection distance model,” *Remote Sensing*, vol. 16, no. 4, p. 727, Feb. 2024, ISSN: 2072-4292. DOI: `10.3390/rs16040727`. [Online]. Available: `http://dx.doi.org/10.3390/rs16040727`.

[52] G. Blanchet, H. Haag, L. Hennegrave, F. Assemat, S. Vial, and E. Samain, “Laser ranging for effective and accurate tracking of space debris in low earth orbits,” in *Proceedings of the 6th European Conference on Space Debris*, L. Ouwehand, Ed., vol. 6, ESA, 2013.

[53] M. Driedger, A. Asgari, and P. Ferguson, “Feasibility of gathering resident space object range measurements using in-orbit observers,” *IEEE Journal of Radio Frequency Identification*, vol. 6, pp. 250–257, 2022. DOI: `10.1109/JRFID.2022.3160938`.

[54] J. J. Degnan, “Millimeter accuracy satellite laser ranging: A review,” in *Contributions of Space Geodesy to Geodynamics: Technology.* American Geophysical Union, 1993, pp. 133–162, ISBN: 0875905269. DOI: `10.1029/gd025p0133`. [Online]. Available: `http://dx.doi.org/10.1029/gd025p0133`.

[55] P. A. Forrester and K. F. Hulme, “Laser rangefinders,” *Optical and Quantum Electronics*, vol. 13, no. 4, pp. 259–293, Jul. 1981, ISSN: 1572-817X. DOI: `10.1007/BF00619793`. [Online]. Available: `https://doi.org/10.1007/BF00619793`.

[56] J. J. Degnan, “A tutorial on retroreflectors and arrays used in satellite and lunar laser ranging,” *Photonics*, vol. 10, no. 11, 2023, ISSN: 2304-6732. DOI: `10.3390/photonics10111215`. [Online]. Available: `https://www.mdpi.com/2304-6732/10/11/1215`.

[57] T. S. Kelso, *Norad two-line element set format*, Accessed: 2025-03-19, 2025. [Online]. Available: `https://celestrak.org/NORAD/documentation/tle-fmt.php`.

[58] T. S. Kelso, *Celestrak: Norad gp element sets current data*, `https://celestrak.org/NORAD/elements/`, TLE epoch for RCM2: , Accessed: 2024-11-14, 2024.

[59] W. Koch, “On exploiting ‘negative’ sensor evidence for target tracking and sensor data fusion,” *Information Fusion*, vol. 8, no. 1, pp. 28–39, 2007, Special Issue on the Seventh International Conference on Information Fusion-Part II, ISSN: 1566-2535. DOI: `https://doi.org/10.1016/j.inffus.2005.09.002`. [Online]. Available: `https://www.sciencedirect.com/science/article/pii/S1566253505000795`.

[60] J. Hoffman, M. Spranger, D. Gohring, and M. Jungel, “Making use of what you don’t see: Negative information in markov localization,” in *2005 IEEE/RSJ International Conference on Intelligent Robots and Systems*, 2005, pp. 2947–2952. DOI: `10.1109/IROS.2005.1545087`.

[61] D.-y. Lee, S.-w. Shim, M.-c. Hwang, and M.-j. Tahk, “Target tracking using adaptive coarse-to-fine particle filter,” in *AIAA Guidance, Navigation, and Control Conference*. American Institute of Aeronautics and Astronautics (AIAA), 2017. DOI: `10.2514/6.2017-1245`. eprint: `https://arc.aiaa.org/doi/pdf/10.2514/6.2017-1245`. [Online]. Available: `https://arc.aiaa.org/doi/abs/10.2514/6.2017-1245`.

[62] C. Greco and M. Vasile, “Robust bayesian particle filter for space object tracking under severe uncertainty,” *Journal of Guidance, Control, and Dynamics*, vol. 45, no. 3, pp. 481–498, 2022. DOI: `10.2514/1.G006157`. eprint: `https://doi.org/10.2514/1.G006157`. [Online]. Available: `https://doi.org/10.2514/1.G006157`.

[63] JENOPTIK Optical Systems, *Diode laser rangefinder (DLEM)*, 2023. [Online]. Available: `https://www.jenoptik.us/-/media/websitedocuments/optics/sensor/_datasheet_20230818.pdf`.

[64] Optotune, *Optotune MR-15-30: Dual axis fast steering mirror with position feedback mr-15-30*, 2024. [Online]. Available: `https://static1.squarespace.com/static/5d9dde8d550f0a5f20b60b6a/t/66d16614cb5fd940bc788955/1724999189711/Optotune+MR-15-30.pdf`.

[65] N. Metropolis and S. Ulam, "The monte carlo method," *Journal of the American Statistical Association*, vol. 44, no. 247, pp. 335–341, 1949. [Online]. Available: `https://www.jstor.org/stable/2280232`.

[66] T. Flohrer, H. Krag, H. Klinkrad, B. Virgili, and C. Frueh, "Improving esa's collision risk estimates by an assessment of the tle orbit errors of the us ssn catalogue," Jan. 2009.

[67] X.-l. Xu and Y.-q. Xiong, "Orbit error characteristic and distribution of TLE using CHAMP orbit data," *Astrophysics and Space Science*, vol. 363, no. 2, p. 31, Jan. 2018, ISSN: 1572-946X. DOI: `10.1007/s10509-018-3251-z`. [Online]. Available: `https://doi.org/10.1007/s10509-018-3251-z`.

[68] P. Kovář, P. Puričer, and K. Kovářová, "Study of the two-line element accuracy by 1u cubesat with a gps receiver," *Sensors*, vol. 22, no. 8, 2022, ISSN: 1424-8220. DOI: `10.3390/s22082902`. [Online]. Available: `https://www.mdpi.com/1424-8220/22/8/2902`.

[69] Á. González, "Measurement of Areas on a Sphere Using Fibonacci and Latitude–Longitude Lattices," *Mathematical Geosciences*, vol. 42, no. 1, pp. 49–64, Jan. 2010, ISSN: 1874-8953. DOI: `10.1007/s11004-009-9257-x`. [Online]. Available: `https://doi.org/10.1007/s11004-009-9257-x`.

[70] S. Clemens, R. Lee, P. Harrison, and W. Soh, "Feasibility of using commercial star trackers for on-orbit resident space object detection," in *Proceedings of the Advanced Maui Optical and Space Surveillance Technologies Conference (AMOS)*,

Presented at the 2018 AMOS Conference, AMOS, 2018. [Online]. Available: `https://amostech.com/TechnicalPapers/2018/Space-Based_Assets/Clemens.pdf`.

[71] R. Qashoa *et al.*, "SPACEDUST-Optical: Wide-FOV Space Situational Awareness from Orbit," in *Proceedings of the Advanced Maui Optical and Space Surveillance (AMOS) Technologies Conference*, S. Ryan, Ed., Sep. 2023, 160, p. 160.

[72] R. Clark, Y. Fu, S. Dave, and R. Lee, "Simulation of rso images for space situation awareness (ssa) using parallel processing," *Sensors*, vol. 21, no. 23, 2021, ISSN: 1424-8220. DOI: `10.3390/s21237868`. [Online]. Available: `https://www.mdpi.com/1424-8220/21/23/7868`.

[73] S. B. Howell, *Handbook of CCD Astronomy, Second Edition*. Cambridge University Press, 2006, vol. 2, p. 172, ISBN: 978-0-521-85215-9.

[74] V. Durán-Ramírez and D. Malacara-Doblado, "Keystone aberration correction in overhead projectors," *Applied Optics*, vol. 43, pp. 4123–4126, Jul. 2004. DOI: `10.1364/AO.43.004123`.

[75] Optotune, *MR-E-2 development kit operation manual*, `https://www.optotune.com/s/Optotune-MR-E-2-Development-Kit-operation-manual.pdf`, 2019.

[76] Bureau International des Poids et Mesures (BIPM), *The International System of Units (SI)*, 9th ed. Sèvres, France: BIPM, 2019, Definition of the metre based on the speed of light in vacuum. [Online]. Available: `https://www.bipm.org/en/publications/si-brochure`.

[77] M. Born and E. Wolf, *Principles of Optics: 60th Anniversary Edition*, 7th ed. Cambridge University Press, 2019, p. 93.

[78] European Space Agency (ESA), *Satellite Missions Catalogue: Starlette / Stella*, `https://directory.eoportal.org/satellite-missions/starlette#eop-quick-facts-section`, Accessed: 19 August 2025, 2012.

Appendices

Appendix A

Copyright Permission

A.1 Copyright from AMOSTech

Outlook

RE: Request to Use Material from Submitted Paper for Masters Thesis

From Sandy Ryan <sandy@medb.org>
Date Tue 5/7/2024 2:50 PM
To William Ediger [redacted] AMOS Conference Organizers <info@amostech.com>

Caution! This message was sent from outside the University of Manitoba.

Aloha William,

Thank you for contacting us requesting permission to use material from your paper presented at the 2023 AMOS Conference.

We are pleased to grant you permission for the stated purpose, and ask that if appropriate in this context, the following citation be referenced: 2023 Advanced Maui Optical and Space Surveillance Technologies Conference (AMOS), Maui, Hawaii – www.amostech.com.

Best wishes in your academic pursuits.

Respectfully,
Sandy Ryan

Ms. Sandy Ryan, Conference Director
AMOS Conference | amostech.com
EMER-GEN Program | emer-gen.com
A program of Maui Economic Development Board
1305 N. Holopono Street, Suite 1, Kihei, Hawaii 96753
808.283.1267.c | sandy@medb.org
Follow us for AMOS Updates at:

From: William Edige[redacted]
Sent: Tuesday, May 7, 2024 9:27 AM
To: AMOS Conference Organizers <info@amostech.com>
Subject: Request to Use Material from Submitted Paper for Masters Thesis

Some people who received this message don't often get email fro[redacted] Learn why this is important

Dear Conference Organizer,

[redacted]

I hope this email finds you well. I am writing to request permission to use material from a paper I previously submitted to your esteemed conference for my Masters Thesis. The technical paper was submitted in 2023 and is entitled "**SPACEDUST-Laser/RF: Time of Flight Methods for Space Situational Awareness**".

The content aligns closely with my current research, and its inclusion would greatly enhance the depth and quality of my thesis. I assure you that proper citations and acknowledgments will be provided.

Please let me know if this request aligns with your policies, and if any further steps are required from my end.

Thank you for your consideration.

Best regards,

William

William Ediger

STARLab – Department of Mechanical Engineering

Price Faculty of Engineering

University of Manitoba

[redacted]

[redacted]

A.2 Copyright from AIAA

Outlook

RE: Request for permission to use conference paper material

From Katrina Buckley <KatB@aiaa.org>
Date Mon 2025-02-24 7:45 AM
To William Ediger [redacted]
Cc ARC Support <arcsupport@aiaa.org>

Caution! This message was sent from outside the University of Manitoba.

Hello William,
Thank you for your inquiry. Since you and your co-author retained copyright of this paper (Copyright © 2025 by William Ediger and Philip Ferguson), you do not need AIAA's permission to reuse it. Generally, as the copyright holder you can reuse it as you wish; however, you may want or need to inform co-copyright holder(s) (please consult your institution as needed for guidance/requirements on that). AIAA also recommends that you acknowledge within the main text or a footnote that relevant sections/chapters of your thesis are reprinted (e.g., "From [paper title and authors]), and that the original source should be cited in full in the reference list.

Best,
Katrina Buckley
Managing Editor, Publications
703.264.7566 (direct)

AIAA
SHAPING THE FUTURE OF AEROSPACE

From: William Ediger [redacted]
Sent: Friday, February 21, 2025 2:59 PM
To: Customer Service <custserv@aiaa.org>
Subject: Request for permission to use conference paper material

Dear customer service,

I hope this email finds you well. I am writing to request permission to use material from a paper I previously submitted to your SciTech conference for my Masters Thesis. The paper was submitted in 2025 and is entitled "**Feasibility of Space-Based Laser Ranging for Resident Space Object Detection, (Control ID 4133144, Paper AIAA-2025-1163)**".

The content aligns closely with my current research, and its inclusion would greatly enhance the depth and quality of my thesis. I assure you that proper citations and acknowledgments will be provided.

Please let me know if this request aligns with your policies, and if any further steps are required from my end. If this email needs to be forwarded to the conference organizer of SciTech you have my permission.

Thank you for your consideration.

Best regards,

William

William Ediger

STARLab – Department of Mechanical Engineering

Price Faculty of Engineering

University of Manitoba

[redacted]

[redacted]

A.3 Copyright from IEEE

In reference to IEEE copyrighted material which is used with permission in this thesis, the IEEE does not endorse any of University of Manitoba's products or services.

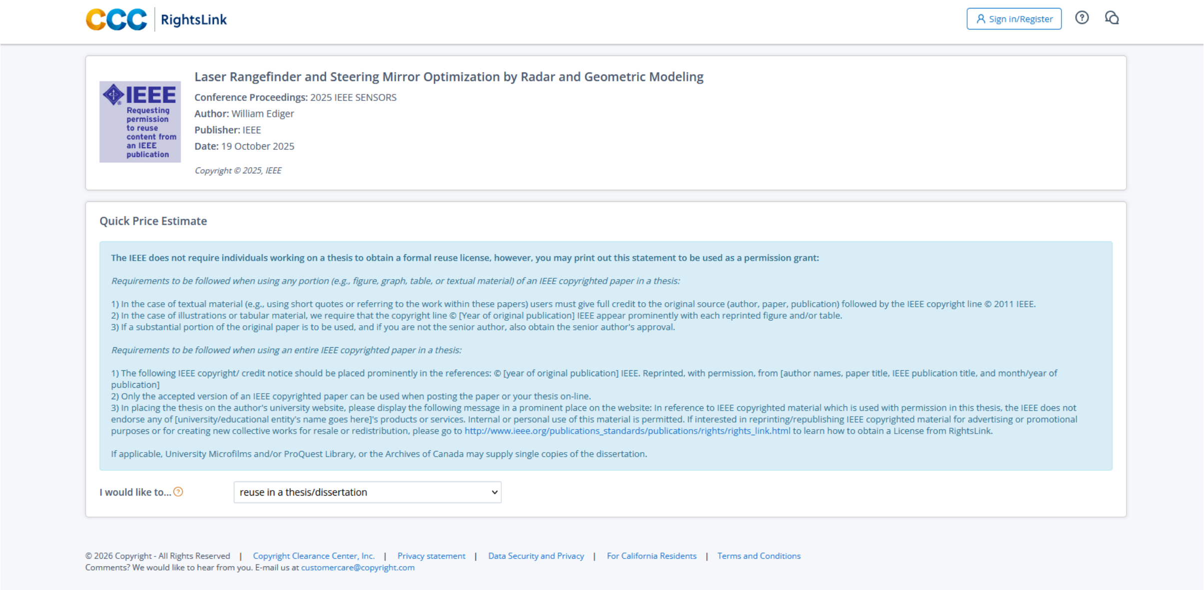

Laser Rangefinder and Steering Mirror Optimization by Radar and Geometric Modeling

Conference Proceedings: 2025 IEEE SENSORS
Author: William Ediger
Publisher: IEEE
Date: 19 October 2025

Copyright © 2025, IEEE

Quick Price Estimate

The IEEE does not require individuals working on a thesis to obtain a formal reuse license, however, you may print out this statement to be used as a permission grant:

Requirements to be followed when using any portion (e.g., figure, graph, table, or textual material) of an IEEE copyrighted paper in a thesis:

1) In the case of textual material (e.g., using short quotes or referring to the work within these papers) users must give full credit to the original source (author, paper, publication) followed by the IEEE copyright line © 2011 IEEE.
2) In the case of illustrations or tabular material, we require that the copyright line © [Year of original publication] IEEE appear prominently with each reprinted figure and/or table.
3) If a substantial portion of the original paper is to be used, and if you are not the senior author, also obtain the senior author's approval.

Requirements to be followed when using an entire IEEE copyrighted paper in a thesis:

1) The following IEEE copyright/ credit notice should be placed prominently in the references: © [year of original publication] IEEE. Reprinted, with permission, from [author names, paper title, IEEE publication title, and month/year of publication]
2) Only the accepted version of an IEEE copyrighted paper can be used when posting the paper or your thesis on-line.
3) In placing the thesis on the author's university website, please display the following message in a prominent place on the website: In reference to IEEE copyrighted material which is used with permission in this thesis, the IEEE does not endorse any of [university/educational entity's name goes here]'s products or services. Internal or personal use of this material is permitted. If interested in reprinting/republishing IEEE copyrighted material for advertising or promotional purposes or for creating new collective works for resale or redistribution, please go to http://www.ieee.org/publications_standards/publications/rights/rights_link.html to learn how to obtain a License from RightsLink.

If applicable, University Microfilms and/or ProQuest Library, or the Archives of Canada may supply single copies of the dissertation.

I would like to... reuse in a thesis/dissertation

© 2026 Copyright - All Rights Reserved | Copyright Clearance Center, Inc. | Privacy statement | Data Security and Privacy | For California Residents | Terms and Conditions
Comments? We would like to hear from you. E-mail us at customercare@copyright.com

Appendix B

Search Simulation and Experiment Statistical Comparison

B.1 Stationary Target Acquisition Performance Comparison

Beginning with the spiral pattern, my null hypothesis, H_0 is that the true hit rate is 65.8% and my alternative hypothesis, H_1 is that the true hit rate is not 65.8%, given in Equations B.1 and B.2. I used a significance level of 5% ($\alpha = 0.05$).

$$H_0 : \quad p = 0.635 \tag{B.1}$$

$$H_1 : \quad p \neq 0.635 \tag{B.2}$$

Each test run is independent and is either a success (target hit) or a failure (target not hit), therefore I treat the hit rate as a binomial random variable, X. The probability mass function for a Binomial variable is given in Equation B.3, where n is the number of trials, k is the number of desired successes, and p is the probability of getting a success in one trial.

$$P(X = k) = \frac{n!}{(n-k)!k!} p^k (1-p)^{n-k} \tag{B.3}$$

Because I am testing whether the experimental results are consistent with the simulation, whether or not the experimental results are higher or lower, I use a two sided hypothesis test. This means to calculate the p-value I should consider the probability that I get the result I actually got, in addition to all probabilities that are the same or less likely. The probability that I see 8 successes in 10 trials, with a true hit probability of 63.5% is:

$$P(X = 8) = \frac{10!}{(10-8)!8!}(0.635)^8(1-0.635)^{10-8} \tag{B.4}$$

$$P(X = 8) = 0.1585 \tag{B.5}$$

Likewise, the rest of the probabilities can be calculated in this manner, tabulated in Table 17.

Table 17. Spiral search experimental hit rate probabilities assuming a true success rate of 63.5%

$P(X = k)$	Value (%)
$P(X = 0)$	0.00
$P(X = 1)$	0.07
$P(X = 2)$	0.57
$P(X = 3)$	2.65
$P(X = 4)$	8.07
$P(X = 5)$	16.86
$P(X = 6)$	24.44
$P(X = 7)$	24.29
$P(X = 8)$	15.85
$P(X = 9)$	6.13
$P(X = 10)$	1.07

Summing all of the cases with probabilities that are equal to or smaller than 15.85% yields 34.41%, which is larger than the level of significance of 5%. Therefore, the experimental performance for the Archimedes spiral is consistent with the simulated performance.

I performed the same hypothesis testing process for the Bayesian search results. In this case the null and alternative hypotheses are:

$$H_0 : \quad p = 0.779 \tag{B.6}$$

$$H_1 : \quad p \neq 0.779 \tag{B.7}$$

The likelihood with a true probability of 77.9% that one would see 10 successes in 10 trials is:

$$P(X = 10) = \frac{10!}{(10-10)!10!}(0.779)^1 0(1-0.779)^{10-10} \tag{B.8}$$

$$P(X = 10) = 0.0823 \tag{B.9}$$

Likewise, the rest of the probabilities can be calculated in this manner, tabulated in Table 18.

Table 18. Bayesian search experimental hit rate probabilities assuming a true success rate of 78.7%

$P(X = k)$	Value (%)
$P(X = 0)$	0.00
$P(X = 1)$	0.00
$P(X = 2)$	0.02
$P(X = 3)$	0.15
$P(X = 4)$	0.90
$P(X = 5)$	3.81
$P(X = 6)$	11.19
$P(X = 7)$	22.55
$P(X = 8)$	29.81
$P(X = 9)$	23.35
$P(X = 10)$	8.23

Summing all of the cases with probabilities that are equal to or smaller than 8.23% yields 13.11%, which is larger than the level of significance of 5%. Therefore, the experimental performance for the Bayesian search was consistent with the simulated performance.

B.2 Moving Rover Acquisition Performance Comparison

In Table 19, I tabulate the likelihood of seeing any given number of near misses assuming the simulation near miss rate using the same process as for the stationary testing. The likelihood of seeing a result as likely or rarer than two near misses assuming the simulation near miss rate is 64.47%. Therefore the experimental near miss rate is consistent with the simulation. The near miss time is also very similar between simulation and experiment, with an error of 10.47%.

Table 19. Bayesian search for moving rover experimental near miss rate probabilities assuming a true success rate of 14.4%

$P(X = k)$	Value (%)
$P(X = 0)$	21.12
$P(X = 1)$	35.53
$P(X = 2)$	26.89
$P(X = 3)$	12.07
$P(X = 4)$	3.55
$P(X = 5)$	0.72
$P(X = 6)$	0.10
$P(X = 7)$	0.01
$P(X = 8)$	0.00
$P(X = 9)$	0.00
$P(X = 10)$	0.00